Microstructural design of CaMnO3 and its thermoelectric proprieties.

Natalia Maria Mazur

Declaration

I hereby declare that the work presented in this document has been performed independently and in accordance with the rules and regulations of the Norwegian University of Science and Technology (NTNU).

Trondheim, 12 June 2015

Natalia Mazur

Preface

The work described in this thesis has been performed at the Department of Materials Science and Engineering at the Norwegian University of Science and Technology (NTNU) during spring 2015.

During that period numerous people have been involved in this project and provided me with their assistance. In fist place I'd like to thank my supervisor, Professor Kjell Wiik for his time and guidance throughout the project work. Your knowledge and advice have been most helpful in understanding the material system and overcoming the challenges.

Further I would like to acknowledge and thank Anne Støre (SINTEF) for conducting thermal conductivity measurements on Laser Flash apparatus and PhD Sathya Prakash Singh for help with understanding and conducting Seebeck coefficient measurements and 4-point probe electrical conductivity measurements.

I would also like to thank all the technical staff at the Department of Materials Science and Engineering at NTNU for all the support with experimental part. Lastly I would like to thank all the members of Inorganic Materials and Ceramics Research Group at the Department of Materials Science and Engineering and the members of THELMA project for all the helpful advices I received during the semester.

Thank you all for your help.

Abstract

Calcium manganate (CMO) is an n-type semiconductor with promising thermoelectric proprieties. Solid state synthesis was employed to synthesise the desired material in two phases: i) reduced rock-salt phase of CaO-MnO (ss) and ii) oxidized phase of $CaMnO_3$ with secondary phase of $CaMn_2O_4$ (marokite). In addition to stoichiometric CMO, three two-phase materials consisting of 2.5vol%, 5vol% and 10vol% of marokite were synthesised. The secondary phase was introduced to investigate its proprieties as a phonon scattering agent with the aim on lowering on the thermal conductivity and enhancement of the thermoelectric figure of merit, zT. Structural and thermoelectric proprieties of the materials were investigated in order to determine correlation between material's microstructure, composition and TE proprieties.

Investigated CMO system produced dense samples with over 90% of the theoretical density. Resulting material consists of large grains with secondary phase precipitating on grain boundaries and triple points. Increased amount of secondary phase reduced material's strength and lead to formation of microcracks on the surface. Transformation of the rock-salt into perovskite is a very rapid reaction and it follows the topotactic reaction mechanism. Formation of marokite is a two step reaction with formation of $Ca_2Mn_3O_8$ at about $570°C$ and its transformation to marokite at about $850°C$.

Introduction of marokite as secondary phase resulted in enhancement of electrical and thermal conductivity and lowering of the absolute value of Seebeck coefficient. Thermal conductivity was enhanced due to large grains that are beneficial for thermal transport and good thermal conductivity proprieties of the secondary phase. Electrical conductivity was enhanced due to change in $\frac{[Mn^{3+}]}{[Mn^{4+}]}$ ratio that is governs charge carrier density. Phase transitions between the two secondary phases lead to formation of oxygen vacancies in CMO that increase its electrical proprieties through generation of Mn^{3+}-ions that supply free charge carriers at lower temperatures. Seebeck coefficient values increase with increasing volume of secondary phase as the density of charge carrier increases.

High thermal conductivity and lower than expected electrical conductivity resulted in relatively low power factor (PF) and zT. From the investigated samples CMO with 2.5vol% marokite is the most promising one as it exhibits highest PF and zT = 0.0062 at $900°C$.

Sammendrag

Kalsium manganat (CMO) er en n-halvleder med lovende termoelektriske egenskaper. Materialet ble syntetisert i to steg: i) den reduserte CaO-MnO(ss) fasen med NaCl-struktur og ii) den oksiderte perovskitt fasen med $CaMn_2O_4$ som en sekundær fase. I tillegg til stoikiometrisk CMO, tre to-fase materialer med 2.5vol%, 5vol% og 10vol% ble syntetisert. Den sekundære fasen ble introdusert for å redusere termisk ledningsevne og forbedre zT (thermoelectric figure of merit). Strukturelle og termoelektriske egenskaper ble undersøkt for å bestemme korrelasjon mellom mikrostruktur, sammensetning og de termoelektriske egenskaper til CMO.

Untersøkt CMO system produserte prøver med over 90% av den teoretiske tettheten. Dannet materiale består av store korn med utfelling av den sekundære fasen på korngrenser og trippelpunkt. Økende mengde av den sekundære fase reduserte materialets styrke og førte til dannelse av micro-sprekk på overflaten. Transformasjonen fra NaCl-struktur til perovskitt skjer veldig raskt og den følger en topotaktisk reaksjonsmekanisme. Dannesle av $CaMn_2O_3$ skjer i to steg: i) dannelse av $Ca_2Mn_3O_8$ ved ca. $570°C$ og ii) omdannelse av $Ca_2Mn_3O_8$ til $CaMn_2O_4$ ved ca. $850°C$.

Introduksjon av $CaMn_2O_4$ til CMO-system førte til økning i elektrisk og termisk ledningsevne og senking av den absolutte verdien til Seebeck-koeffisienten. Termisk ledningsevne økte på grunn av store korn og gode termiske egenskaper til den sekundære fasen. Elektrisk ledningsevne økte på grunn av endring i $\frac{[Mn^{3+}]}{[Mn^{4+}]}$ som påvirker ladningsbærer konsentrasjon. Fase overgang mellom de to sekundære faser danner oksygen-vakanser i CMO som forbedrer elektriske egenskaper ved lave ved å danne Mn_{3+}-ioner som tilfører ladningsbærere til systemet. Seebeck-koeffisienten øker med økende sekundære fase volum på grunn av økende ladningsbærer tetthet.

Høy termisk edningsevne og lavere enn forventet elektrisk ledningsevne førte til relativt lav $S^2\sigma$ og zT. Utifra undersøkte sammensetninger, CMO med 2.5vol% av $CaMn_2O_4$ gir beste resultater med zT = 0.0062 ved $900°C$.

Contents

Chapter 1

Introduction

1.1 Background

Energy consumption in today's world is constantly increasing. Hundreds of factories around the world are constantly working to meet the demand. Many of them are burning fossil fuels, which unfortunately have negative side-effects on the environment in addition to their limited abundance. On top of that, it not only costs energy to produce energy, but also not everything that is produced is being utilized as it is being lost during the processes.

Heat is an abundant but low quality energy source. Currently more than half of all the energy generated is lost [21] wile only in Norway it is possible to save up to 40% of the produced energy and a third of those losses are in form of waste heat.[64] There are many ways to minimize those losses and this work is focusing on a currently understated method and aims to shine some light on developing technologies that could enhance efficiency of many industrial processes.

Thermoelectric (TE) materials and devices provide us with the ability to directly convert heat into electricity. A classical TE device consists of many thermoelectric couples as shown in Fig. 1.1, where each couple is made up of a n- and a p-type TE material, an insulator and a connector joining both legs. The n- and p-type semiconductors generate the thermoelectromotive force of the opposite signs that doubles the voltage when combined. [43] Those couples are then wired electrically in series and thermally in parallel.

TE devices, being solid state devises, have several advantages over more traditional devices such as heat pumps or heat engines. Compared to those, they have no moving parts, resulting
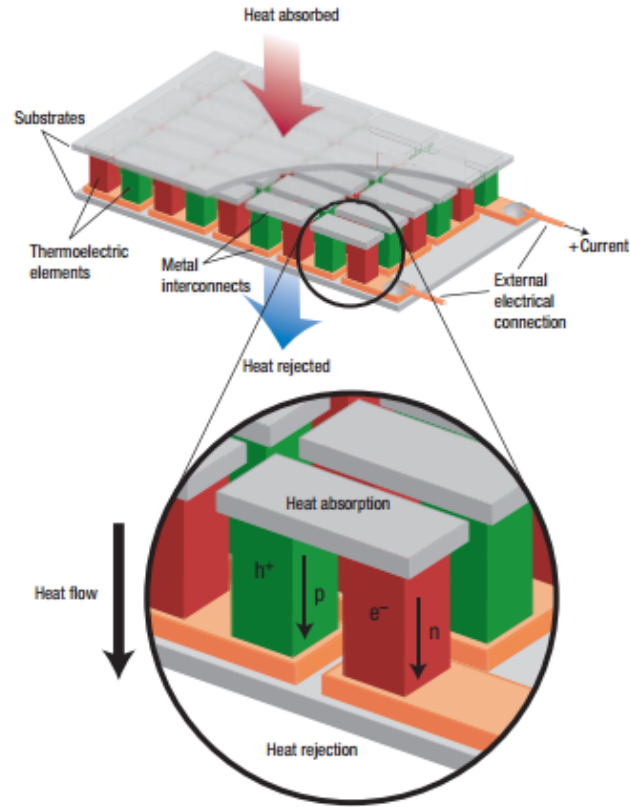
Figure 1.1: Schematic illustration of a TE device [60]

in less maintenance, higher reliability and longer life span. As shown in Fig. 1.2 TE devices can be easily scaled down without loosing their efficiency making the applicable for other environments than industry. Disadvantages of TE devices is their low efficiency compared with classical devices. Lack of design knowledge and design tools is also slowing down their introduction into commercial marked at the same time being a great motivation for further research.

Another aspect lowering the TE device efficiency are the TE materials used to produce those devices. Currently, there are many well developed state-of-the-art TE materials that are being in use. In spite of their relatively high efficiency those materials are often toxic, unstable in air and expensive thus having a limited of usability. This is the reason for why up till now TE devices were mainly used in deep-space exploration missions, in military applications and in remote locations were connection to the power grid was impossible. That is why the main focus of current research within TE is to synthesize a cheap, eco-friendly material with high thermal and chemical stability in air and also a relatively high energy conversion, often described in toe from of a dimensionless figure of merit, zT.
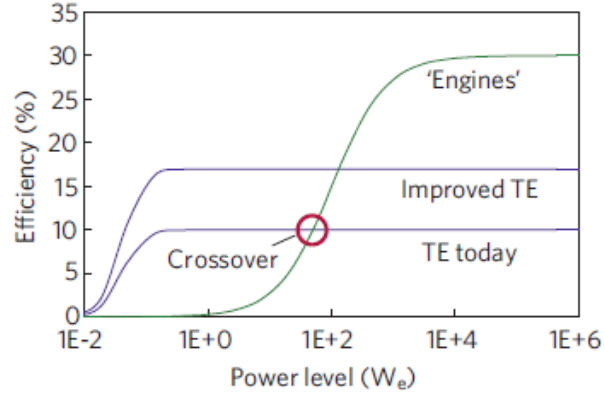
Figure 1.2: An illustrative plot of efficiency versus size for TE and classical devices. [72]

The thermoelectric figure of merit, zT is a key figure in TE material research. It correlates the three most important proprieties of a TE material, electrical conductivity, σ, Seebeck coefficient, S, and thermal conductivity, κ as shown in Eq.1.1: [43]

$$zT = \frac{\sigma S^2 T}{\kappa} \tag{1.1}$$

The goal is to have as high zT as possible since this ensures good electrical proprieties of the device and high conversion of heat to electricity. Enhancement of this figure of merit is not that simple through. All three aforementioned proprieties are interrelated through charge carrier concentration making it difficult to control and adjust each parameter separately.

Since the *phonon-glass electron crystal concept* (PGEC) was introduced in 1979 [55] an intensive research within TE materials has been done. The idea is to be able to independently control the electronic and the lattice properties of a material. PGEC materials would possess electronic properties of good crystalline semiconductors combined with "glass-like" thermal conductivities. The goal is to establishing a material with low thermal conductivity and optimize its electronic proprieties by suitable substitutions. Similar way of thinking was used in this work with the focus on lowering of the thermal conductivity,

1.2 Objective

The focus of this master project is synthesis of a thermoelectric oxide, characterization and improvement of its proprieties. Calcium manganate (CMO), $CaMnO_{(3-\delta)}$, was chosen as the material of interest. It belongs to the more general $ABO_{(3-\delta)}$ group with a perovskite structure. Those nonstioichiometric compounds are forming a complex and phenomenologically rich group worth investigating.[13] CMO was selected for following reasons: i) it is stable in oxidizing atmosphere at high temperatures ii) it is non-toxic and eco-friendly iii) raw materials are cheap as they are highly abundant, iv) solid solubility between CaO and MnO makes structuring possible, v) the Ca-Mn-O phase diagram shows many secondary phases that can be utilized as phonon scattering mechanism vi) extensively studied material exhibiting promising results. Those proprieties makes this material a valid match of other TE materials presented in Fig. 1.3.
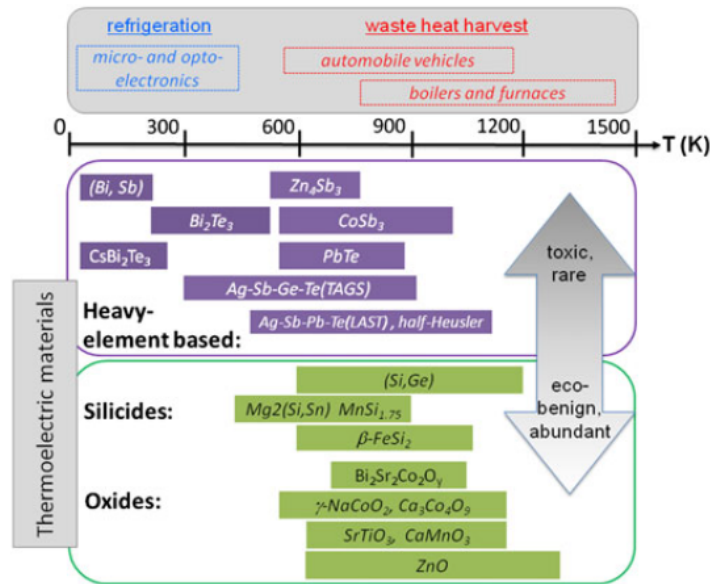
Figure 1.3: Schematic comparison of various TE materials in terms of the applicable temperature range, abundance and environmental friendliness. [21]

The goal is to improve TE proprieties by employing structuring to lower thermal conductivity of the material. This is to be achieved by introducing secondary phases and grain boundary scattering while maintaining high electrical conductivity and Seebeck coefficient. Solid state reactions will be used in the synthesis process while techniques such as XRD, SEM, Archimedes density measurement, Laser Thermal flash, 4-point probe measurement and Seebeck measure-

ment will be used to characterize materials proprieties. Synthesis route partially determined during specialization project in Fall 2014 is the starting point for the work. Correlation between microstructure, phase composition and thermoelectric proprieties is to be studied and determined.

Chapter 2

Theory

2.1 Thermoelectric effects

The total thermoelectric effect is comprised of three reversible effects, Seebeck, Peltier and Thomson. The common base for those three effects is the ability of charge carriers to carry both heat and electricity at the same time. In addition to those effects two irreversible effects, Joule heating and Thermal conduction, occur simultaneously affecting the heat and current transport. **Joule heating**, also called resistive heating, is caused by the passing current and leading to heat release in the material. **Thermal conduction** is caused by a temperature gradient in a material which induces a flow of heat in the direction of negative gradient. [49] Although neglected in the case of this work, as it focuses only on improvement of material's TE proprieties, those effects have to be taken into consideration in TE device development.

2.1.1 Seebeck effect

In 1821 John Seebeck discovered a phenomenon that became the basis of thermoelectricity. He observed that when two dissimilar, homogeneous, conductive materials are put in a direct contact with each other creating a closed loop, an electric current will flow given the two junctions are kept at different temperatures [49] as illustrated in Fig. 2.1.

The temperature difference causes a more frequent generation of electron-hole pairs at higher temperatures, raising a potential gradient in the loop. As material tries to equilibrate the charge
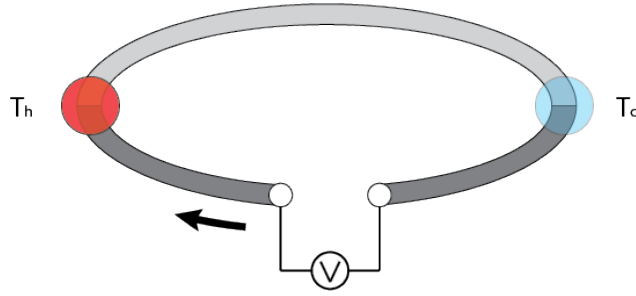
Figure 2.1: Schematic illustration of Seebeck effect between two dissimilar materials with junctions held at different temperatures where $T_h > T_c$. Arrow indicates the direction of current flow.

carrier surplus on the hot side, a carrier diffusion through the material towards the cold side takes place leading to an electrical diffusion current. As a result, in a n-type material, where the charge carriers are electrons, negative charges will build up at the cold side while in a p-type materials, holes will be accumulated.[11] This effect is called the Seebeck effect and it is the direct conversion of temperature difference into electricity.

The induced voltage V due to carrier diffusion depends on the temperature difference between the hot and cold and can be expressed as [11]

$$V = \int_{T_c}^{T^h} S(T)T \tag{2.1}$$

where T_c and T_h are respectively temperature at the cold and hot end and S is the Seebeck coefficient which then can be expressed as:[54]

$$S = \frac{V}{\Delta T} \tag{2.2}$$

where ΔT is the temperature difference between T_h and T_c. This implies that the produced voltage is proportional to the temperature difference, and that theoretically, the larger the temperature difference the more current flows through the loop. By convention, S, also called the themropower, is negative for n-type and positive for p-type materials.

Since Seebeck effect occurs only when two materials are in direct contact, Seebeck coefficient cannot be measured for a single material. However, it was found experimentally that Seebeck coefficient can be represented as the difference between two quantities, where one of them is chosen as a reference material (Pt, Pb or Cu). From those measurements it is possible to

calculate S for any single material of a couple $XY = XR - YR$ where XY is a designated couple made up of materials X and Y and R is the reference material. [49]

2.1.2 Peltier effect

When the process of power generation is reversed by applying current to a couple of dissimilar materials, a temperature increase or decrease at the junction is observed. This effect was discovered by J.C Peltier in 1834 and it is illustrated in Fig. 2.2.
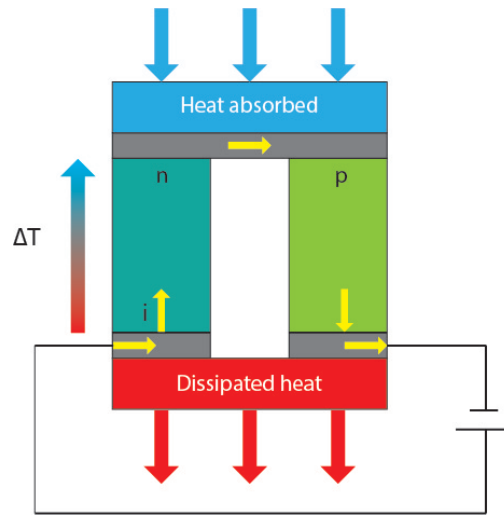
Figure 2.2: Schematic illustration of Peltier effect in a thermocouple. Yellow arrow indicate direction of current flow, *i*. Red and blue arrows indicate direction of heat flow, while the grey boxes are the metallic contacts between semiconductors.

Heat release or absorption, Q, is dependant on the direction and proportional to the electric current, I, flowing through the junction, as expressed in Eq. 2.3, where Π is the Peltier coefficient. This coefficient is defined as $\frac{I}{Q}$ i.e the heat transferred reversibly with the electric current at constant temperature and it tells how much heat is carried per unit charge through the material.

$$Q_P = (\Pi_A - \Pi_B) \cdot I = \Pi_{AB} \cdot I = S_{AB} \cdot T \cdot I \qquad (2.3)$$

where S is the Seebeck coefficient while A and B denote the two different materials. Same as for Seebeck coefficient, Peltier coefficient cannot be measured for a single material but only for couples or against a reference material.

2.1.3 Thomson effect

The last thermoelectric phenomenon, the Thomson effect, describes changes in energy of a charge carriers exposed to a temperature gradient. Heat transfer is determined by the direction of the charge carrier flow meaning if a charge carrier is moving with the temperature flux it will loose energy and when it moves against the flux it will gain energy. This means that an electron will gain energy with increasing temperature and loose it when temperature decreases. The heat absorbed or liberated can be expressed as: [32]

$$Q_T = \beta \cdot I \cdot \frac{dT}{dx} \tag{2.4}$$

where β is the Thomson coefficient, I is the electric current and $\frac{dT}{dx}$ is the temperature gradient.

2.1.4 Interdependency of thermoelectric effects

Aforementioned effects, Seebeck, Peltier and Thomson, are closely connected. This connection was proved and described by W. Thomson in 1851 in what later became known as Kelvin relationships: [11]

$$\beta = T\frac{dS}{dT} \tag{2.5}$$

$$\Pi = S \cdot T \tag{2.6}$$

By measuring the Thomson coefficient of an individual material over a selected temperature range, the absolute values for the Peltier and Seebeck coefficients can be calculated via Thomson relations. This is possible because only Thomson coefficient can be measured directly for a single material, while Peltier and Seebeck coefficients can only be measured against reference materials.

2.2 Thermoelectric figure of merit and the thermoelectric parameters

In 1949 the concept of a thermoelectric figure of merit, zT, was developed by Abram Fedorovich Ioffe.[67]. The figure of merit (FOM) presented in Eq.2.7 describes the relationship between the three quantities determining the TE proprieties of a material: [43]

$$zT = \frac{\sigma S^2 T}{\kappa_{tot}} = \frac{S^2 T}{R\kappa_{tot}} \tag{2.7}$$

where S is the Seebeck coefficient, σ is the electrical conductivity, κ_{tot} is the total thermal conductivity, R is the electrical resistivity and T is the absolute temperature. In principle z is the thermoelectric figure of merit a material, however since it is temperature dependant it is more meaningful to use it in its dimensionless form zT.

The thermoelectric figure of merit of a material is determined by measuring the Seebeck coefficient under small temperature gradient of 5 to 10K, the electrical conductivity under isothermal conditions, and the thermal conductivity under $\approx$ 1K temperature gradient. This means that the Eq. 2.7 is valid only for small temperature gradients, i.e. ΔT < 10 K. [11] For larger temperature gradients, the zT value decreases with increasing ΔT mainly due to the Thomson effect which has to be then taken into consideration when designing TE devices.[17]

The ultimate goal is to have as high zT as possible which implies that a good TE should possess (i) large Seebeck coefficient, in order to efficiently convert heat into electricity, (ii) high electrical conductivity to minimize ohmic losses and Joule heating due to electrical resistance and (iii) low thermal conductivity to minimize heat losses and maintain the thermal gradient. [35] The three thermoelectric parameters are functions of the carrier concentration and they are interrelated in a conflicting manner. Those relationships will be studied further in Section 2.2.4

2.2.1 Seebeck coefficient

In an earlier section Seebeck coefficient was defined as relation between the induced voltage and the temperature difference, Eq. 2.2. By utilizing thermodynamics of irreversible processes, Seebeck coefficient can be expressed as: [22]

$$S = \frac{8\pi^2 k_B^2}{3eh^2} m^* T (\frac{\pi}{3n})^{\frac{3}{2}} \tag{2.8}$$

where k_B is the Boltzman constant, e is electron charge, h is Planck's constant, m^* is the effective carrier mass, T is the absolute temperature and n is charge carrier concentration. Assuming that S is measured at constant temperature, the only variable in this equation will be carrier concentration n that can be varied through doping. By looking at the equation we can see that S will decrease when n increases. Reason for this is the fact that Seebeck effect is caused by the induced voltage in the material. The higher the carrier concentration to begin with the lower the induced voltage as it takes less new electron-hole pairs to induce current flow through the material.

2.2.2   Electrical conductivity

Electrical conductivity is obviously strongly affected by the carrier concentration. It is derived from the Ohm law and expressed as: [22]

$$\sigma = \frac{1}{R} = ne\mu \tag{2.9}$$

where μ in this case is the carrier mobility, n is the carrier concentration and e is the electron charge.

This equation illustrates very well that σ increases with increasing carrier concentration simultaneously decreasing the electrical resistivity of the material. In addition, electrical conductivity can be expressed through the Arrhenius equation: [27]

$$\sigma = \frac{A}{T} exp(\frac{-E_a}{k_B T}) \tag{2.10}$$

where A is the pre-exponential factor, k_B is Boltzmann's constant, T the absolute temperature and E_a the activation energy of conduction. E_a of 0.16eV is being reported for $CaMnO_3$ prepared by solid state reaction.[66]

2.2.3 Thermal conductivity

In a crystalline solid, heat can be carried through the motion of charge carriers described as the electronic thermal conductivity, κ_{el}, and through the lattice vibrations, i.e. phonon thermal conductivity, κ_{ph}. As a result, the total thermal conductivity, κ_{tot} is defined as a sum of the electronic and lattice component, Fig. 2.3:

$$\kappa_{tot} = \kappa_{el} + \kappa_{ph} \tag{2.11}$$
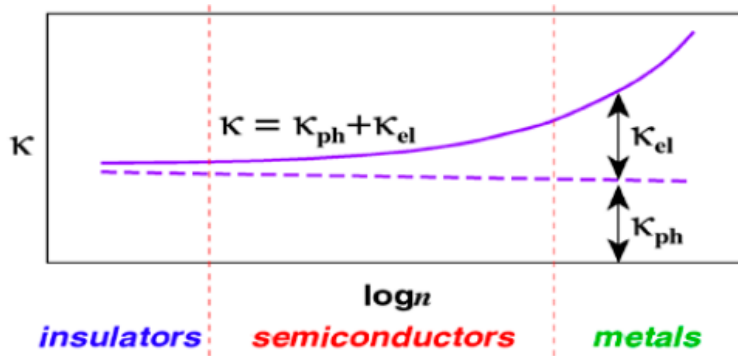
Figure 2.3: Thermal conductivity dependence on carrier concentration [42]

The electronic thermal conductivity can be expressed as [10]

$$\kappa_{el} = L\sigma T \tag{2.12}$$

where L is the Lorentz number, σ is the electrical conductivity and T is the temperature. Another illustrative equation is the Wiedemann-Franz relationship [16]:

$$\frac{\kappa_{el}}{\sigma} = \left(\frac{\pi^2 k_B^2}{3e^2}\right)T \tag{2.13}$$

where e is charge of an electron and k_B is the Boltzman's constant.

Both equations indicate that the ratio between σ and κ_{el} is constant at a given temperature and that any improvement in electrical conductivity leads to an offsetting increase in the electronic thermal conductivity.

The lattice thermal conductivity dominates the heat conduction process in insulators and its contribution becomes less significant the more metallic material is. Although lattice vibra-

tions are independent of the carrier concentration the lattice thermal conductivity increases rapidly and becomes less significant in materials with high carrier concentration because the electronic thermal conductivity is the dominating process. Lattice thermal conductivity corresponds to the propagations of phonons in the three space dimensions through the crystal lattice and can be expressed as: [61]

$$\kappa_{ph} = \frac{1}{3}C_V v l_{ph} \tag{2.14}$$

where C_V is the heat capacity at constant volume, v is the concentration and velocity of phonons and l_{ph} is the phonon mean free path, which is defined as the average distance a phonon travels before colliding with another particle. The evolution of κ_{ph} with the temperature depends on the dominating interactions occurring in the lattice. At low temperatures those limitations are caused by the grain size and the defect concentration while at high temperatures, collisions between phonons are the dominant factor limiting heat conduction.

2.2.4 Interdependency of thermoelectric proprieties

The generalized carrier concentration dependence of S, σ, and κ for conventional TE materials is presented in Fig. 2.4. Based on this figure we can see that insulating materials present large Seebeck coefficients, low thermal conductivities and high electrical resistivity values due to low charge carrier concentrations while metals, which are good electrical conductors, display low thermopower and high thermal conductivity due to large carrier density. Semiconductors, being in between those two worlds are in great position having TE proprieties that can be tailored according to the demand.

Closed inspection of that figure shows that there always will be a trade-off when designing new TE materials. This is because all three proprieties are to some degree affected by changes in charge carrier concentration. When the Seebeck coefficient is improved the electrical conductivity will be decreased. Then again when the electrical conductivity is enhanced so is the electronic part of the thermal conductivity resulting in overall enhancement of thermal conductivity.

The PGEC concept, that was mentioned in introduction, suggested obtaining lowest possible
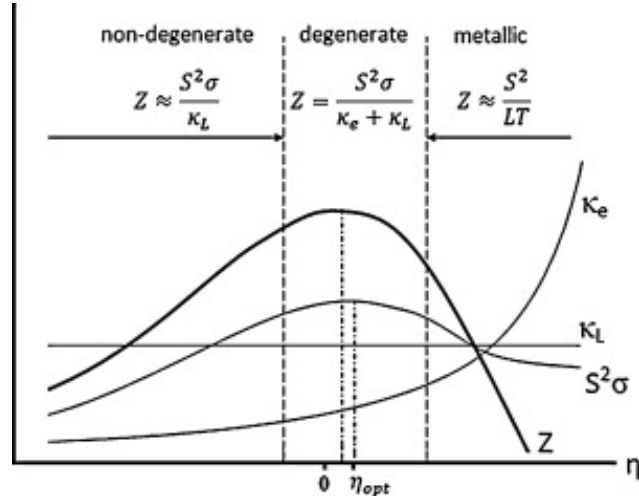
Figure 2.4: Relation between TE proprieties included in zT [47] plottet with respect to temperature and η is carrier concentration. In this case κ_e and κ_L are respectively electronic and lattice thermal conductivity.

thermal conductivity first, before fine-tuning electrical proprieties. It should be noted though, that the defects induced to lower the thermal conductivity, scatter not only phonons but also charge carriers, leading to lower electrical conductivity. Luckily in case of semiconductors, thermal conductivity is mainly dependant on the lattice contribution and it can be lowered without affecting the other two TE proprieties at great extent.

Ioffe has shown that zT has its maximum in the region where the carrier density is of the order of 10^{18} to 10^{21} carriers per cm^3[25]. This corresponds to highly doped semiconductors and semi-metals and those n values maximize power factor (PF), σS^2 [21]. High PF is desired as it provides a much needed balance between Seebeck coefficient and electrical conductivity.

2.3 Enhancement of zT

As illustrated in Fig. 2.5, many various methods are employed to enhance the thermoelectric figure of merit. The main approaches are focusing on either enhancement of the electrical conductivity, on lowering of the thermal conductivity or they are trying to combine both.

The most popular way to enhance the electrical conductivity is by doping. This method supplies additional charge carriers to the material which in extent increases the electrical conductivity. Downside of this method is possibility of enhancement of the electronic part of the
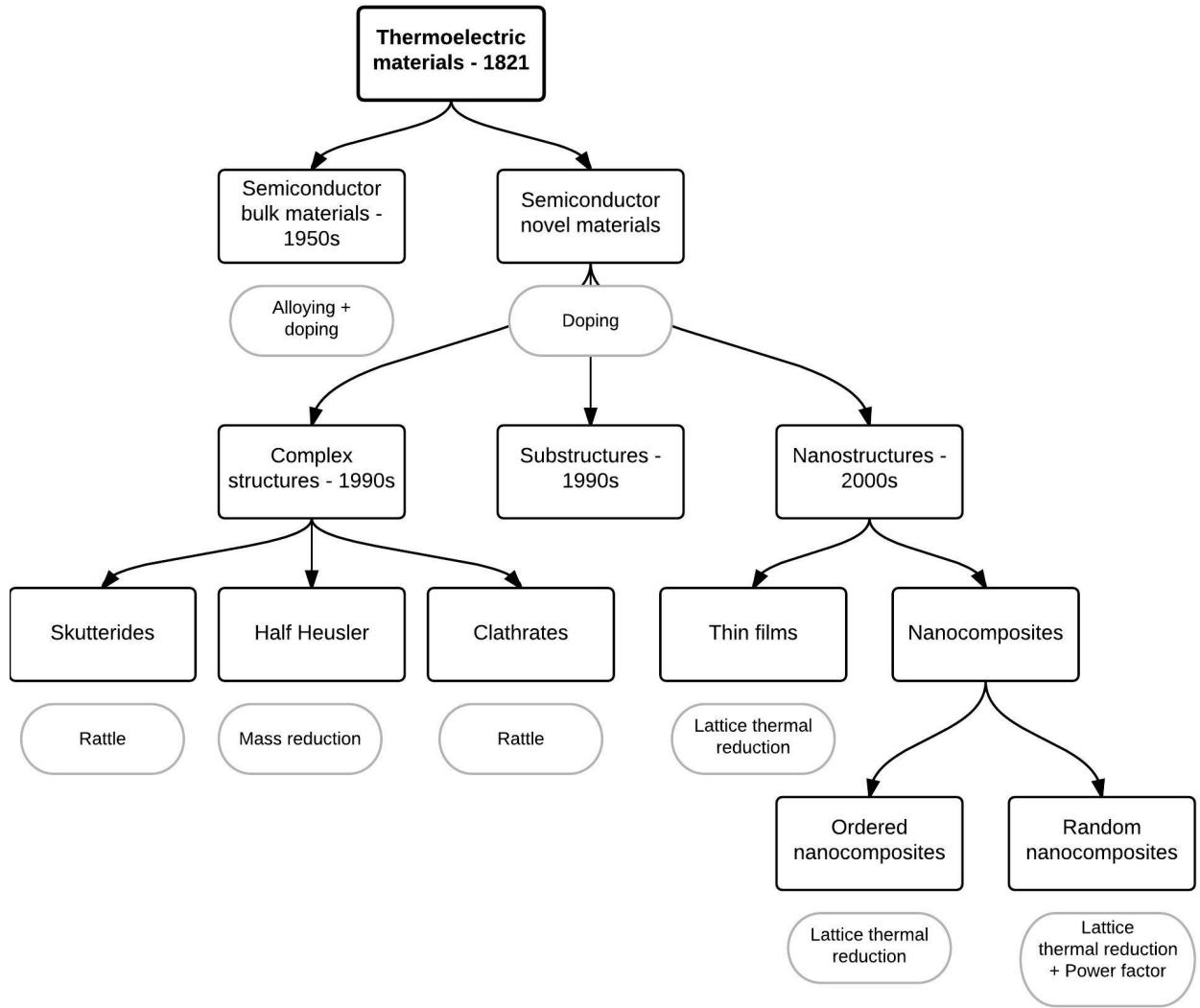
Figure 2.5: History of efforts in increasing zT. Black rectangles are types of materials and grey ovals specify utilized approach. Remastered from Alam et.al. [22]

thermal conductivity as well as lowering of the Seebeck coefficient. Further rare earth metals or heavy metals are often used as dopants, which are often not only expensive materials but also toxic making it more difficult to utilize them in everyday applications.

The other popular approach is lowering of the thermal conductivity. Importance of that approach can be easily visualized rearranging Eq.2.7 by utilizing the Wiedemann-Franz relationship (Eq. 2.13) and total thermal conductivity equation (Eq. 2.11):

$$zT = \frac{S^2 T \sigma}{LT \sigma \kappa_{ph}} = \frac{S^2}{L} \cdot \frac{\kappa_{el}}{\kappa_{el} + \kappa_{ph}} \qquad (2.15)$$

This shows that zT can be enhanced when $\frac{\kappa_{ph}}{\kappa_{el}} \ll 1$ implying a very low lattice thermal. Since the thermal transport in solids is described as " dissipation of vibrational energy between adjacent atoms through chemical bonds" [73] also called phonon transfer, the easiest way to lower the thermal conductivity can be done via phonon scattering mechanisms.

One method to obtain lower thermal conductivity is through distortion of unit cells which can be obtained by creating various types of defects in the lattice. The common types of defects that have significant effect on the thermal conductivity are structural imperfections, such as crystallite boundaries and dislocations. Randomness in distribution of different kinds of atoms in the crystal, as the one occurring in alloys and solutions of impurities, also lowers the thermal conductivity. When creating defects by introducing foreign atoms one should be mindful of their valence, mass, size and interaction with the original atoms. Foreign atoms of similar valence do not scatter free charge carriers but strongly scatters phonons due to difference in wavelengths of charge carriers and phonons. To maximize this effect, introduced atoms should be much larger and heavier than the original atoms.[73] Concentration of the defects needed to lower thermal conductivity is temperature dependant and relatively large concentrations of lattice imperfections will required to produce significant effects at hight temperatures where phonon scattering is the dominant mechanism. [49]

Continuing with the defects as main scattering agent, introduction of vacancies is yet another effective method. Those tend to be be more effective than foreign atoms as they can scatter phonons by virtue of both missing an atom and the interatomic linkages. Downside to this method is the possibility for vacancies to act as electron acceptors and modify the electronic transport properties. [73] Since both Seebeck coefficient and electrical conductivity are dependant on charge carrier transport and concentration introduction of vacancies can possibly worsen TE proprieties.

Another very effective scattering mechanism is the interface scattering. In general the phonon mean-free path cannot be shorter than the average inter-atomic spacing in a homogeneous system. In an inhomogeneous system, such as a soft superlattice or multiphase materials the inter-atomic spacing varies with the phase giving mean-free paths of multiple lengths. The key to achieve a successful interface scattering is to have neighbouring phases as different as possible. Most phonons can pass through the interface between dissimilar materials if those materials

have similar crystalline and elastic properties, but they will be reflected if the difference is large enough. This effect is also possible in single phase material with various crystallite sized and it will increase with decreasing grain size. Nanostructured materials can reduce phonon mean free path very effectively, however nanograins are also capable of reducing the electrical conductivity. Coherent interfaces prevent electron scattering because $l_{el} \ll l_{ph}$ and are a solution to preserving high electrical conductivity in a nanostructured material. [73]

In order to enhance the effect of boundary scattering in can be highly beneficial to combine it with forming of a solid solution of the material. This way more phonon frequencies will be targeted causing greater decrease in thermal conductivity. Grain boundaries are very efficient towards low-frequency phonons, especially at low temperatures. At higher temperatures, where phonon frequency increases, the short-range disorder introduced by solid solution proves to be more successful. In addition, charge carriers would not suffer from reduced mobility as they have much longer wavelengths than phonons. [40]

Two more methods that are very popular approaches and which focus on structuring on atomic level are resonant scattering and formation of hybrid crystals. Resonant scattering by localized rattling atoms is utilized in skutterudites and clathrates. Those structures have large voids that can be filled with rear earth or heavy metals that interact resonantly with low-frequency phonons, thus lowering lattice thermal conduction. [11] The basic idea of the hybrid crystal, on the other hand, formation of a complex crystal structure that can be regarded as being formed by building modules with different compositions and structural symmetries. Those building modules then have specific TE functions enabling decoupling of electrical and thermal transport and individual tuning of the parameters to attain a higher zT. [21]

Lastly, porosity has a significant impact on thermal conductivity, especially at lower temperatures. Pores, being voids that can be quite large in size will slow down heat propagation as the only mechanism applicable for heat transfer in an empty space is radiation. The radiative energy transfer is described by the Stefan-Boltzmann equation: [32]

$$Q = \epsilon \sigma T^4 \tag{2.16}$$

where Q is the heat transfer rate, ϵ is the emissivity of the material and σ is the Stefan-Boltzmann constant. From the T^4 term it is easy to see that the heat transfer rate is highly de-

pendant on the temperature and it will increase massively as the temperature increases. This means that for low-temperature applications, high porosity might be an easy method for lowering thermal conductivity, however it can become a disadvantage at high temperatures.

To illustrate how big impact porosity has on a thermal conductivity of a material, its contribution can be subtracted thorough Maxwell equation: [75]

$$\kappa_{dense} = \frac{\kappa_{measured}}{1 - 1.5V_o} \tag{2.17}$$

where V_o is the fraction of porosity, $\kappa_{measured}$ is the measured thermal conductivity and κ_{dense} is the thermal conductivity of completely dense material. This is only an approximation and it is viable for materials with spherical pores and no more than 10vol% porosity.

Lastly, in some mixed valence materials phonon scattering due to valence disorder can be observed. The phonons are assumed to be scattered when an electron pair in the d shell of an atom of one valence, f.eks. Ru^{2+} is transferred to a neighbouring atom of same element but different valence, Ru^{4+}. In this process of charge transfer of two electrons with opposite spin a phonon is scattered. [39] [76]

2.4   Energy conversion efficiency

In every heat engine, including the thermoelectric generator, the energy conversion efficiency is governed by the Carnot efficiency:

$$\eta_c = \frac{\Delta T}{T_h} \tag{2.18}$$

where ΔT is the temperature gradient and T_h it the temperature at hot end. This equation shows that for maximizing the Carnot efficiency a large temperature gradient is required.

In addition, efficiency of the thermoelectric generators, η is defined as the ratio between electric power P, supplied to the load, and the heat energy Q, provided at the hot junction. For simplicity, a generator can be seen as a single p- and n-type unicouple. Considering that (i) the Seebeck coefficients, the electrical and thermal conductivities are constant with temperature and (ii) the contact resistance at the cold and hot junctions is negligible. [11] The maximum
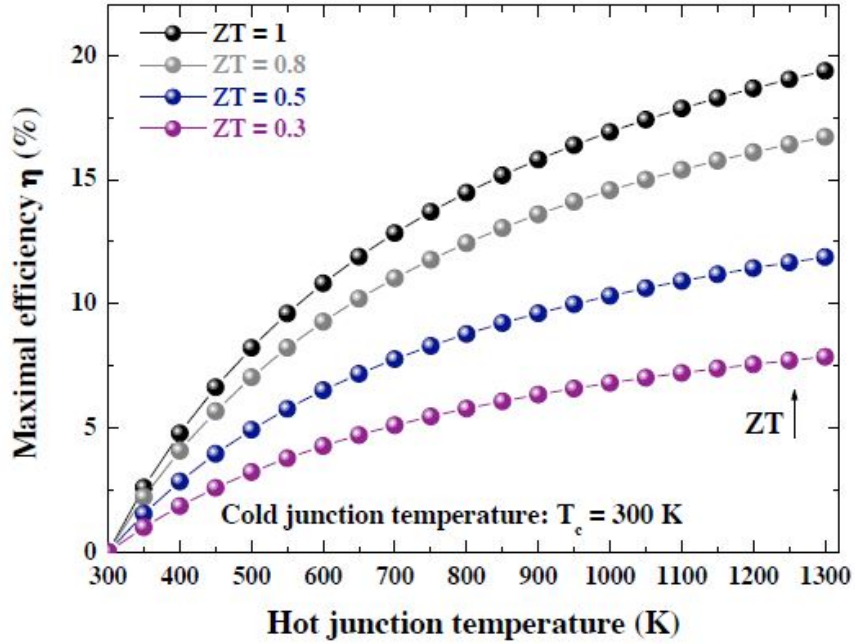
Figure 2.6: Maximal generating efficiency as function of the temperature at the hot junction and the figure of merit. [11]

theoretical efficiency, ϵ, for conversion of heat transferred from hot temperature, T_h to cold temperature, T_c through a material is: [16]

$$\epsilon = \frac{P}{Q} = \frac{T_h - T_c}{T_h} \cdot \frac{\sqrt{1 + z\bar{T}} - 1}{\sqrt{1 + z\bar{T}} - (T_c/T_h)} \tag{2.19}$$

where $\bar{T} = \frac{T_h + T_c}{2}$

To maximize power-generation efficiency, zT should be as high as possible, and the temperature differential between the hot and cold sides should be as large as possible. This relation is well illustrated in Fig. 2.6 However the large temperature difference lowers zT due to the Thomson effect should be included in calculations as explained in Section 2.2.

For practical applications zT = 1 is chosen as a benchmark as then the efficiency reaches approx. 10%. [45] Although it is less than more traditional technologies that can achieve 30% conversion efficiency [72] it still is a viable addition to traditional energy production techniques. In the end the goal is not to replace existing technologies but to provide a supplement that would reduce energy losses mainly in industry where they are largest.

2.5 Thermoelectric materials

2.5.1 State-of-the-art materials

Currently one of the most popular TE materials that are available on the marked are the tellurides. Those alloys are good at low temperatures (<450K, zT ≈ 0.8 to 1.1 [60]) when composed of $(Bi,Sb)_2(Te,Se)_3$ and medium-range temperatures (≈ 700K) when composed of PbTe or other group-IV tellurides (Ge, Sn). One specific example is Bi_2Te_3 with interesting features of its Seebeck coefficient depending on the composition. zT values up to 1.4 [30] can be obtained by tuning the carrier concentration via doping. Highest zT values for both n- and p-type group-IV tellurides were reported for alloys of $AgSbTe_2$ and they are greater than unity.[24] In high-temperature applications, meaning above 900 K, SiGe alloys are most used, both as n- and p-type materials. Unfortunately these materials exhibit relatively low zT as illustrated in Fig. 2.7.
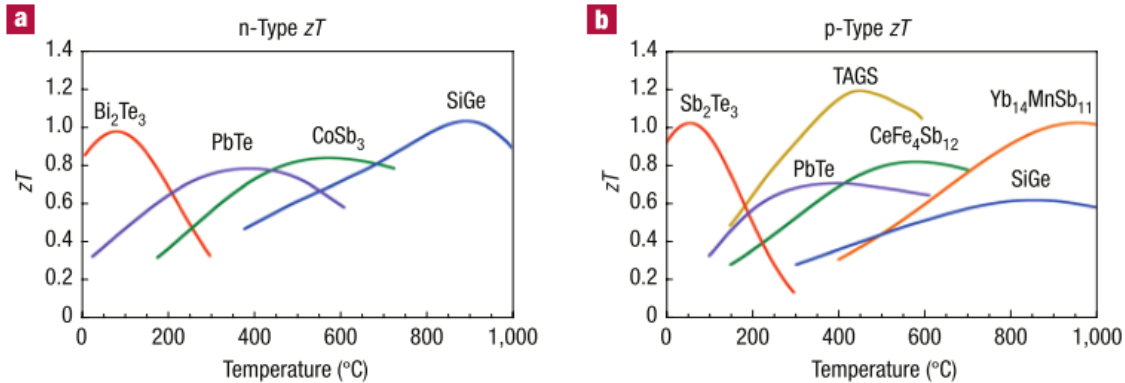
Figure 2.7: Figure of merit of the state-of-the-art materials for a)n-type and b)p-type [60]

The largest zT have been achieved with chalcogenites and skutterudites but their stability at high temperatures and under oxidizing conditions is poor and the toxicity if those compounds are a major issue. [35] Those problems are general issues for current state-of-the art materials hence the great interest in TE oxides.

2.5.2 Thermoelectric oxides

Work on thermoelectric oxides has started in early 1990s, as shown in Fig. 2.8, and resulted in many new promising candidates for both p- and n-type materials. So far the best p-type

materials are layered cobaltates with zT bit above 1 [56], placing themselves very close to the state-of-the-art materials. The n-type materials, on the other hand, are more challenging making development of oxide based TE devices more challenging.
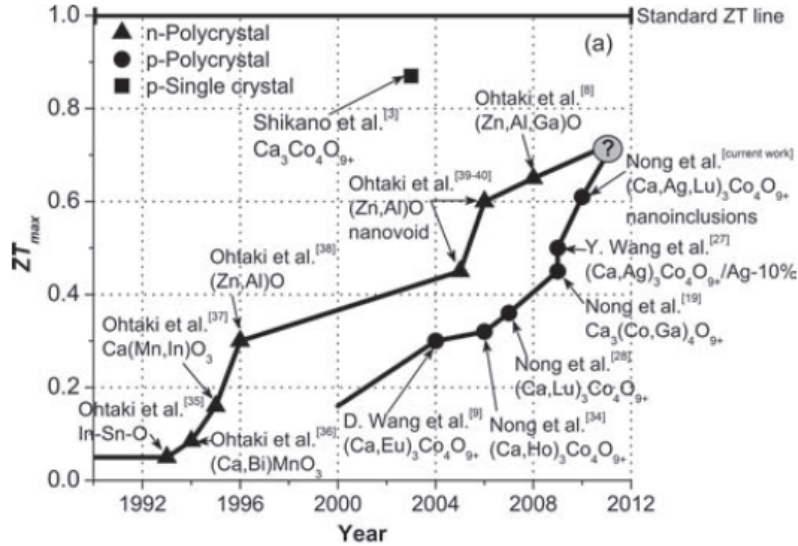

Figure 2.8: The historical developmental progress of n- and p - type polycrystalline oxide TE materials. [41]

In spite of relatively low zT, TE oxides have many advantages over state-of-the-art materials. First and foremost they are eco-friendly and cheap as they consist of highly abundant elements, Fig. 2.9. This is an important aspect as for any large-scale application, the cost of raw material and production costs are a major consideration after performance. [21] Further, the high chemical and thermal stability of oxides in oxidizing atmospheres makes it possible to use them in air without any special coating while a large temperature gradient is being applied. This somewhat compensates for low zT as it leads to a relative high device efficiency presented in Fig. 2.10. Lastly, oxides are chemically versatile and structurally intricate. This offers a great flexibility of structural and compositional tailoring through structuring or doping.

Unfortunately TE oxides are not without their drawbacks. First, the large electronegativity difference among the constituent elements leads to more ionic bonding, strong tendency for carrier localization, and strong scattering of carriers by optical phonons. Even for high mobility oxide semiconductors, $|S|$ is often found to be small because of the cancellation between the electron and hole band contributions. Moreover, the large bonding energy and the small mass of oxygen lead to a high velocity of sound and, therefore, high κ_l. [21]
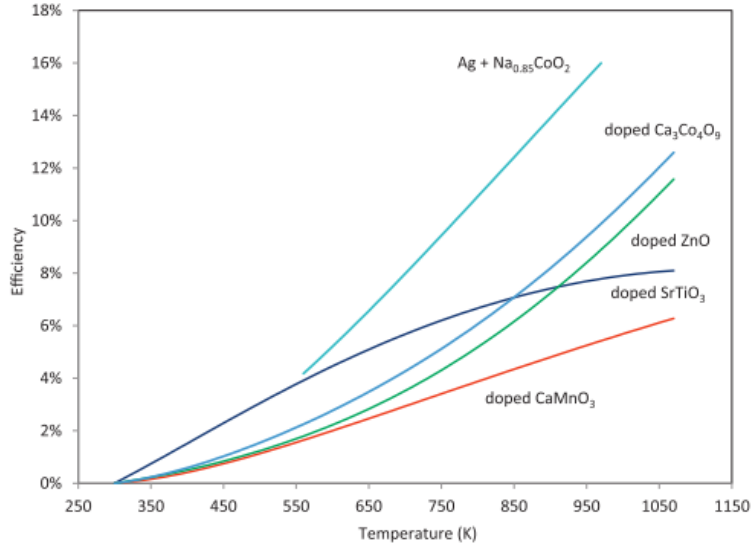
Figure 2.9: Element abundance in earth crest [19]

Perovskite-type materials

Perovskites have the general formula, ABO_3, where A is a cation (rare-earth, alkaline earth, al-kali) and B is a transition metal. The unit cell of a perovskite structure can be described in two different ways depending on the chosen A cation position, as illustrated in Fig. 2.11, with the (c) structure being the most commonly used.

Perovskite can exist in several different structures. The stability limits of a perovskite structure are expressed as Goldsmith tolerance factor: [32]

$$t = \frac{r_A + r_O}{\sqrt{2}(r_B + r_O)} \tag{2.20}$$

where r_A, r_B and r_O are ionic radii of A and B cations and oxygen anion respectively.

There are multiple crystal structures that a perovskite can form, as shown in Table 2.1, how-ever the t value usually lies between 0.80-1.10, when not taking temperature into consideration. The perfect cubic structure should have a t factor as close to 1 as possible and at least greater than 0.89. [26]

An ideal perovskite has a cubic crystal structure but it can deviate due to various distortion mechanisms such as: i)distortion of the octahedra, ii) cation displacements within the octahe-dra, and iii) rotation or tilting of the octahedra [11]. The last distortion mechanism is most com-

Figure 2.10: Maximum theoretical efficiencies for thermoelectric oxides using $T_C = 300K$ [16]

Table 2.1: Overview over Goldschmidt tolerance factors for perovskite structures. [58]

t-value	Structure
>1.10	Hexagonal stacking
0.89 >t >1	Ideal cubic perovskite
0.80 >t >0.89	Orthorhombic perovskite
<0.80	Ilmenite

mon and it yields the orthorhombic, so called GdFeO$_3$-type structure depicted in Fig. 2.12 a) while the relationship between orthorhombic and the perfect cubic unit cells is depicted in Fig. 2.12 b). All the structural distortions have strong influence on the microstructure and transport proprieties in perovskites. This gives the flexibility to tune TE proprieties by adjusting composition, oxygen content and mictrostructure of the material.

Calcium manganate

CaMnO$_{(3-\delta)}$ being an oxide in the perovskite family is a very well known and studied material. Interest in this material is caused by its structural proprieties that allow to tune the TE proprieties as well as the inherent proprieties of high thermal and chemical stability in oxidizing atmosphere. Solid solution between CaO and MnO, Fig. 2.13 makes structuring possible. Small deviations from 50/50 stoichiometry cause formation of new phases shown in Fig. 2.14. Many of
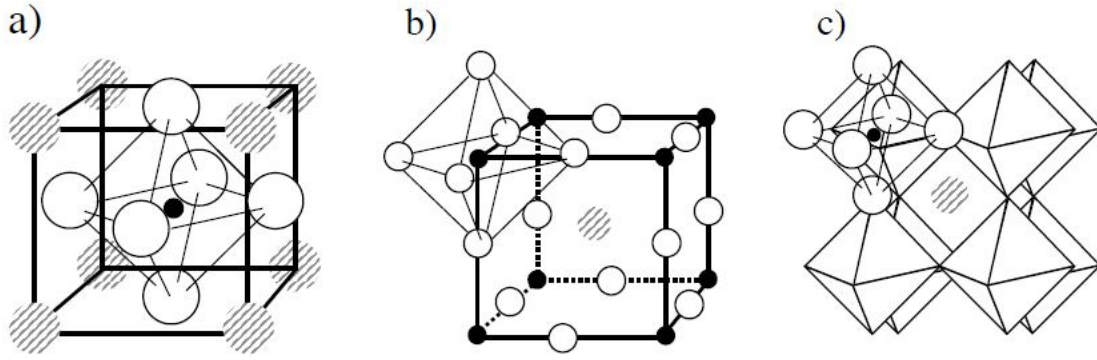
Figure 2.11: Different representations of the cubic perovskite structure where the A, B and O ions are represented by hatched, open and small black circles, respectively. The edges of the BO_6 octahedra are indicated by thin lines. a) A cations at the corners, b) A cations in the centre of the cell c) ABO_3 perovskite structure in a perspective view where the corner-sharing BO_6 octahedra surrounds the A cation. [11]

those phases have not been studied as potential TE materials and the few works that have been done always studied them as pure one phase materials and not in combination with $CaMnO_3$.

Crystal structure The perovskite structure, Fig. 2.15, provides many opportunities to finetune material's proprieties and lower the thermal conductivity. Firstly, the crystal structure is quite complex in itself and automatically suggesting low thermal conductivity. Further, the proprieties can be changed by introducing multiple types of point defects, such as substitution on A or B site or oxygen vacancies. As described in an earlier section, the perfect cubic perovskite structure undergoes various distortion mechanisms forming other related crystal structures. In case of manganate, it is structure depends on the temperature treatment with the structures as presented in Table 2.2. Also, the degree of
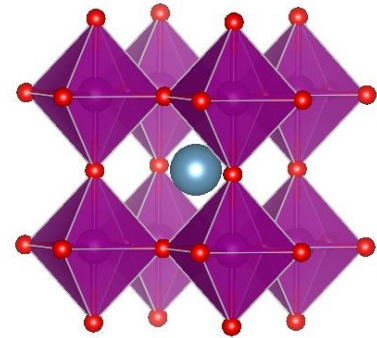

Figure 2.15: $CaMnO_3$ cubic perovskite crystal structure visualized with Vesta [36]

orthorhombicity increases with increasing δ, i.e. with increasing tolerance factor t. As the Mn^{4+} content increases in the $CaMnO_3$, the structural distortion decreases and a more cubic structure is obtained. [34] The fully oxidized $CaMnO_3$ had a t value of 1.004, i.e. it is cubic. However when the oxygen content as well as the manganese oxidation state changes from 4+ to 3+, the t value will decrease and come within regime of orhtorhombically distorted perovskites. Having
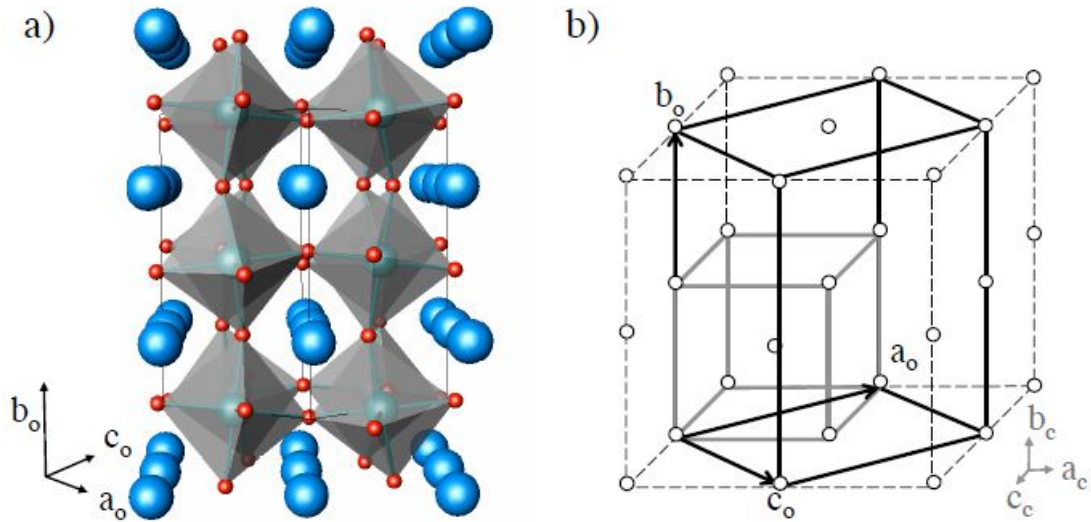
Figure 2.12: Schematic representations of a) an orthorhombic crystal structure and b) an orthorhombic unit cell (black lines) derived from a pseudo-cubic one (grey lines). Blue spheres correspond to A-sites, green spheres to B-sites, and red spheres to oxygen.[11]
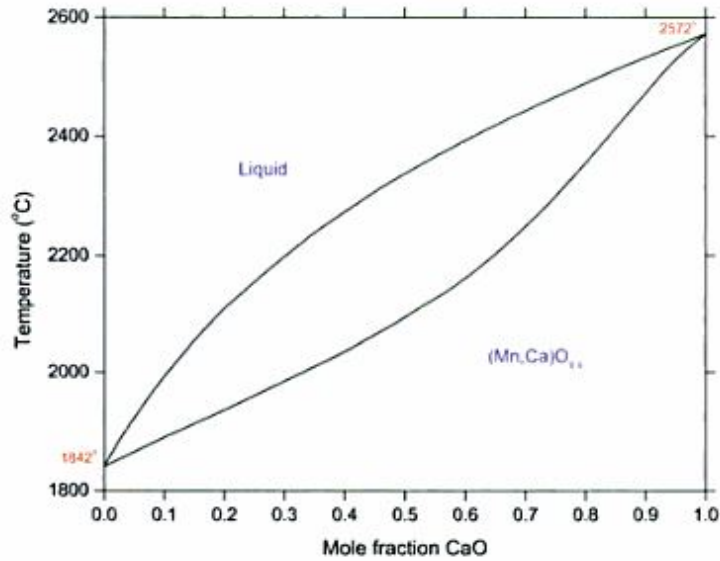

Figure 2.13: CaO-MnO solid-solubility phase diagram [46]

a mixed valence of Mn-atoms might be beneficial as it should lower the thermal conductivity and enhance the electrical conductivity. This also suggests that some oxygen deficiency might be desired as it affects the oxidation state of Mn.

In addition to change of structure with oxygen stoichiometry, two types of distortions, co-operative rotation of MnO$_6$ octahedra and co-operative Jahn-Teller distortion, can be observed
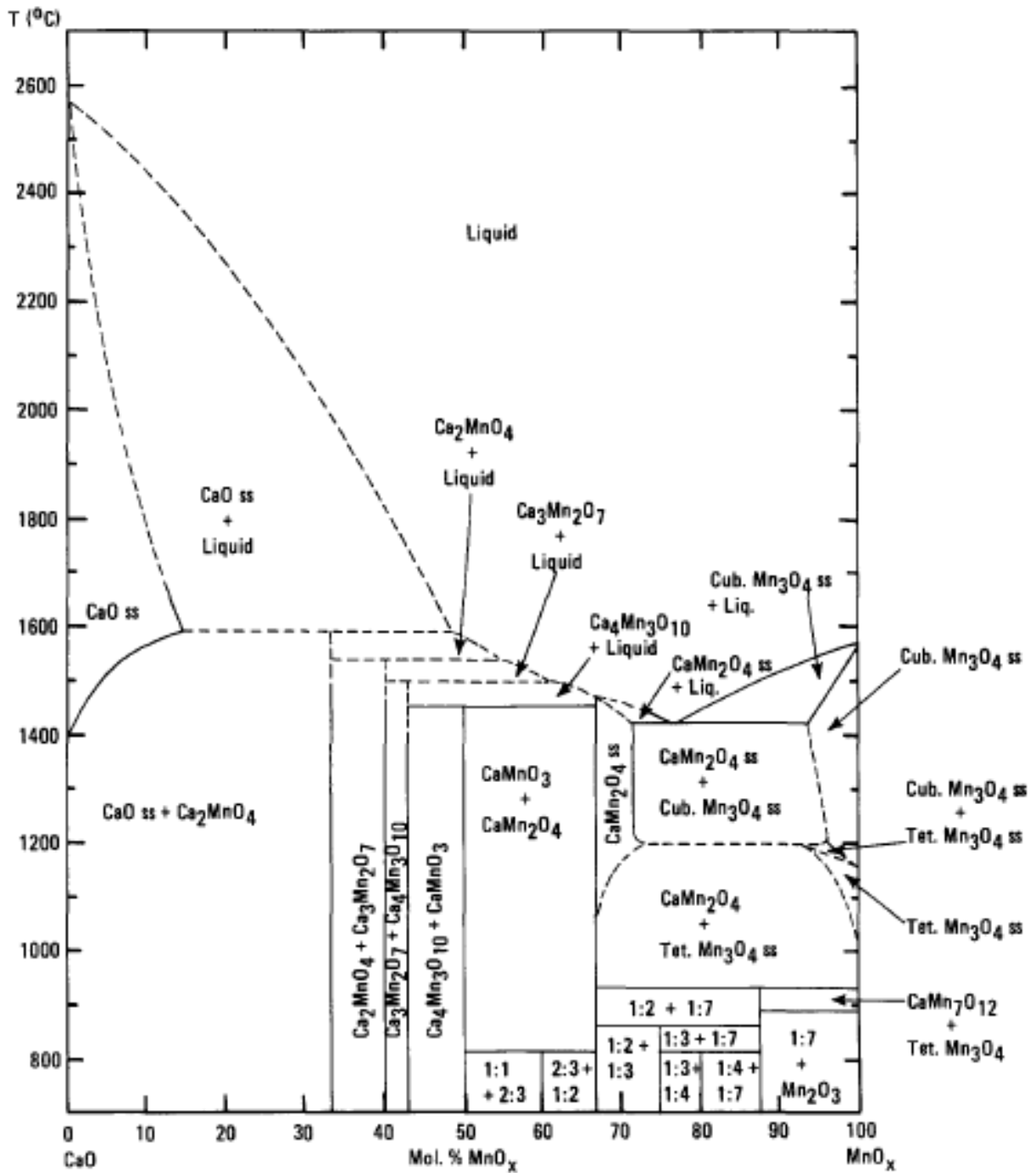
Figure 2.14: CaO-MnO phase diagram. [23]

Table 2.2: Phase transition and cell parameters of stoichiometric calcium manganate [62]

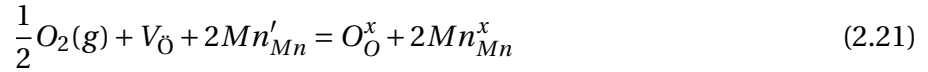| Structure	a [nm]	b [nm]	c [nm]	Temp. range [oC]
Cubic	0.3774	-	-	> 913
Tetragonal	0.5333	-	0.7534	896 - 913
Orthorhombic	0.5282	0.5265	-	< 896

in this CMO. Those two mechanisms are the ones that are responsible for formation of the tetragonal and orthorhombic perovskite structures at lower temperatures. [11]

Defect chemistry and electrical proprieties   The undoped $CaMnO_3$ is a poor n-type semiconductor. The obtained conductivity values differ significantly in the literature ranging from 10^{-2} to 6.3 Scm^{-1} at room temperature[12], depending on the precursors, synthesis route and microstructure.

Materials conductivity and also Seebeck coefficient depends on the charge carrier concentration which in this case is affected by the oxygen stoichiometry, δ. In addition, it was observed that the conductivity is dependant on the structure, degree of distortion and Mn oxidation state. It decreases with increasing distortion [34] as the conduction paths are diverging more and more from the ideal cubic structure.

On the other hand, multiple oxidation states of Mn-ions enhance the electrical conductivity. As the δ increases the mobility and concentration of free electrons left after removal of an oxygen atom and the reduction of Mn^{4+} to Mn^{3+} increases. The highest conductivity in undoped materials was observed in $CaMnO_{2.75}$ where Mn-ions coexist in both oxidation states in equivalent molar ratios.[15] Nevertheless, after the threshold of $\delta \approx 0.25$ the conductivity decreases due to lack of charge neutrality with so many free charge carriers. [57] An oxygen vacancy has a charge of +2 relative to the perfect lattice ($V_{\ddot{O}}$ in Kröger-Vink notation). This charge has to be compensated by point defects, Mn^{3+} on Mn^{4+} sites with a relative charge of -1 (Mn'_{Mn})to retain charge neutrality.[7] Those defects tend to order themselves further affecting electrical conductivity by forming paths along which current can be conducted, like in zig-zag or line formation or bromnmillerite-like structures with insulating planes. [35]

The defect proprieties of $CaMnO_{(3-\delta)}$ can be described by two chemical reactions:

$$\frac{1}{2}O_2(g) + V_{\ddot{O}} + 2Mn'_{Mn} = O_O^x + 2Mn_{Mn}^x \tag{2.21}$$

$$2Mn_{Mn}^x = Mn'_{Mn} + Mn_{Mn}^{\cdot} \tag{2.22}$$

where the first reaction correspond to the filling of oxygen vacancies and oxidation of Mn-ions and the secon reaction is the thermal excitation of electronic charge carriers across the band-gap.[57]

Generally speaking conductivity decreases with decreasing temperature, while at any fixed temperature conductivity will increase with the increasing O-vacancy up to δ equal to about 0.25.[13] The impact of δ onto conductivity and Seebeck coefficient is illustrated in Fig. 2.16.
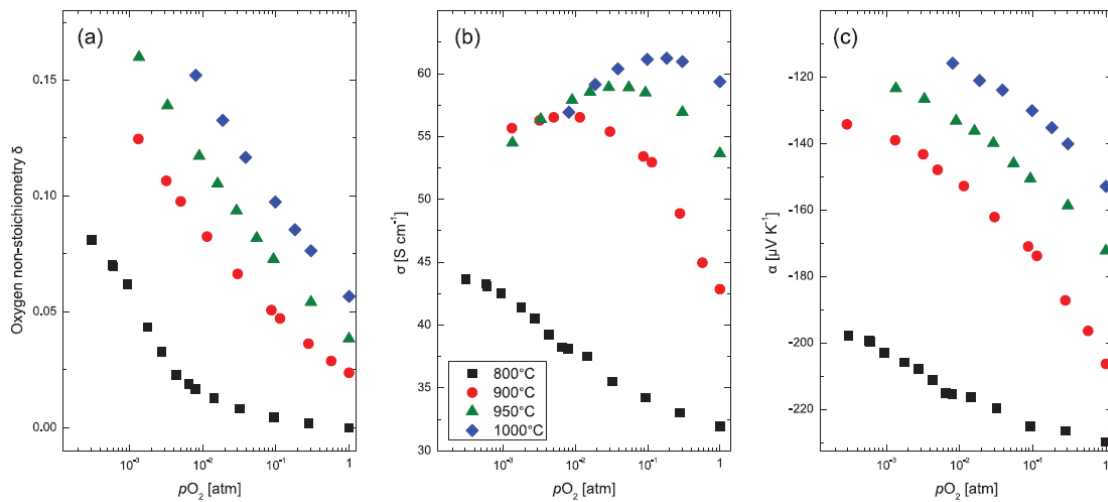

Figure 2.16: a) Oxygen nonstochiometry δ, b) electrical conductivity σ, c) Seebeck coefficient α of CaMnO$_{3-\delta}$ as at different oxygen partial pressures and temperatures [57]

In addition to affecting electronic proprieties, oxygen vacancies affect the bulk of the material leading to an an expansion of the crystal lattice, so called chemical expansion. It is most pronounced in perovskites with mixed valence elements because they can easily accommodate for the missing bonds caused by the two additional electrons left by the missing oxygen.[7]

Conduction mechanism   The conduction mechanism in calcium manganate is described as small polaron hopping mechanism, Fig. 2.17. Conduction electrons polarize the surrounding crystal lattice by strong electron-lattice interactions, localizing themselves on the lattice points
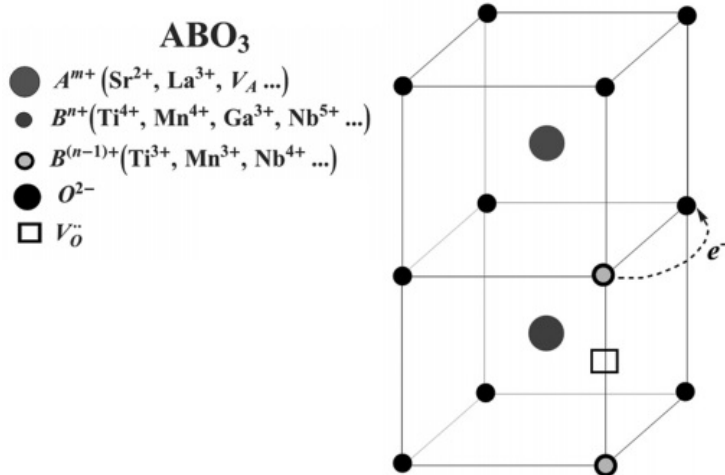
Figure 2.17: Schematic of Small polaron hopping mechanism. [38]

and inducing lattice distortion. Those localized electrons are called small polarons and they travel by a hopping mechanism. [45] This lattice distortion is induced by the Coulomb interaction between the carrier and the polarized crystal lattice. Small polaron hopping mechanism is mediated by ligands between Mn-ions of different oxidation states. In Mn^{3+}/Mn^{4+} mixed-valence manganates, it can be described as a simultaneous transfer of (i) an electron from the Mn^{3+} site to the oxygen anion and (ii) an electron from the oxygen anion to the Mn^{4+} site, as illustrated in Fig. 2.18 This mechanism is called the Zener's double exchange mechanism.
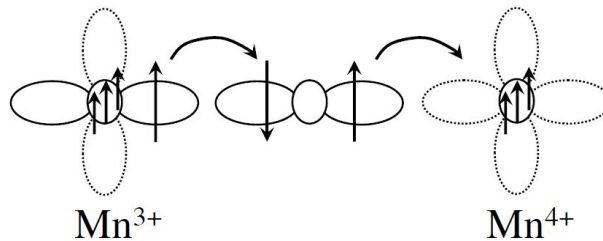

Figure 2.18: Schematic illustration of Zener double exchange mechanism. The Mn ions are represented by a small circle for the t_{2g} orbitals and lobes for the e_g orbitals. The 3d electrons are indicated by their spins. The three t_{2g} electrons are assigned as core spins. Empty e_g orbitals are indicated by dotted lines. [11]

Due to the ferromagnetic effective interaction between the two Mn-sites participating in conduction, two high spin clusters will be formed, where the extra electrons move relatively free. [13] The density of clusters increase with increasing oxygen-vacancy concentration thus

leading to increase in electrical conductivity. The temperature dependence of the conductivity suggests that this hopping is thermally activated. [13] In general, the mechanism results in the carrier mobility much lower that that for band conduction. [45]

Thermoelectric proprieties   Seebeck coefficient is dependant not only on carrier concentration, as described in Section 2.2.4, but also on the crystal structure of the material. The absolute value of Seebeck coefficient decreases continuously with increasing δ as it is expected for an increasing charge carrier concentration. Further, it changes steeply with charge carrier concentration in the orthorhombic phase and flattens out in the cubic phase. [57] Lastly it was observed that S decreases in absolute value as the temperature increases. For improved S the best composition is the partially doped CMO with a zig-zag arrangement of oxygen vacancies.[35]

The total thermal conductivity of calcium manganate with a sub-microcrystalline structure is very low compared other, similar compounds. This observation can be related to the twinned domains, which are frequently observed in orthorhombic perovskite-type structures. Twinning phenomena occur when orthorhombic unit cells can grow in different directions accommodating slight discrepancy between lattice parameters. The lattice thermal conductivity (phononic part) accounts for 90% of the total thermal conductivity in these materials. This leads to the assumption that the heat is carried predominantly by phonons.[29]

The most popular way to enhance TE proprieties of this materials is through doping that can be done on either site. A study of several lanthanide dopants demonstrated that ytterbium doping was most effective in increasing zT through reduction of the thermal conductivity and increase of the electrical conductivity and Seebeck coefficient.[16] Overview over zT change with doping is illustrated in Fig. 2.19. $CaMn_{0.08}Nb_{0.02}O_3$ samples produced with a soft chemistry exhibit zT values of 0.3 at 1070 K which are one of the highest values obtained for this material.[29]
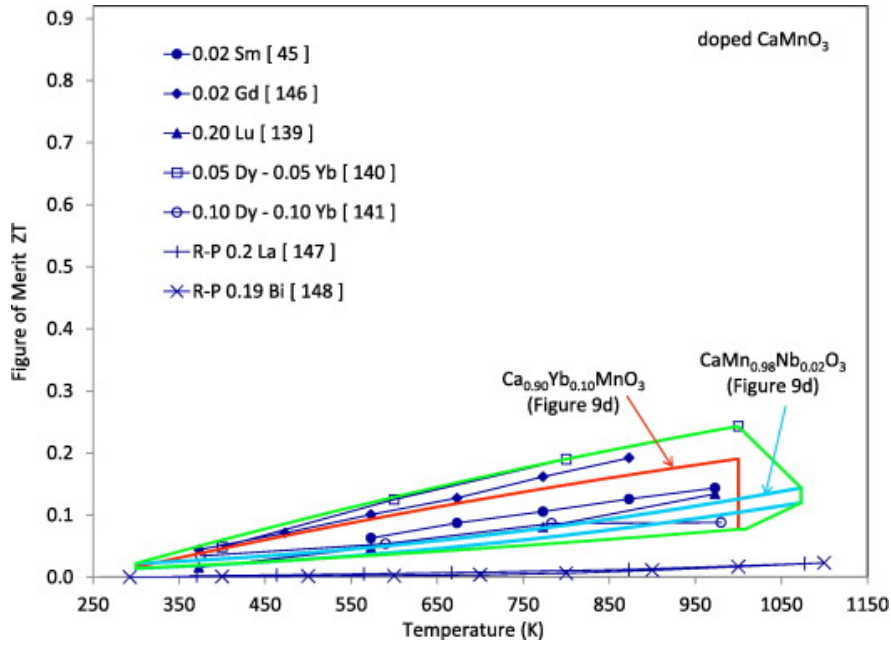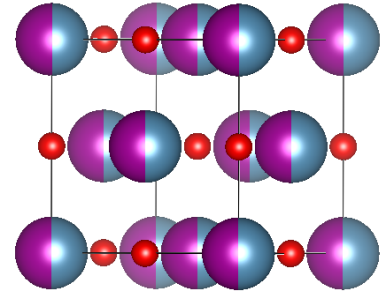
Figure 2.19: zT values for doped $CaMnO_3$ [16]

$Ca_{0.5}Mn_{0.5}O$

The starting single phase material formed in reducing atmosphere is $Ca_{0.5}Mn_{0.5}O$ also denoted as $CaMnO_2$. It has a rock-salt crystal structure with Ca and Mn occupying every second corner and center-face sites and oxygen atoms occupying all edges, as shown in Fig.2.20. Material has a light green colour due to Mn^{2+} [18] and the theoretical density of $4.25g/cm^3$ [68].

Figure 2.20: Crystal structure of $Ca_{0.5}Mn_{0.5}O$ simulated with Vesta. Ca and Mn atoms are shown with 50% occupancy rate just for illustrative purposes.

The solid solution between CaO and MnO leads to formation of rock-salt structure due to its simplicity and similar ionic radii of Ca^{2+} (1Åwith coordination number (CN) 6 [5]) and Mn^{2+} (0.83MnÅfor CN=6 [5]). This small difference enables Ca- and Mn-ions to occupy same sites in the crystal structure.

CaMn$_2$O$_4$

CaMn$_2$O$_4$, commonly known as marokite is a secondary phase
that forms from the CaO-MnO ss at temperatures above $\approx$850°C
when the MnO content is between 50 and $\approx$66%, see Fig. 2.14.
At room temperature it has a spinell structure with cell parame-
ters: a = 3.1540Å , b = 9.988Å and c = 9.6775Å [77], as illustrated
in Figure 2.21. In this structure the transition metal, Mn, is oc-
tahedrally coordinated with MnO$_6$ octahedra sharing edges and
corners and forming channels providing 8-coordinated sites for
the larger Ca-atoms. [77] Same Jahn-Teller distortion of MO$_6$ oc-
tahedra occupied by Mn^{3+} is observed in this structure as it is in
the orthorhombically distorcet CaMnO$_3$ perovskite. This mate-
rial is highly insulating at room temperature and has a theoretical
density of 4.68g/cm^3 [70] .

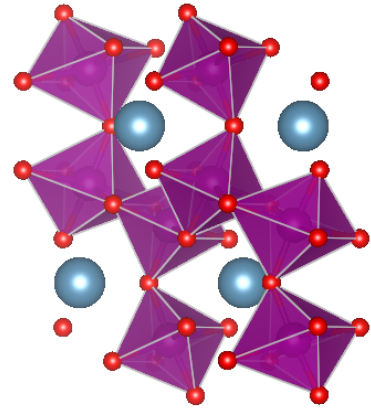Figure 2.21: Crystal struc-
ture of CaMn$_2$O$_4$ visualized
with Vesta.

Phase transformation

Transformation of Ca$_{0.5}$Mn$_{0.5}$O into CaMnO$_3$ is a very fast reaction as it follows the topotactic
reaction mechanism. Gunter defines a chemical reaction of a solid as topotactic "if the product
is formed in one or several chrystallogaphically equivalent orientations relative to the parent
crystal, if there has been an exchange of components with the surroundings, and if the reaction
can proceed throughout the entire volume of the parent crystal." [20] This reaction is caused by
low nucleus formation energy due to specific crystal orientation and can be cause by: i) Con-
servation of certain structural elements of the parent phase reducing necessity for major atom
rearrangement or ii) Epitactic nucleation, due to some correlation between the two involved
structures. [20]

The first step in this reaction and the most important one is oriented nucleation. Small
crystals with the perovskite structure and composition are formed on the surface of the NaCl-
structure. Ca$_{0.5}$Mn$_{0.5}$O is being used as a "substrate" for formation of the nuclei, making the
process much easier as stand alone nuclei do not have to be formed and the cationic arrange-
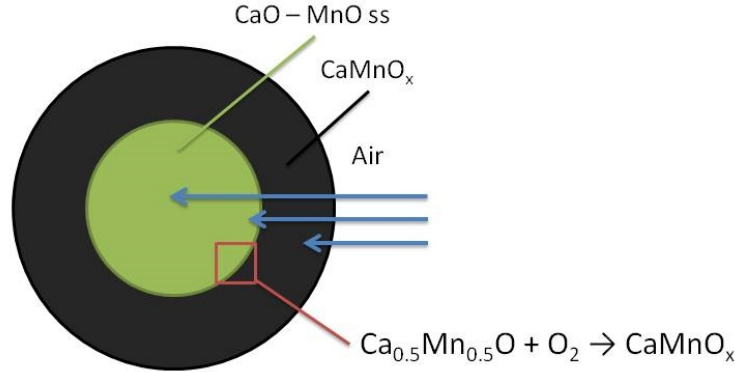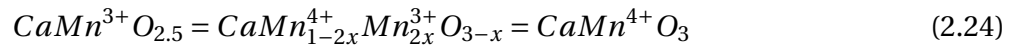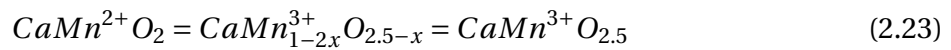
Figure 2.22: Schematic illustration of shrinking core

ment in both structures is identical. This allows nuclei to cross the critical size much easier and grow at a much faster rate.

Growth of the nuclei, which is the second step, is initially very fast however it will slow down with time as the diffusion length will grow. In case of this particular transformation, oxygen is needed to form $CaMnO_3$. Those additional atoms are coming from atmosphere and on the beginning of the reaction they are in close contact with the reduced phase through the sample surface. However as the perovskite starts to form, oxygen will have to diffuse further into the sample through already formed perovskite layer. This will slow down oxidation speed and lead to formation of so called shrinking core, Fig. 2.22.

This entire process can be described with following reactions:[51]

$$CaMn^{2+}O_2 = CaMn^{3+}_{1-2x}O_{2.5-x} = CaMn^{3+}O_{2.5} \tag{2.23}$$

$$CaMn^{3+}O_{2.5} = CaMn^{4+}_{1-2x}Mn^{3+}_{2x}O_{3-x} = CaMn^{4+}O_3 \tag{2.24}$$

This shows that intermediate phases with lower oxygen stoichiometry will be formed before the desired perovskite is synthesised.

Looking at the reaction on atomic level and relationship between the rock-salt and perovskite structure we can observe many similarities as pointed out before. The Ca and Mn atoms are alternating in an ordered 1:1 sequence in both structures and the cationic subcell remains nearly unaltered throughout the reaction. Occurring changes come from oxidation of Mn^{2+} with

ionic radius of 0.83Åto Mn^{3+} and Mn^{4+} with ionic radius of 0.58Åand 0.53Årespectively [59]. This leads to change in bond lengths and the cation site occupied by the Ca-ion becomes enlarged because the anions shift towards surrounding cations. [5] Fig. 2.23 illustrates the relationship between the rock-salt structure and the forming perovskite structure.
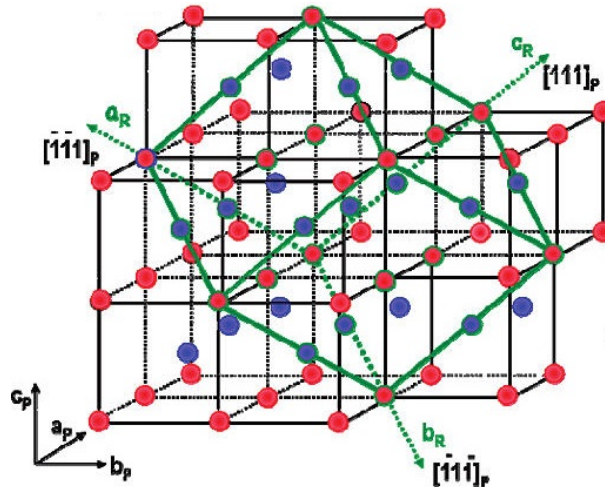

Figure 2.23: Schematic representation of relations between rock-salt and rhombohedral structures. Oxygen anions omitted for clarity. [65]

Density improvement

Density of a ceramic material is a very important propriety as it has an impact at TE proprieties. In case of solid state sintering, densification of the material occurs through volume diffusion which in extend leads to shrinkage of material. The driving force in this process is the difference in free energy between the free surfaces of particles and the points of contact between neighbouring particles. [52]

To increase density of the material the particle size and shape as well as temperature and time of sintering have to be adjusted. Small particles are desired as they sinter faster and at lower temperatures. Further uniform preferably spherical particles increase green body density through better packing which is further improved by narrow particle size distribution. Next to particle size, sintering temperature is the most important parameter enhancing the density due to its relationship with the diffusion coefficient and by providing the necessary energy to drive the reaction.

Chapter 3

Experimental

3.1   Apparatus and Chemicals

Single phase rock-salt precursor powder was synthesized by the solid state method. Chemicals used during this synthesis and characterization, their formula, supplier and purity are shown in Table 3.1

Table 3.1: List of chemicals used during solid state synthesis, their formula, supplier and purity

Chemical	Formula	Supplier	Purity
Calcium carbonate	$CaCO_3$	Sigma-Aldrich	For analysis
Manganese(IV) oxide	MnO_2	Sigma-Aldrich	>99%
Ethanol	CH_3CH_2OH	VWR International AS	99.8%
Isopropanol	C_3H_8O	VWR International AS	>99%

5% H_2 in Ar from Varigon was used as reducing atmosphere. Nitrogen or argon and synthetic air as respectively inert and oxidizing atmospheres supplied by AGA were used to anneal the precursor powder and obtain $CaMnO_3$ with and without secondary phases. The different apparatus used during in this project are listed in Table 3.2, together with model and application area.

Table 3.2: List of apparatus used to in synthesis and characterization together with their model and area of application

Apparatus	Model	Application
Planetary ball mill	Retsch PM 100	Mixing an milling of powders
Rotavaopur	Buchi Rotavapor R-210	Drying of wet powders
Tubular furnace	Entech Nabertherm P330	Synthesis, sintering and annealing
Furnace	Nabertherm P330	Low temp. oxidation
Flow meter	Brooks Model no.1355	Control of gas flow through the furnace
Uni-axial press	Hydraulic C-press	Pressing of pellets
Cold Isostatic Press	Autoclave Engineers	Densification of green body pellets
XRD	Bruker AXS D8-Focus Bruker D8 Advance DaVinci	Study of phase composition
SEM	Hitachi S-3400N	Miscrostructure and phase composition
Dilatometer	Netzsch DIL 402C	Sintering and annealing analysis
TGA	Netzsch STA 449C	Oxidation analysis
Optical microscope	Leica MEF4M	Study of microstructure
Grinder	Struers Tegramin-20	Polishing of samples
BET	Micromeritics Tri Star 3000	Surface area measurement
Sputter coater	Edwards S150B	Gold-plating of samples for SEM

3.2 Procedure

For the purpose of the report the procedure was divided into four steps:

1. **Synthesis of powder precursor** Synthesis of single phase $Ca_{0.5}Mn_{0.5}O$ (rock-salt structure) in a reducing atmosphere. This step involves preparation of raw powder at reducing conditions and its post-reduction treatment. Obtained material is used as a starting point for further synthesis.

2. **Sintering of dense bodies** Improvement of sintering parameters to obtain material with density $\approx$90% of $Ca_{0.5}Mn_{0.5}O$.

3. **Annealing** Oxidation in air to form $CaMnO_3$ and desired secondary phases.

4. **Characterization** Characterization of materials microstructure, composition and TE proprieties.

The synthesis procedure was loosely based on previously published methods. [50] [34] [57] It should be noted that the details provided in following sections are the optimized conditions

to obtain desired material. Optimization of the parameters was a big part of the work and the results of different approaches are described in Section 4.

3.2.1 Synthesis of powder precursor

Single phase $Ca_{0.5}Mn_{0.5}O$ is used as a starting point for all sintering and annealing. Its synthesis consists of three steps: i) preparation of raw powder, ii) synthesis in reducing atmosphere through reaction sintering and iii) processing involving milling in sieving. What is understood as a powder precursor is a single phase $Ca_{0.5}Mn_{0.5}O$ that has a rock-salt structure and that was milled, dried and sieved. The entire process is illustrated in Fig. 3.1 and described in further detail in following paragraphs. Preparation of raw powder and synthesis of single phase $Ca_{0.5}Mn_{0.5}O$ in reducing atmosphere was optimized during specialization project fall 2014. [33]

Preparation of raw powder Powders of $CaCO_3$ and MnO_2, as received from Sigma-Aldrich, were weighted and mixed in accordance with desired stoichiometry. Both powders were milled in a planetary ball mill for 30min at 175rpm in a 250mL zirconium milling jar with 15 Yttrium stabilized zirconia (YZT) 10mm in diameter milling balls. Approximately 80mL of ethanol corresponding to approximately the third of the volume of the jar was added to aid mixing. Wet powder was firstly dried in a rotavapour to remove most of the solvent and its remains were evaporated on a hot plate. Raw precursors were milled together not only to mix them but also to break up the agglomerates and even out the particle size as both precursors differ greatly in size, with MnO_2 particles begin much larger than $CaCO_3$ (see Fig. A.1)

Synthesis of $Ca_{0.5}Mn_{0.5}O$ Raw, mixed powders were pressed on a uni-axial double action press at 100MPa. Obtained green body was heated up in a reducing atmosphere, 5% H_2 in Ar, in a horizontal tubular furnace. The synthesis was conducted at 1250°C with 200°C/h heating and cooling rate and dwell time of 6h. Material composition was checked by XRD, by crushing pellets into powder to analyse the bulk material. If secondary phases were detected, obtained powder was pressed again and fired in the furnace for the second time at the same conditions.
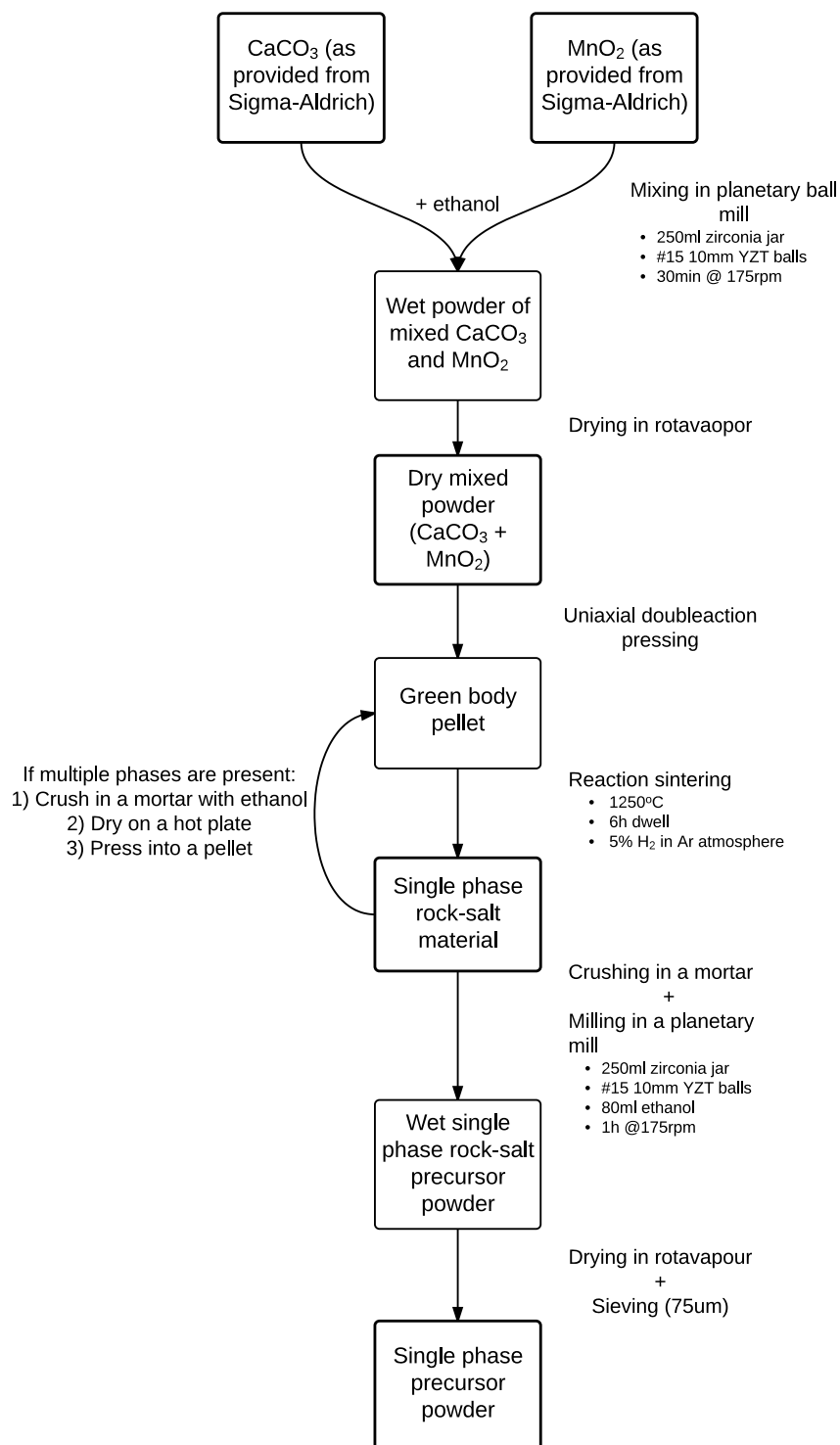
Figure 3.1: Flowchart illustrating powder precursor synthesis process.

Processing of single phase rock-salt material In order to obtain precursor powder, obtained single-phase rock-salt pellets were first crushed in a mortar and then milled in a planetary mill for 1h at 175rpm. Same milling media as for preparations of raw powder were used to mill the rock-salt material (i.e. 250mL zirconium milling jar with 15 YZT $\varnothing$10mm milling balls and ≈80mL of ethanol). Obtained wet powder was first dried in rotavapour and then on a hot plate to remove all solvent. Obtained dry powder was sieved through a 75μm sieve to remove all big particles and form soft agglomerates. The sieved powder is then used as precursor powder for all future processes.

3.2.2 Sintering of dense bodies

Precursor powder was first pressed on a uni-axial double action press with 100MPa pressure for several minutes and then in a cold isostatic press (CIP) at the pressure of 2kbar for approx. 2min. Pressed pellets were then sintered in reducing atmosphere in a horizontal tubular furnace at 1350°C for 12h with a heating and cooling rate of 200°C/h. Pt wire was used as a spacer between the pellet and the alumina boat to prevent side-reactions. During heating, at 850°C atmosphere was shifted to pure nitrogen and flow, controlled with a flow meter, adjusted to maximum. Upon cooling atmosphere was changed back to 5% H_2 at 850°C to reverse any potential oxidation that could have occurred as illustrated in Fig. 3.2
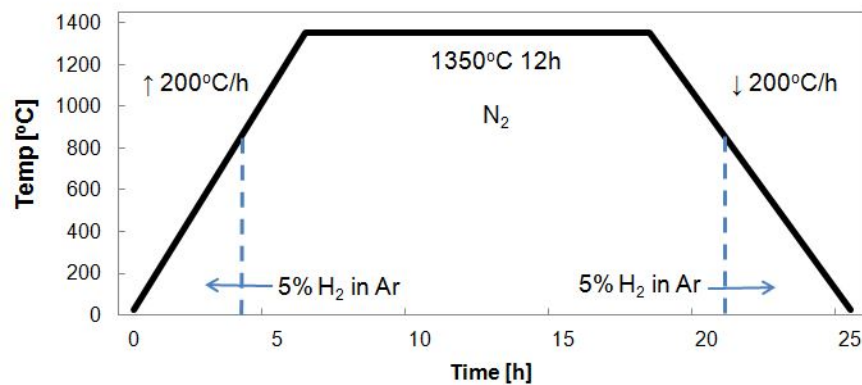

Figure 3.2: Schematic of heating program for sintering of dense bodies used for all samples with indicated heating (↑)/cooling (↓) rates and atmospheres. Dashed line indicates place where atmosphere is shifted.
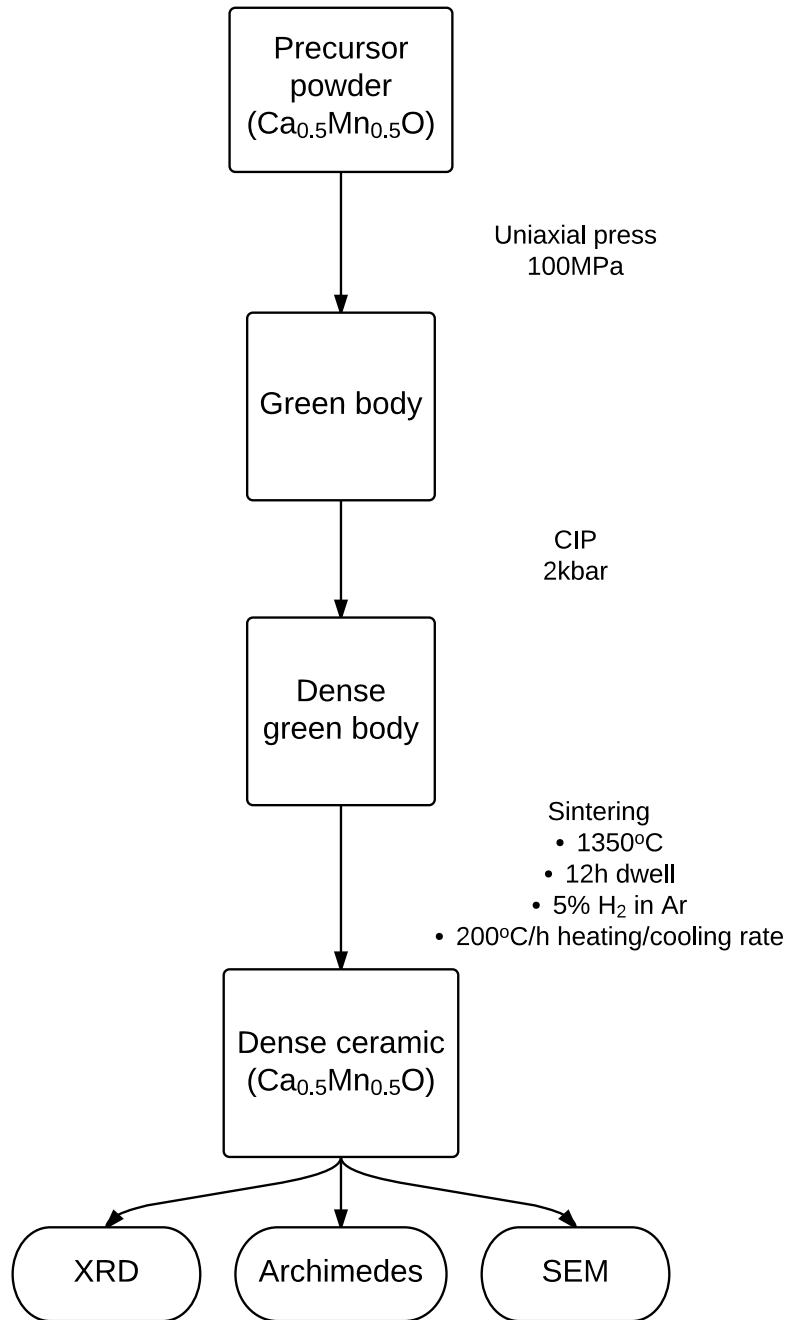
Figure 3.3: Flowchart illustrating the sintering process.

3.2.3 Annealing

Multiple annealing procedures were conducted to observe the relationship between heat treatment, microstructure and formation of secondary phases. The most suitable process involved heating up of the dense sintered pellet in 5% H_2 in Ar up to 1250°C at the rate of 200°C/h. Following, furnace is flushed with excess of an inert gas, either N_2 or Ar, before atmosphere is shifted to synthetic air. The amount and time needed for flushing were determined by calculating the volume of the furnace and using a flow meter to ensure maximum flow through the furnace at all times. Change of atmosphere from inert to oxidizing (synthetic air in this case) marks the start of the annealing process. The oxidizing atmosphere is used till the end of the process, including cooling at the rate of 120°C/h. The entire heating program is illustrated in Fig. 3.4.
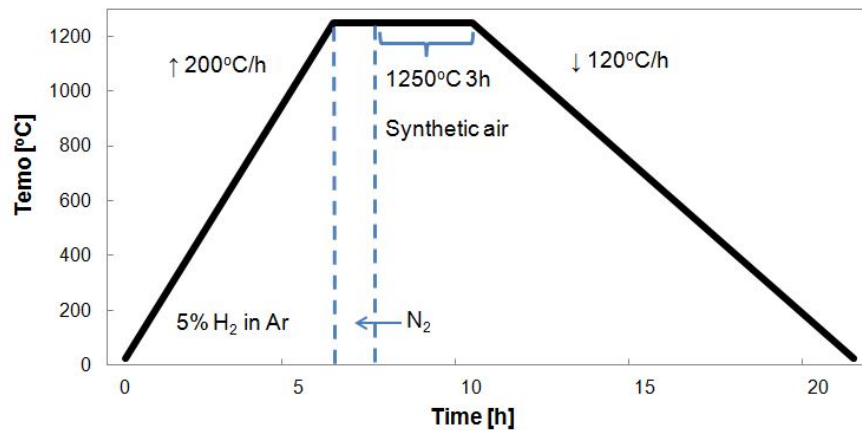

Figure 3.4: Schematic of heating program used for annealing of the samples with indicated heating (↑)/cooling (↓) rates and atmospheres. Dashed line indicates place where atmosphere is shifted.

3.3 Summary

Table 3.3: Overview over entire synthesis procedure with details involving each step

Phase	Steps involved
1. Production of powder precursor	1. Mixing of precursor powders in planetary mill - $CaCO_3$ + MnO_2 in desired ratio + 80ml ethanol - 250ml zirconia milling jar - 15 $\varnothing$10mm YZT milling balls - 30min at 175rpm 2. Drying of mixed powder in rotavapor and on a hot plate 3. Pressing into pellets on an uniaxial double-action press at 100MPa 4. Reaction-sintering in reducing atmosphere - 5% H_2 in Ar - 200K/h ramp up/down - 6h dwell - max. temp. 1250°C 5. Check phase purity - XRD - If multiple phase present i) crush in a mortar ii) press into pellets iii) refire using previous heating program 6. Milling in planetary ball mill - Reduced powder crushed with mortar + 80ml ethanol - 250ml zirconia milling jar - 15 $\varnothing$10mm YZT milling balls - 1h at 175rpm 7. Drying of milled powder in rotavapor and on a hot plate 8. Sieving with a 75μm sieve
2. Sintering of dense bodies	1. Pressing into pellets in a uniaxial double-action press at 100MPa for 5min 2. CIP at 2kbar for 2min 3. Sintering - 5% H_2 in Ar at temp below 850°C, N2 at higher temperatures - 200K/h ramp up/down - 12h dwell - max. temp. 1350°C - Pt wire as spacer between sample and Al_2O_3 boat
3. Annealing	1. Heat treatment in oxidizing atmosphere - 5% H_2 in Ar during heating - N_2 at max. temp to flush out H_2 - Synthetic air for the rest of the program - 200K/h ramp up, 120K/h ramp down - 3h dwell in air + dwell for flushing - max. temp. 1250°C

3.4 Characterization techniques

3.4.1 X-ray diffraction

X-ray diffraction (XRD) analysis was used to establish phase composition at all stages of the synthesis. XRD patterns were obtained from the bulk of the sample, by thoroughly grinding it in a mortar before placing it in a single crystal Si sample holder. Scans were performed between 20-80θ in either Bruker AXS D8-Focus or Bruker D8 Advance DaVinci instrument. Both instruments have a Cu source, however additional peaks caused by Cu-Kβ and W can be found in patterns produced by the DaVinci instrument. Obtained patterns were analysed in EVA software [1] and compared against patters found in the International Centre for Diffraction Data (ICDD) in order to obtain phase composition.

3.4.2 Scanning electron microscopy and Energy dispersive x-ray microscopy

Scanning electron microscopy (SEM) was used to inspect misrostructure and sample composition. All images presented in this thesis were taken with Hitachi S-3400N. During analysis the electron source is excited by high voltage and the resulting electron beam is aimed at the sample. This produces several different signals and the ones that were used for analysis: i) Secondary electrons (SE) - a result of excitation and replacement of outer shell electrons by the primary electrons enabling us to view microstructure of the sample; ii) Backscatter electrons (BSE) - inelastically scattered primary electrons. The energy loss is dependant on the weight of surface atoms electrons are interacting with giving an image of phase segregation; iii) Characteristic x-rays used in energy dispersive spectroscopy (EDS) - produced due to excitation by the primary electron beam and enable us to see the phase composition by determining its chemical composition as those x-rays atomic fingerprints. Aztec software [3] was used to process EDS images and determine sample composition. Samples used for BSE and EDS were polished under 1μm with Struers products. Chosen samples were thermally etched by heating the samples to 1000°C in air at heating and cooling rate of 200°C and no dwell time.

3.4.3 Archimedes density measurement

Bulk density and porosity was determined by Archimedes method described in ISO5017. Home made apparatus was used to conduct the measurement while isopropanol was the immersion liquid of choice.

Archimedes density measurement is based on measuring sample weight when it is dry (m_1), immersed (m_2) and wet (m_3). Porosity is then calculated by relating obtained masses to sample buoyancy and the density of the liquid through following equations:

$$\rho_{bulk} = \frac{m_1}{m_3 - m_2} \cdot \rho_{liq} \tag{3.1}$$

$$\pi_{open} = \frac{m_3 - m_2}{m_3 - m_2} \cdot 100 \tag{3.2}$$

$$\pi_{true} = \frac{\rho_t - \rho_{bulk}}{\rho} \cdot 100 \tag{3.3}$$

$$\pi_{closed} = \pi_{true} - \pi_{open} \tag{3.4}$$

$$\tag{3.5}$$

where ρ_t is the theoretical density of the material and ρ_{liq} is density of used liquid and Π is porosity.

3.4.4 Dilatometry

Dilatometry (DIL) is a method used to measure sample's dimension changes at given temperature. Netzsch DIL 402C with preprogrammed alumina standard was used in all analyses. Especially for DIL measurements samples of 5mm in diameter had to be pressed. For all measurements a standard heating and cooling rate of 2K/min was used while dwell time, maximum temperature and atmosphere was adjusted according to the needs. Obtained curves were used to gain insight into the sintering process, oxidation of the material and calculation of the thermal expansion coefficient (TEC). TEC, α, can be calculated using following formula: [32]

$$\alpha = \frac{\Delta dl/lo}{\Delta T} \tag{3.6}$$

where $\Delta dl/lo$ is the change in expansion over selected temperature range, ΔT

3.4.5 Other

In addition to the techniques described above, Thermogravimetric analysis (TGA), optical microscopy and Brunauer-Emmett-Teller measurement (BET) were conducted as a part of the characterization process.

TGA was used to determine oxidative proprieties of $Ca_{0.5}Mn_{0.5}O$ and gain insight into the phase transformation. In the measurement precursor powder powder was used. Heating and cooling rate as well as dwell time was the same as in the DIL measurements focused on the oxidative proprieties, i.e. 2K/min rate with dwell time of 7h and maximum temperature of 950°C. Synthetic air at flow rate of 30mL/min was the selected atmosphere.

BET method was used to approximate surface area of the $Ca_{0.5}Mn_{0.5}O$ powder obtained through different milling processes. Samples were pretreated by applying a combination of heat, vacuum, and flowing gas to remove adsorbed contaminants. Then they were cooled under vacuum before nitrogen, used as adsorptive was added in controlled increments. After each added dose, pressure was allowed to equilibrate before the adsorbed quantity was calculated. The quantity adsorbed at each pressure defines an adsorption isotherm, from which the quantity of gas required to form a monolayer on the particle surface is determined. With the area covered by each adsorbed gas molecule known, the surface area can be calculated. [4]

Since the model used to calculate surface area is based on spherical particles it was also assumed that produced powder is made up of spherical particles. This assumption will be discussed in detail in Section 5. Single particle size was calculated by using following formula: [31]

$$D = \frac{6000}{A_{BET}\rho} \tag{3.7}$$

where A_{BET} is the BET-surface area of the sample obtained through the measurement, ρ is the theoretical density of the material and D is the particle diameter.

3.5 Thermoelectric proprieties measurements

3.5.1 Seebeck measurement

The Seebeck coefficient measurements were performed with a Probostat device from NorECs AS illustrated in Fig. 3.5. Measurements were conducted every 100°C between room temperature and to 900°C in synthetic air with flow of 130ml/min. Approximately 3-4h dwell was set on each increment allowing the temperature and S-values to stabilize.

The Seebeck coefficient is determined by applying small temperature gradient over the sample and measuring temperature and voltage at its cold and hot ends. Those values, in combination with Eq. 2.2 give $S_{measured}$. To obtain Seebeck coefficient for the material, S_{sample} contribution from the thermocouples (Pt wire), S_{tc}, used as reference in measurement must be subtracted, hence

$$S_{sample} = S_{measured} - S_{tc} \qquad (3.8)$$

Special samples were prepared for the measurement. Dense bars with approximate dimensions 25mm × 2.4mm × 6mm were sintered and annealed according to procedure described in Section 3.2. All bars were polished prior measurement in order to remove any impurities formed on the surface and have a perfectly smooths surface ensuring good contact with the probes.

Figure 3.5: Schematic illustration of ProboStat used to measure Seebeck coefficient. [6]

3.5.2 Thermal diffusivity and conductivity measurement

Thermal diffusivity The thermal diffusivity of the samples were determined by using Netzsch LFA 457 MicroFlash instrument and the flash method developed by Parker [48]. It was performed in N_2-atmosphere with 100°C increments from room temperature to 500°C and 3 measurements per step. Special samples 0.5" in diameter and ≈2mm in thickness were prepared.
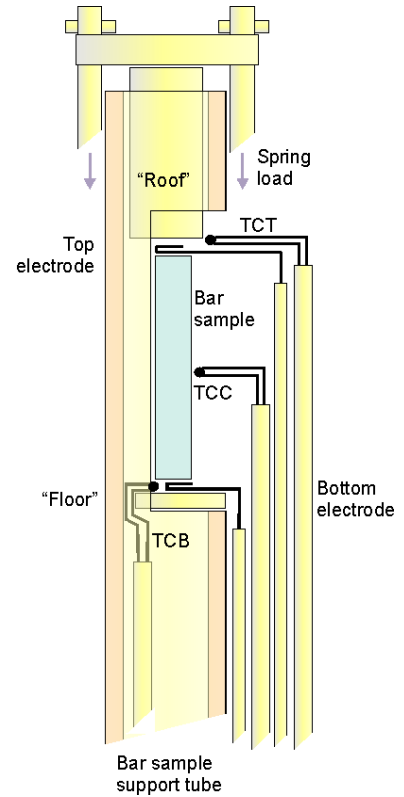
Right before the measurement sample surface was polished with a 500 grid Si polishing paper to remove any potential contamination. Lastly both sides were spray-coated with graphite to approximate the material to the black body condition. A material is considered a black body when: i) its surface absorbs light perfectly, and ii) it presents a high emissivity ($\varepsilon \approx 1$). This means that in practice the sample should not be transparent and it should be dark in colour, hence the carbon coating.

The measurement is done by irradiating the sample by a short heating pulse caused by the laser. It causes the temperature on the opposite side to rise and the temperature change is measured by an IR detector as illustrated in Fig. 3.6. After the laser pulse, the initial temperature raise decreases asymptotically till it reaches base temperature. Assuming adiabatic conditions, the time to reach half of the maximal temperature, so called "half time" ($t_{1/2}$), allows to determine the thermal diffusivity, α [48]:

$$\alpha = \frac{1.38 d^2}{\pi^2 t_{1/2}} \tag{3.9}$$

where d is thickness of the sample. Sample thickness is a very important parameter as it determines the time for the pulse to reach the other side. The pulse should reach the detector without any heat losses and without causing the half time to be shorter than the irradiation and detection time.

Thermal conductivity The Laser flash method determines the thermal diffusivity, α, and heat capacity, C_p of the material, which can be used to calculate the thermal conductivity, κ of the sample through following equation [48]:

Figure 3.6: Schematic representation of the laser flash method. Remastered from Bocher. [11]

$$\kappa = \alpha \rho C_p \tag{3.10}$$

To obtain the thermal conductivity values, the thermal diffusivity measurements were evaluated by using the Netzsch Proteus LFA analysis software and the data were corrected with Cowan model. Pyroceram 9606 which is a pyroceramic material made up of Corning and a
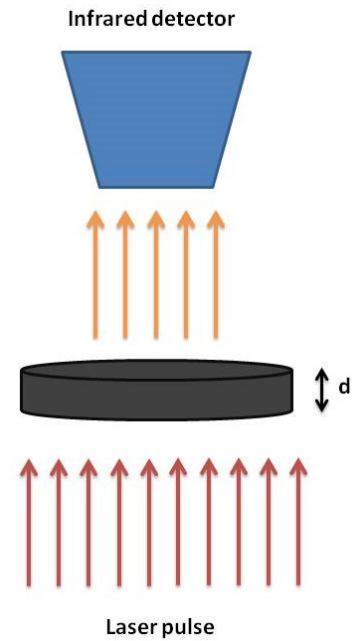
glass-ceramic material, supplied by Netzsch was used as a standard for the measurements.

3.5.3 Electrical conductivity

Electrical conductivity was measured through 4-point probe method. It was measured in air in a home-built set-up. Approximately 3-4h dwell time was set on each 100°C increment allowing the temperature and σ-values to stabilize. In this method, illustrated in Fig. 3.7 current is supplied by two voltage probes, while the other two are measuring the potential drop measured over the sample. The conductivity is then determined as: [32]

$$\sigma = \frac{I}{U}\frac{l}{A} \tag{3.11}$$

where I is the supplied current, U is the voltage drop, l is distance between voltage probes set to 0.5cm and A is the cross section of the sample.

Same bars as for Seebeck measurement were used for electrical conductivity measurements without any additional processing processing prior the measurement.
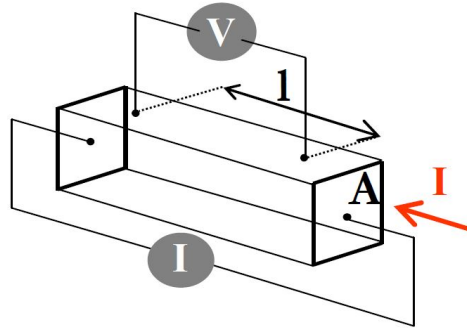

Figure 3.7: Schematic illustration of 4-point probe electrical conductivity measurement. [11]

3.6 Investigated stoichiometries

Four stoichiometires were synthesized: stoichiometric CMO (V0) and CMO with 2.5vol% (V2.5), 5vol% (V5) and 10vol% (V10) of secondary phase. Preliminary work was conducted on stoichiometric $Ca_{0.5}Mn_{0.5}O$, meaning 50/50 ration between CaO-MnO. Further 5vol% powder was used to conduct some preliminary tests on manganese-rich $Ca_{0.5}Mn_{0.5}O$. In the end TE proprieties

only V0, V2.5 and V5 were investigated. Table 3.4 summarized names, stoichiometries and ratios that were investigated.

Table 3.4: Overview over investigated stoichiometries together with their sample IDs

Sample ID	Amount of secondary phase	mol % CaO	mol % MnO
V0	0 - Stoichiometric	50.0	50.0
V2.5	2.5vol%	49.5	50.5
V5	5vol%	49.1	50.9
V10	10vol%	48.2	51.8

Theoretical densities of manganese rich samples were calculated through rule of mixtures:

$$\rho_{tot} = \rho_{CaMnO3}V_{CaMnP3} + \rho_{CaMn2O4}V_{CaMn2O4} \tag{3.12}$$

where ρ_{tot} is the theoretical density of a manganese rich sample and respectively $\rho_{CaMnO3/CaMn2O4}$ $V_{CaMnO3/CaMn2O4}$ is the theoretical density and volume fraction of either $CaMnO_3$ of $CaMn_2O_4$. Calculated values are presented in Table 3.5 All future results and discussion involving density is referring to those densities. Theoretical densities of pure materials can be found in Appendix E

Table 3.5: Overview over calculated theoretical densities for manganese-rich samples.

Sample ID	V2.5	V5	V10
Calculated theoretical density [g/cm3]	4.5825	4.5850	4.5900

Chapter 4

Results

4.1 Synthesis of powder precursor

4.1.1 Synthesis of single phase $Ca_{0.5}Mn_{0.5}O$

Initial planetary milling of raw precursors resulted in a homogeneous mixture of $CaCO_3$ and MnO_2 shown in Fig. 4.1. This caused large agglomerate to form, especially those of MnO_2 were broken up into smaller particles and formed smaller, softer agglomerates. The raw powder mixture had a dark grey colour due to MnO_2.

Samples of all stoichiometries were reduced at same conditions and in all cases single step reaction sintering was needed to obtain pure single phase material. Sintering program was determined during specialization project. Details can be found in Appendinx A. The resulting CaO-MnO solid solution phase was characterized through XRD as $Ca_{0.5}Mn_{0.5}O$, Fig. 4.2. The additional peaks that are not marked belong to tungsten radiation from the instrument. The reduced phase has a strong green colour caused by Mn^{2+}. [18]
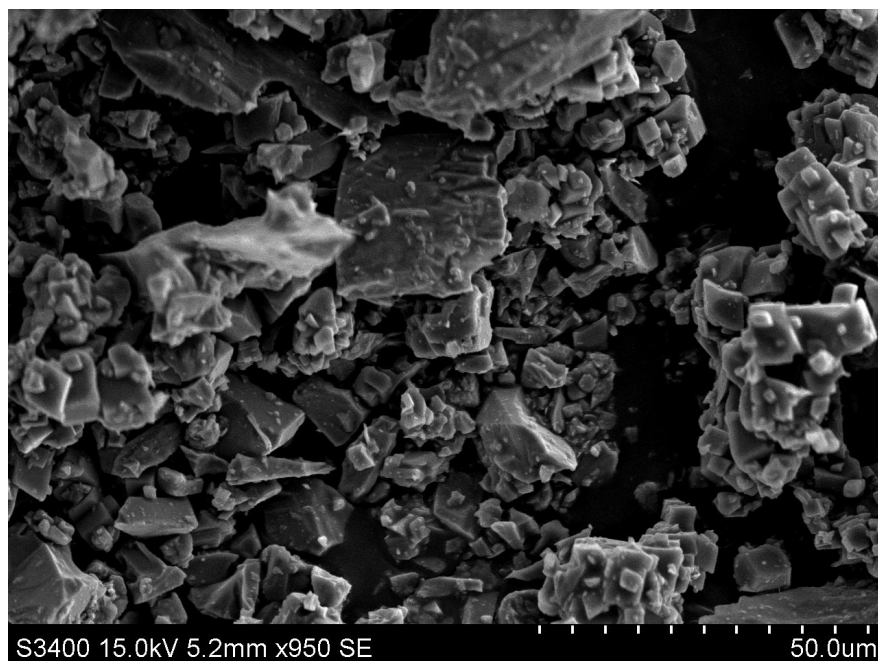
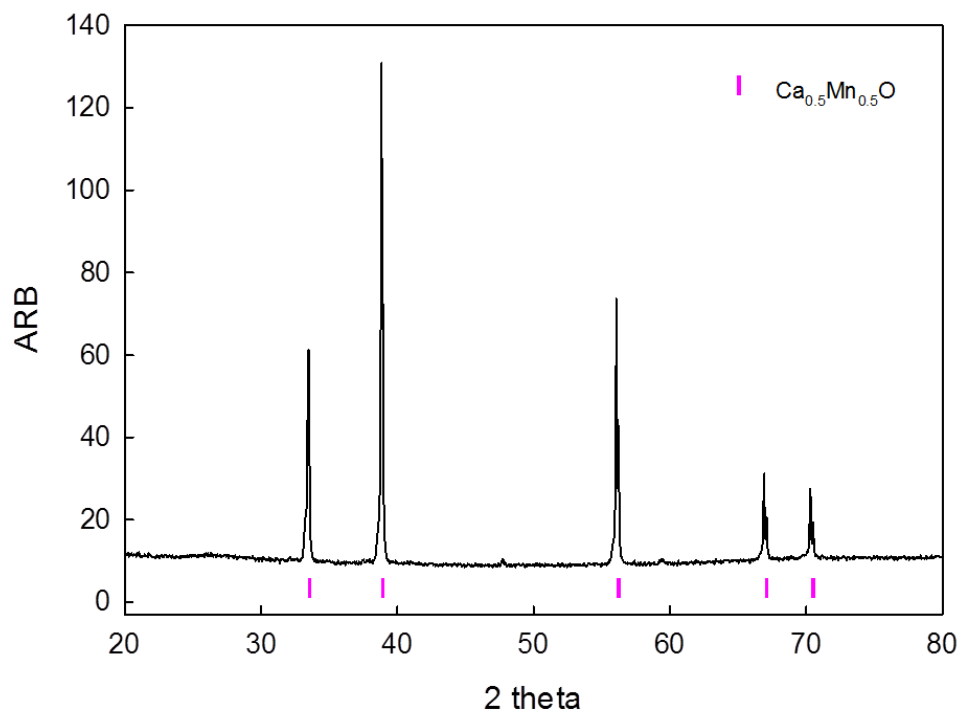Figure 4.1: SEM image of mixed and dried $CaCO_3$ and MnO_2 powders coated with gold for better conductivity.

Figure 4.2: XRD pattern of single, reduced phase, $Ca_{0.5}Mn_{0.5}O$, marked red. Small unmarked peaks are due to tungsten radiation coming from the instrument.

4.1.2 Determination of milling time

To obtain powder precursor, the single phase $Ca_{0.5}Mn_{0.5}O$ pellets were hand ground in a mortar. Obtained powder was then transferred to a milling jar together with 80mL of ethanol and milled in planetary ball mill at 175rpm for the total time of 2h. Same as for mixing 15 $\varnothing$10mm YZT milling balls were used as the milling medium. Each 15min a sample of the powder was taken out of the jar, dried in air and analysed in SEM to estimate the particle size and see its evolution with increasing milling time. Obtained images are shown in Fig. 4.3a and Fig.4.4. The particle morphology remained unchanged up till 1h45min of milling when small platelets are becoming visible. In general particles are uneven in shape and size with mortar crushing resulting in largest particles and first major difference in size decrease is noticeable after 1h of milling. As shown in the figures, obtained the particles tend to agglomerate and form large clusters. Particles ground with mortar are on average 7-10μm in size, those milled for 1h are about 3-5μm while those milled for 2h have a very large particle size distribution between 1 and 8μm. This means that not all powder is thoroughly milled and additional processing will be needed.

An interesting feature was observed in the $Ca_{0.5}Mn_{0.5}O$ microstructure, as shown in Fig. 4.3b. Many of the particles have a step-like structure with steps up to 1μm in width and <1μm in height. The structure is similar to what was observed by Varela [65] and which is caused by the rock-salt crystal structure.
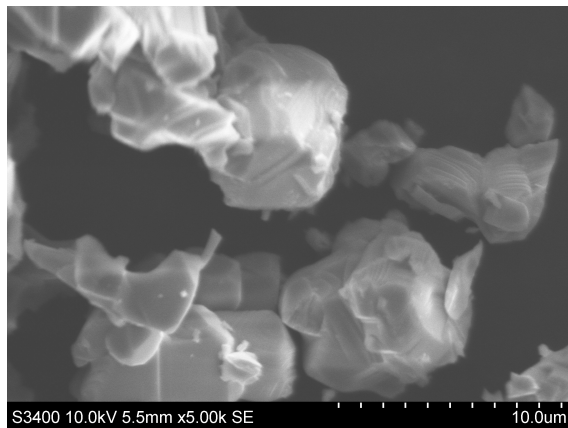
(a) Mortar
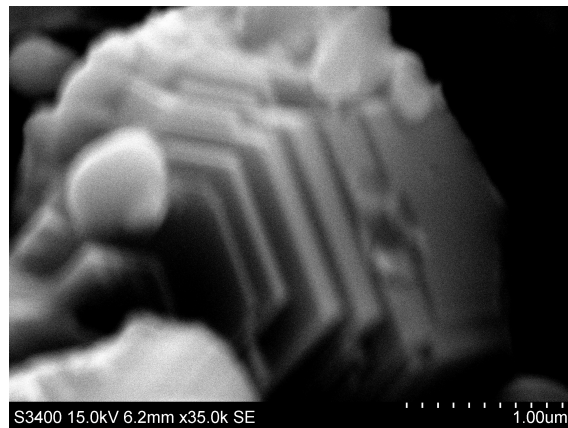
(b) Magnification of particle with a step structure

Figure 4.3: SEM images of single phase $Ca_{0.5}Mn_{0.5}O$ hand ground in a mortar

(a) 15 min

(b) 30 min
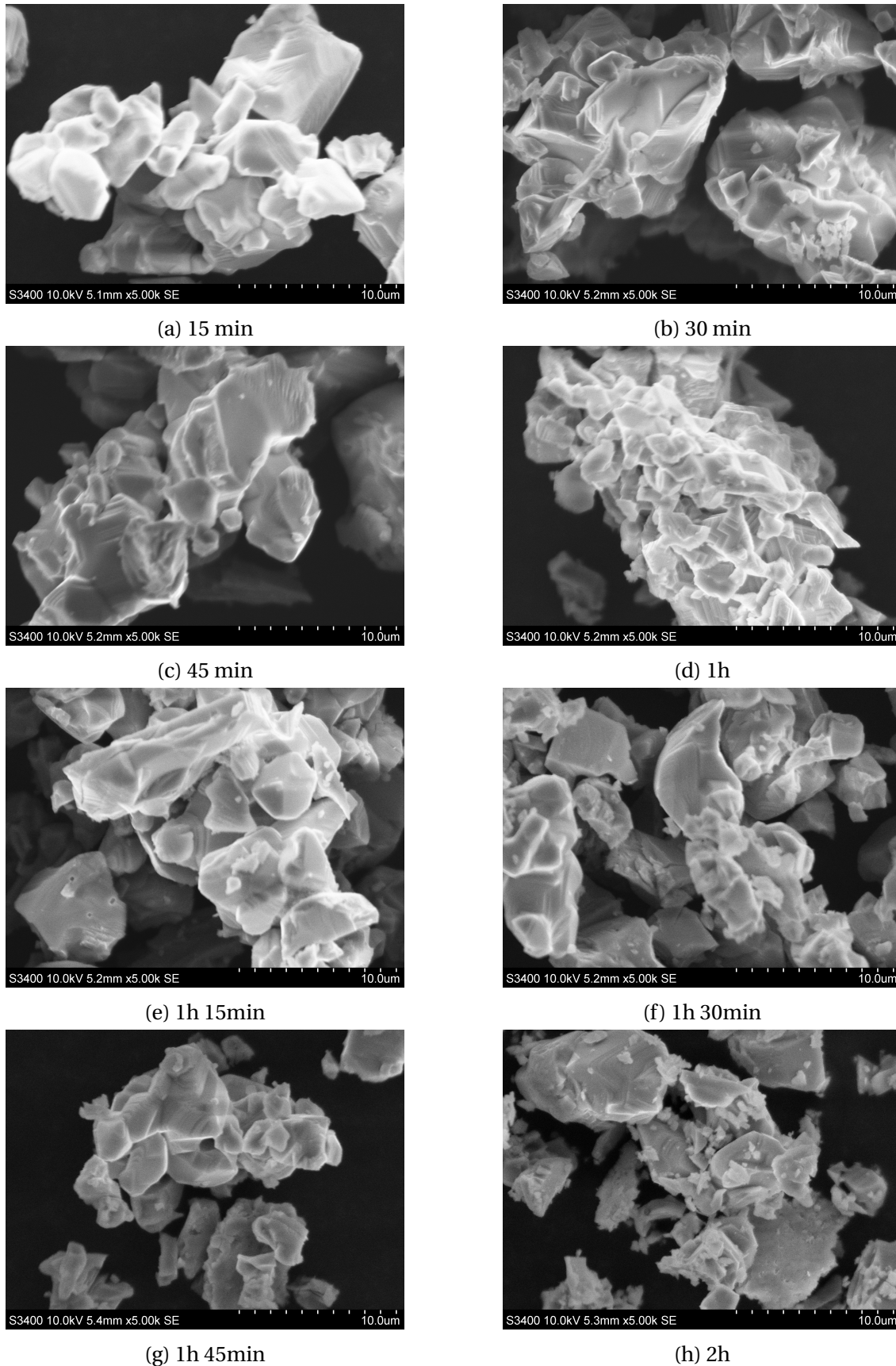
(c) 45 min

(d) 1h

(e) 1h 15min

(f) 1h 30min

(g) 1h 45min

(h) 2h

Figure 4.4: Investigation of particle size reduction - SEM images of single phase $Ca_{0.5}Mn_{0.5}O$ planetary milled at 175rpm with milling times specified in subcaptions.

Based on the SEM results three samples, hand ground in mortar, milled for 1h and 2h, were chosen to be further analysed. A BET measurement was conducted to obtain an estimate on particle size. Table 4.1 shows the measured BET surface as well as the calculated particle size using Eq. 3.7.

Table 4.1: Single phase $Ca_{0.5}Mn_{0.5}O$ particle size based on BET measurement

Milling procedure	A_{BET} [m^2/g]	Particle size [μm]
Mortar	0.6602	2.138
1h milling	1.9198	0.735
2h milling	2.3056	0.427

Further, DIL measurements were conducted to investigate sintering proprieties of the material. The measurement was conducted in 2% H_2 in Ar, with max temperature of 1200°C, dwell time of 1h and the typical heating and cooling rate of 2K/min. Obtained sintering curves are presented in Fig. 4.5. Fluctuations at the beginning of heating step visible up to about 100°C are due to instrument and are not considered in the discussion of the results.

Lastly, the three selected powders were pressed into $\varnothing$10mm pellets on a uniaxial press with 100MPa pressure and sintered in 5% H_2 at 1250°C for 6h. Obtained ceramics were measured with Archimedes method to compare the final densities produced by particle size reduction. Results are shown in Table 4.2.

Table 4.2: Single phase $Ca_{0.5}Mn_{0.5}O$ ceramics after milling and sintering at 1250°C for 6h in 5% H_2.

Milling process	ρ_{bulk} [g/cm^3]	Π_{Open} [%]	Π_{Closed} [%]	ρ_{rel} [%]
Mortar	2.55	38.07	1.90	60.0
1h milling	2.86	31.46	1.35	67.2
2h milling	2.94	29.97	0.86	69.1

For the sake of clarity when presenting further results it should be noted that 1h milling time was chosen as the most suitable one and was included in the synthesis procedure for all future samples. Explanation for this choice can be found in Section 5.1
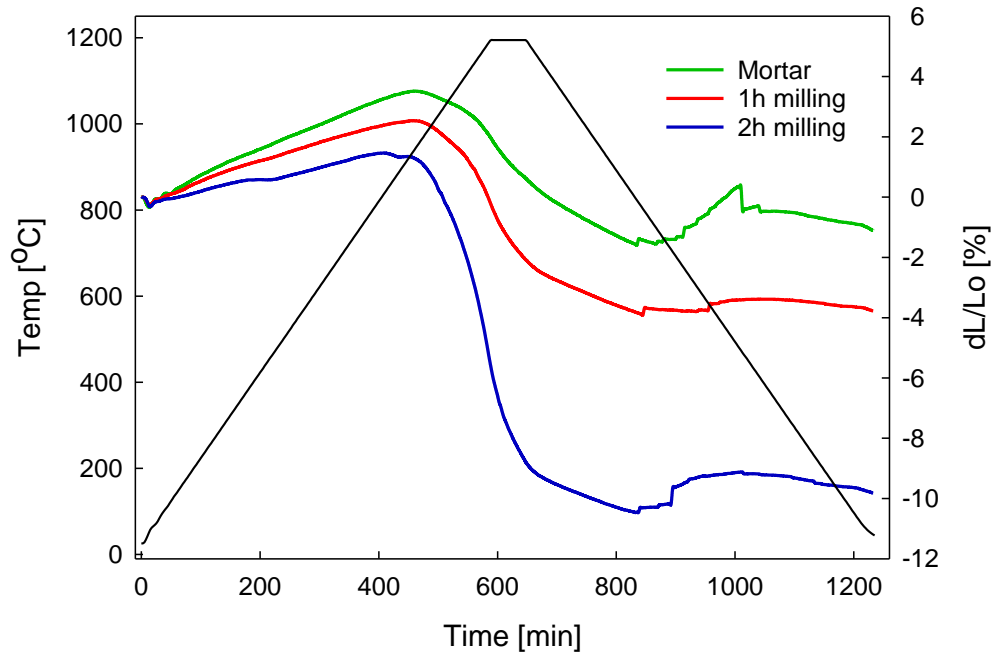
Figure 4.5: Sintering behaviour investigation - DIL measurement of hand ground in a mortar and milled single phase $Ca_{0.5}Mn_{0.5}O$ powders in 2% H_2 atmosphere. Milling was conducted for 1h and 2h at 175rpm with addition of ethanol.

4.1.3 Determination of sintering parameters

Green body density improvement

Since decreasing of initial particle size did not give desired results approx. 90% of the theoretical density, additional densification of green body, in form of sieving and cold isostatic pressing (CIP), was introduced to the synthesis procedure. Sieving through a 75μm sieve (smallest screen size available) removed all unmilled particles above the screen size and formed soft agglomerates. Available CIP uses liquid to apply high, uniform pressure on the sample from all sides. In addition to reducing porosity it also evens out density distribution in the sample and removes any density gradient that could have been caused by the uniaxial press.

Use of CIP caused immediate decrease of sample dimensions in all directions, implying that the green density is improved. Table 4.3 shows density variation with and without use of CIP at 2kbar obtained through Archimedes method and measurement of geometrical dimensions of the pellets. Based on those results it was decided to include CIP in synthesis of all future

samples.

Table 4.3: Investigation of impact of green density of $Ca_{0.5}Mn_{0.5}O$ on ceramic's density. ρ_{green} and ρ_{sint} are geometric densities of the green body and sintered ceramic respectively.

Sample	ρ_{green}[g/cm^3]	ρ_{sint} [g/cm^3]	ρ_{bulk} [g/cm^3]	Π_{Open}[%]	Π_{Closed}[%]	ρ_{rel} [%]
without CIP	1.94	1.96	2.55	38.07	1.90	60.0
with CIP	2.90	3.01	3.14	24.73	1.34	73.9

Heating program adjustment

As a next step to obtain desired density, temperature and atmosphere were adjusted and following things were discovered:

- Temperature above 1250°C results in melting of the sample if no other spacer but coarse powder precursor is placed between the pellet and the alumina boat. As the sample reacts with the alumina a dark green layer is formed on the bottom of the boat.

- Temperature of 1300°C and higher in highly reducing atmosphere (5% H_2 in Ar) with Pt plate spacer between the sample and the alumina leads to firstly reaction between Pt and the sample as well as evaporation of manganese from the sample. This can be observed as change in colour from green to white. This reaction is not very fast though, as only few micrometer are formed during 6h of sintering as shown in Figure 4.6. The bulk of the sample remains as $Ca_{0.5}Mn_{0.5}O$. Deposition of Mn in form of light green coating, can be observed on some parts of the furnace as well as bubbles on the surface of Pt plate.

- Conducting sintering at high temperatures (1300°C or more) in pure N_2 and only maintaining part of the heating and cooling step in reducing atmosphere (850°C threshold for atmosphere switch) results in dense, undamaged samples.

- Use of a coarse powder precursor as bed for the pellet to prevent potential contamination at temperatures higher than 1250°C even with Pt spacer with direct contact with alumina results in melting of the powder precursor.

Summary of the temperature and atmosphere variation can be found in Table 4.4

(a) Top surface
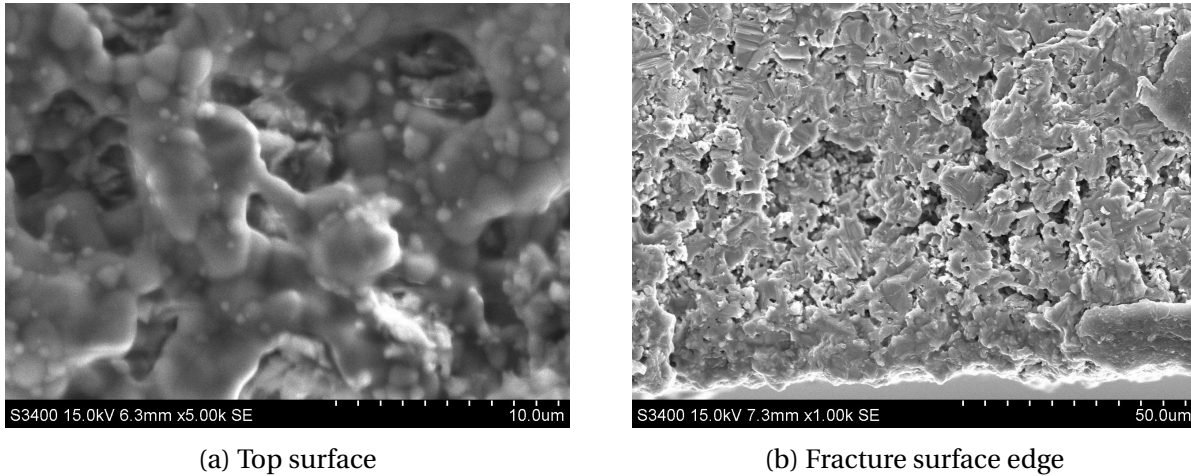

(b) Fracture surface edge

Figure 4.6: SEM images of manganese deficient sintered sample. Sample was coated with gold to improve conductivity.

Table 4.4: Summary of temperature and atmosphere variation as part of density improvement process for pure $Ca_{0.5}Mn_{0.5}O$ with indication whether the sample can be used for further processing.

Temp [°C]	Spacer	Atmosphere	Result	Usable
1250	Powder	5% H_2 in Ar	Low density	Yes
> 1250	Powder	5% H_2 in Ar	Complete melting	No
> 1250	Pt + powder	5% H_2 in Ar	Melting of the powder	No
≥ 1300	Pt	5% H_2 in Ar	Evaporation of Mn	No
≥ 1300	Pt	5% H_2 in Ar +N_2	Dense sample	Yes

Lastly, the impact of dwell time on the density was investigated. In total four samples were sintered. Used programs as well as results are presented in Table 4.5 and Fig. 4.7. Microstructure of fracture surface of obtained dense ceramics was investigated with SEM and images can be found in Fig. 4.8.

It was observed that density increases with increasing dwell time and temperature. The impact of increased dwell time was smaller than that of increased temperature. In case of lower densities (<80%) fracture propagated through the grain boundaries, however at high densities fracture went through the grains.

In the end the last program, i.e. max. temp. of 1350°C with dwell time of 12h and combination of 5% H_2 in Ar + N_2 was chosen as the most suitable sintering program and it was used for all future samples.

Table 4.5: Overview over densities of pure $Ca_{0.5}Mn_{0.5}O$ obtained form selected sintering programs

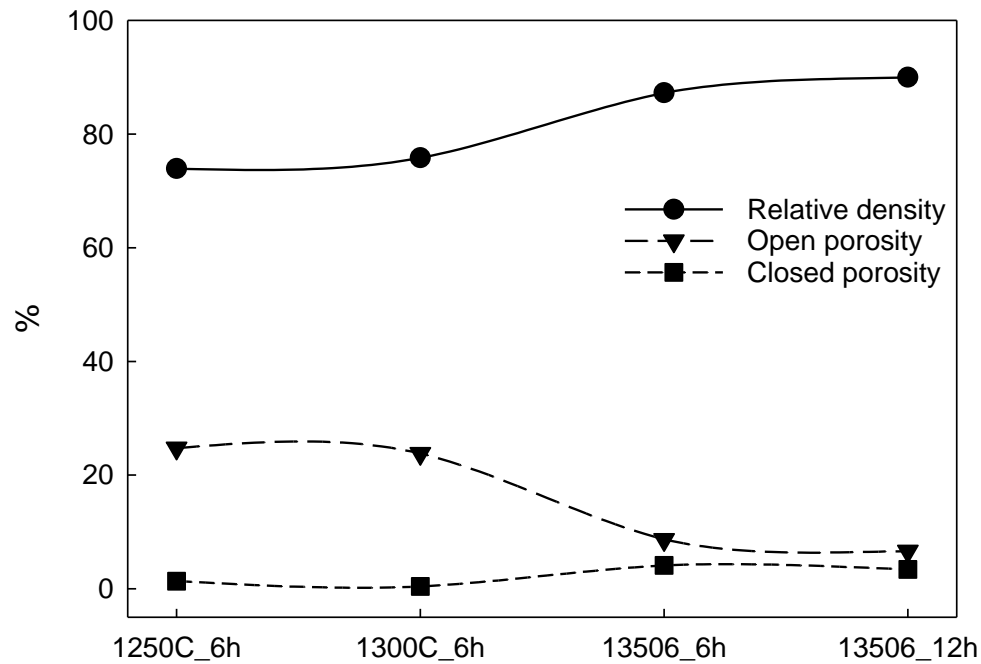| T [°C]	Dwell [h]	Atmosphere	ρ_{bulk} [g/cm^3]	Π_{Open}[%]	Π_{Closed}[%]	ρ_{rel} [%]
1250	6	5% H_2	3.14	24.73	1.34	73.9
1300	10	5% H_2 + N_2	3.22	23.78	0.40	75.8
1350	6	5% H_2 + N_2	3.71	8.65	4.10	87.3
1350	12	5% H_2 + N_2	3.82	6.61	3.40	90.0

Figure 4.7: Overview over densities and porosities for single phase $Ca_{0.5}Mn_{0.5}O$ obtained with selected sintering programs. Labels on x-axis denote sintering temperature and dwell time that resulted in given relative density and porosity, y-axis.
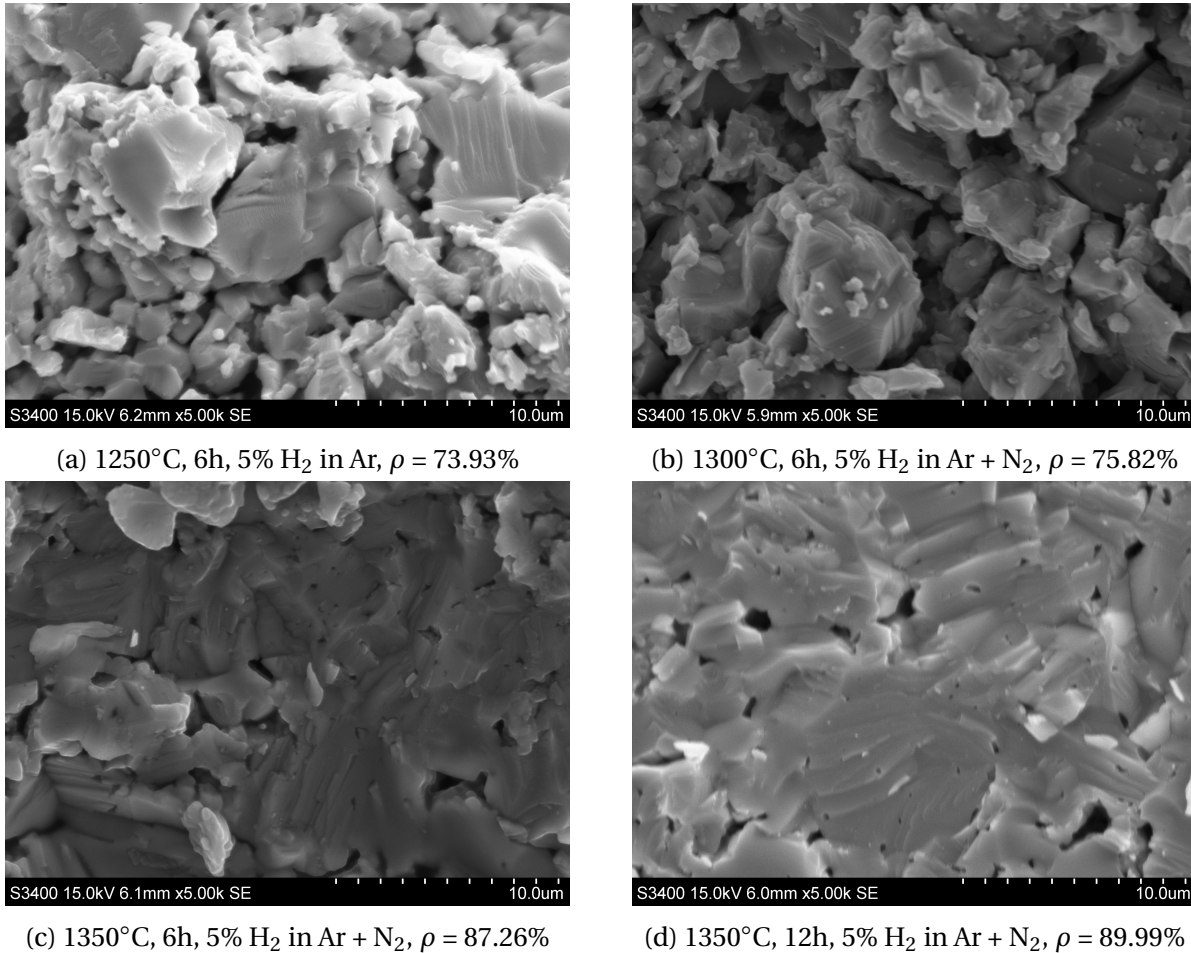
(a) 1250°C, 6h, 5% H_2 in Ar, ρ = 73.93%

(b) 1300°C, 6h, 5% H_2 in Ar + N_2, ρ = 75.82%

(c) 1350°C, 6h, 5% H_2 in Ar + N_2, ρ = 87.26%

(d) 1350°C, 12h, 5% H_2 in Ar + N_2, ρ = 89.99%

Figure 4.8: Investigation of temperature influence - SEM images of fracture surface of pure $Ca_{0.5}Mn_{0.5}O$ sintered at various temperatures and times

4.2 Determination of annealing program

TGA and DIL measurements were conducted to investigate oxidation proprieties of $Ca_{0.5}Mn_{0.5}O$. 950°C was chosen as a max. temperature knowing that this temperature ensures relatively fast reaction kinetics and also in the case of the manganese rich samples, the secondary phase starts to form at around 900°C. In case of TGA precursor powder was used in the measurement while for DIL analysis, 5mm single phase $Ca_{0.5}Mn_{0.5}O$ pellets were sintered at previously established conditions, resulting in dense ceramics. In both cases 2K/min heating and cooling rate was used.

4.2.1 Stoichiometric powder precursor

TG analysis of stoichiometric CMO (V0), Fig. 4.9, shows typical perovskite behaviour. Oxidation begins at about 350°C and proceeds in one step till it reaches equilibrium at max temperature. At that point $Ca_{0.5}Mn_{0.5}O$ is converted to $CaMnO_{3-\delta}$ which picks up additional oxygen upon cooling. Similar CMO behaviour was shown by Thiel [63] with mass loss upon heating and mass increase upon cooling.
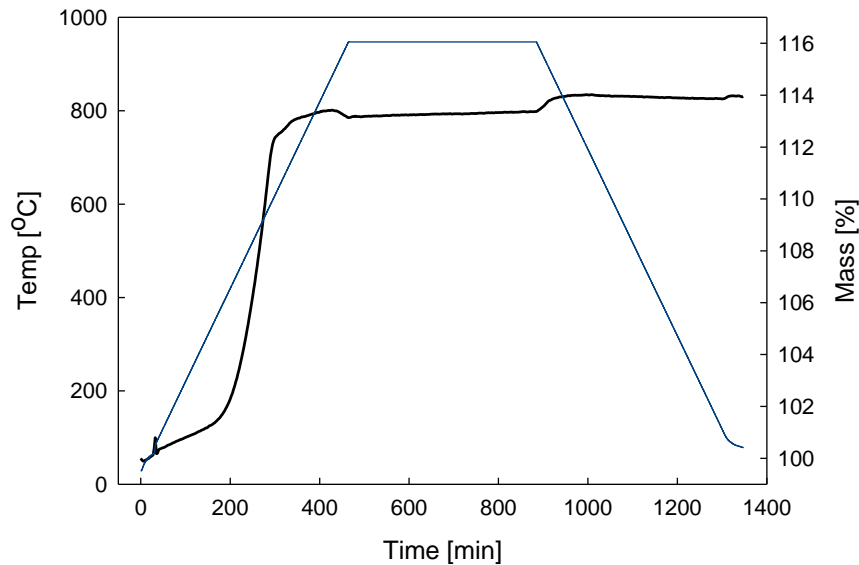

Figure 4.9: TG analysis of stoichiometric (V0) precursor powder in air. Max temp = 950°C, dwell = 7h

DIL analysis of V0, Fig. 4.10, shows rapid expansion that starts at about 500°C and ends in fracture of the sample at maximum temperature of 950°. Inverstigation of sample after the measurement showed it complete disintegration. This affected the data collected upon cooling as the change in dimensions between reduced and annealed sample corresponds well with the expansion data collected until the end of dwell time but nod during the cooling.
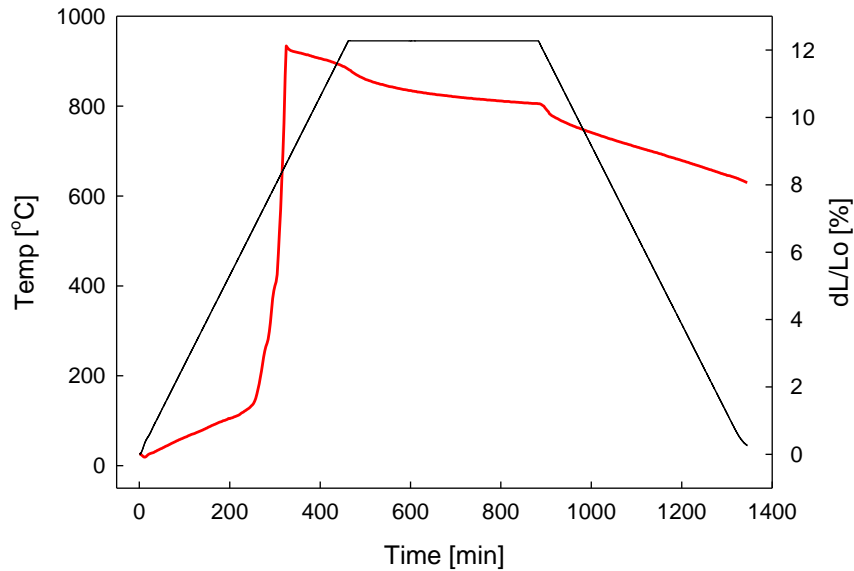
Figure 4.10: DIL analysis in air of stoichiometric (V0) pure rock-salt dense pellet. Max temp = 950°C, dwell = 7h.

4.2.2 Manganese-rich precursor powder

TG analysis of manganese rich samples (V5 and V10), Fig. 4.11, shows some trends similar to perovskite behaviour described in previous section. Oxidation of the material begins at about 500°C and proceeds in one step till maximum temperature temperature. Following mass increase takes place at much slower rate what could be associated with introduction of secondary phase. The transitions that are occurring in the material are also responsible for the mass decrease upon cooling. Over all the mass increase is higher for higher volumes of secondary phase.

DIL analysis of V5, Fig, 4.12, indicates that oxidation for manganese rich samples starts at about 500°C. It is a two step expansion with an intermediate step at about 570°C followed by cracking at nearly 950°C. Same as for V0 sample, pellet has completly disintegrated what affected the data collected upon cooling.
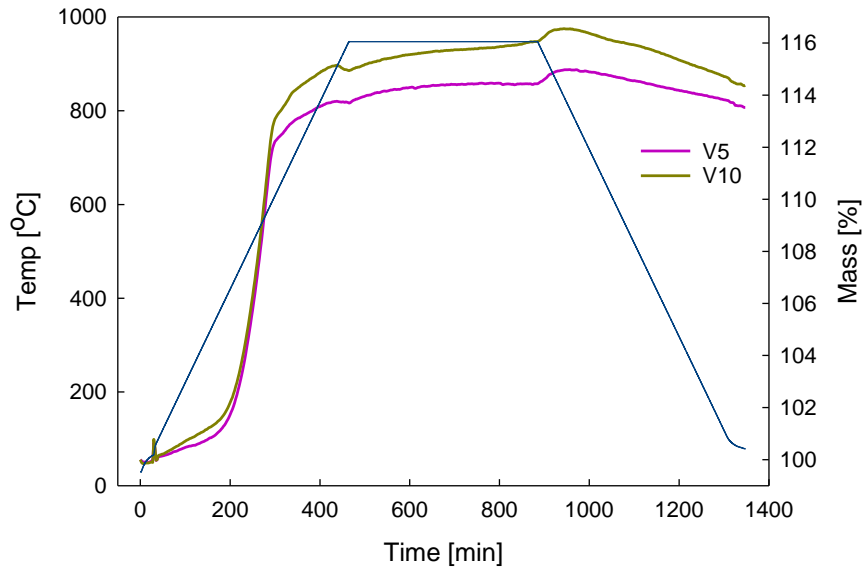
Figure 4.11: TG analysis of manganese rich (V5 and V10) precursor powder in air. Max temp = 950°C, dwell = 7h.
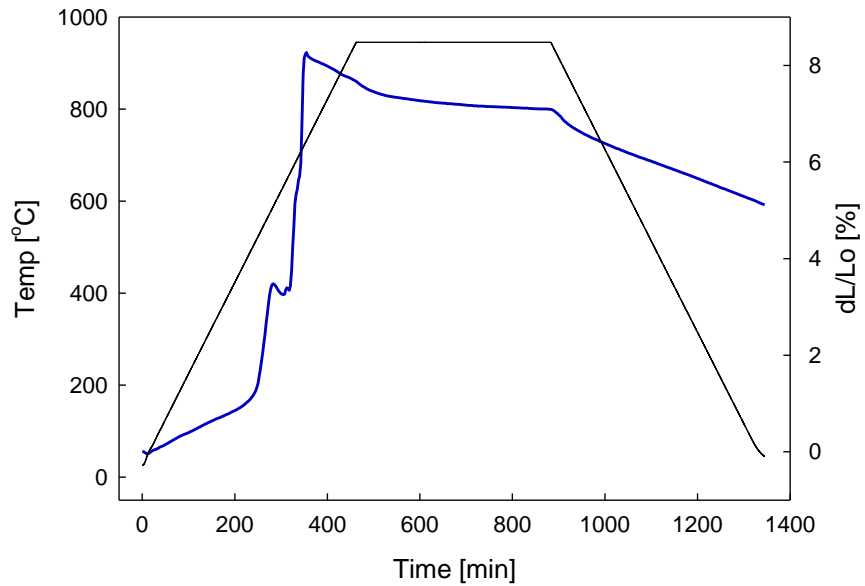

Figure 4.12: DIL analysis in air of manganese rich (V5) pure rock-salt dense pellet. Max temp = 950°C, dwell = 7h.

4.2.3 Correlation between the density of single phase $Ca_{0.5}Mn_{0.5}O$ and annealing temperature

Based on TGA and DIL results, several stoichiometric and manganese-rich samples of different densities were sintered and subjected to different annealing programs in the furnace. Temperature and atmosphere were varied and following correlations were observed for bot stoichiometric and manganese rich samples:

- Low density samples ($\rho_{rel} \leq 75\%$) can be annealed at low temperatures ($\leq 1000°$C) without cracking.

- Medium density samples ($\rho_{rel} < 85\%$) can be annealed at temperatures up to 950°C without cracking.

- To avoid cracking in high density samples ($\rho_{rel} \geq 85\%$) sample has to be annealed at 1250°C.

- Only low density samples can be annealed only in air without cracking. Remaining samples require heating up in reducing atmosphere, followed by flushing of the furnace with inert atmosphere before synthetic air is introduced and kept till the end of the program.

- Annealing of at high temperatures leads to higher densification of samples.

- High density samples are more prone to higher densification upon annealing than low density samples.

- The higher annealing temperature the higher effect on microstructure of the material

4.2.4 Summary

TGA results   In case of TGA measurement all powders exhibit similar behaviour upon oxidation in spite of different Ca/Mn ratios. Oxidation starts are relatively low temperatures, $\approx 400°$C, slowing down around 700°C and once again picking up more oxygen upon cooling. In all cases necking between particles can be observed through formation of lightly bonded kind of a pellet on the bottom of the crucible. This suggests that in addition to oxidation of the powders,

sintering is occurring at the same time. Nevertheless, there are some differences between stoichiometric and manganese rich samples, which will be further investigated in Section 5.2

DIL results   When it comes to DIL measurement the situation is more complicated. The initial stage up to $\approx 600°$C is similar, with initial expansion starting at about $500°$C. Stoichiometric sample expands in one step while the manganese-rich one has an intermediate step. In both cases cracking occurs at high temperatures and affects the measurement during dwell and cooling step. As a result the lowest possible temperature for oxidation of $Ca_{0.5}Mn_{0.5}O$ was determined. Also it was established that annealing only in air is not possible and some additional treatment will be required to prevent cracking.

As a result, high temperature annealing at $1250°$C was chosen as the ideal temperature. Dwell of 3h was chosen since it was shown in TG and DIL that the reaction occurs relatively fast and material obtains the desired phase shortly after reaching max temperature. The microstructure of fully oxidized samples was investigated with SEM, Fig. 4.13. For both stoichiometries it is nearly identical with small relatively spherical pores and cross-grain fracture. Table 4.6 has an overview over relative densities of samples of investigated stochiometries before and after annealing.

Table 4.6: Average relative densities of sintered and annealed samples with different stoichiometries.

Sample ID	V0	V2.5	V5	V10
Sintered [%]	87.4	93.5	89.9	91.5
Annealed [%]	89.8	94.9	93.2	92.6

(a) V0, $\rho = 94.3\%$

(b) V5, $\rho = 91.7\%$

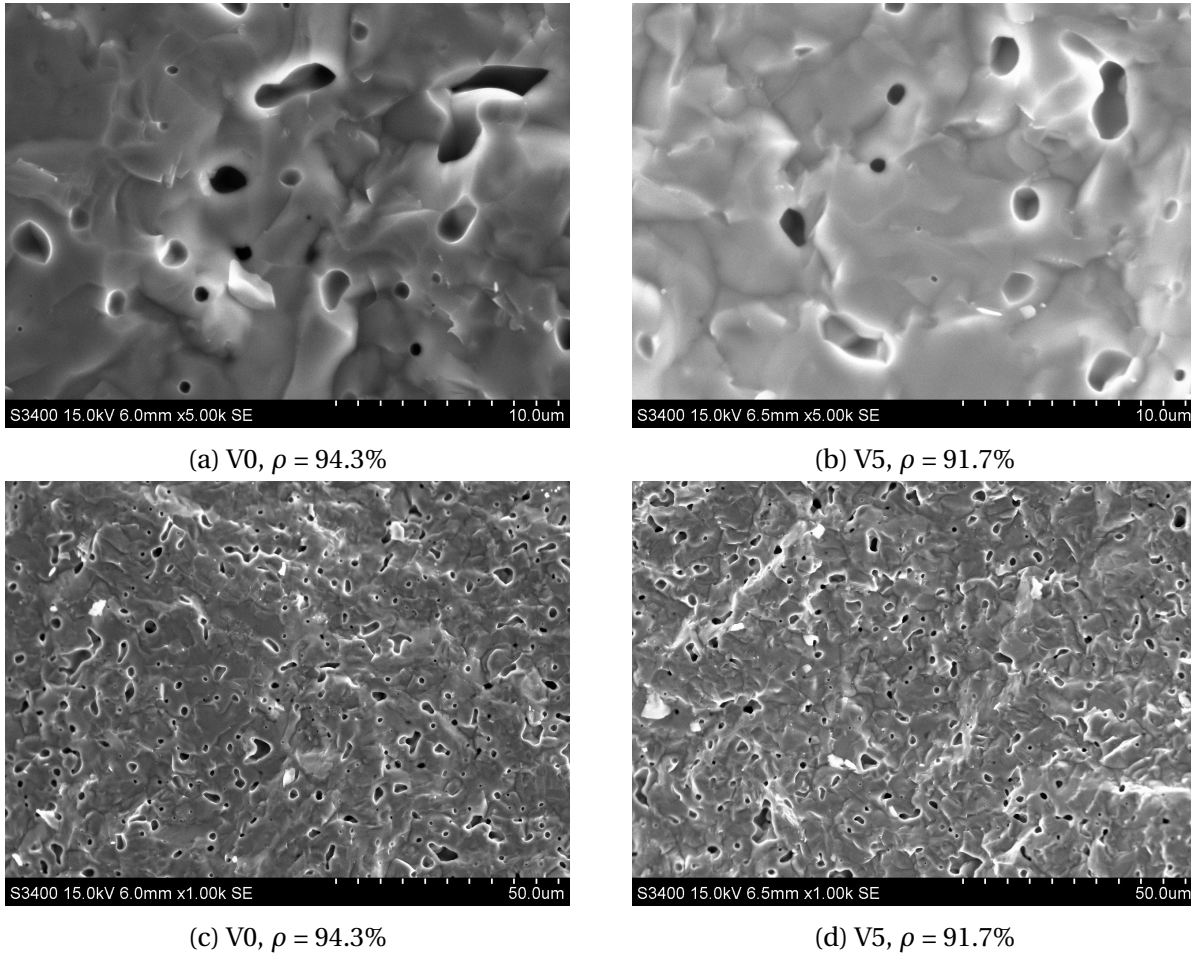(c) V0, $\rho = 94.3\%$

(d) V5, $\rho = 91.7\%$

Figure 4.13: Fracture surface of dense V0 and V5 fully oxidized samples at 1250°C for 3h

4.3   Secondary phases

4.3.1   Reference material

Samples of dense fully oxidized V0 were prepared as a reference material for the manganese-rich samples and subjected to the same treatment and same phase purity characterization. Samples were polished and subjected to thermal etching prior SEM investigations. BSE and SE images of just polished samples can be found in B. SE and BSE images, Fig. 4.14 are showing nearly phase pure material. Small round particles are visible some areas of the sample. Point analysis with EDS, Fig. 4.15 shows that they are rich in Zr and Al impurities that have come from milling jar. Those impurities have not been detected by EDS mapping, Fig. 4.16, analysis or XRD analysis which suggests that their concentration is very low.
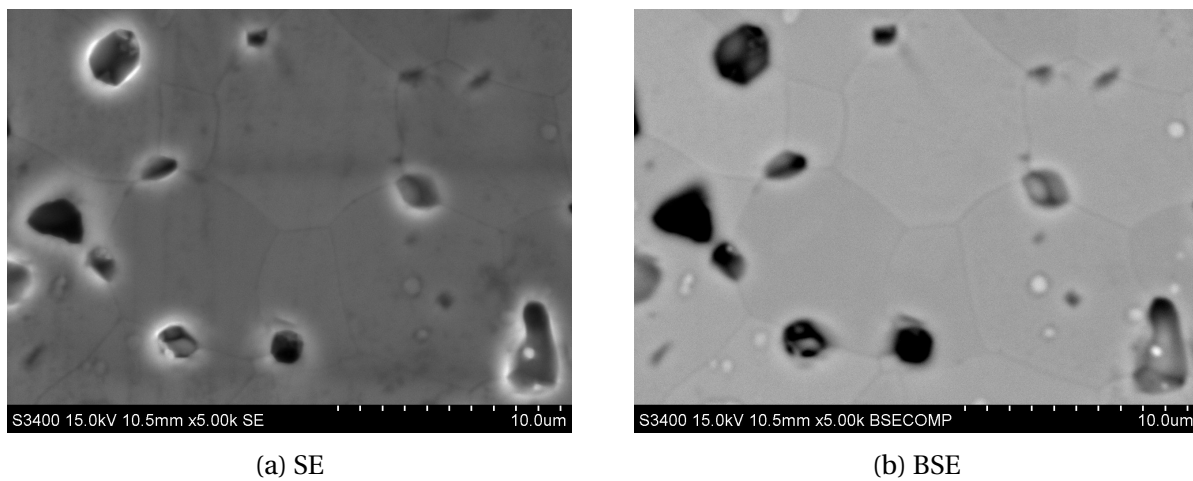
(a) SE

(b) BSE

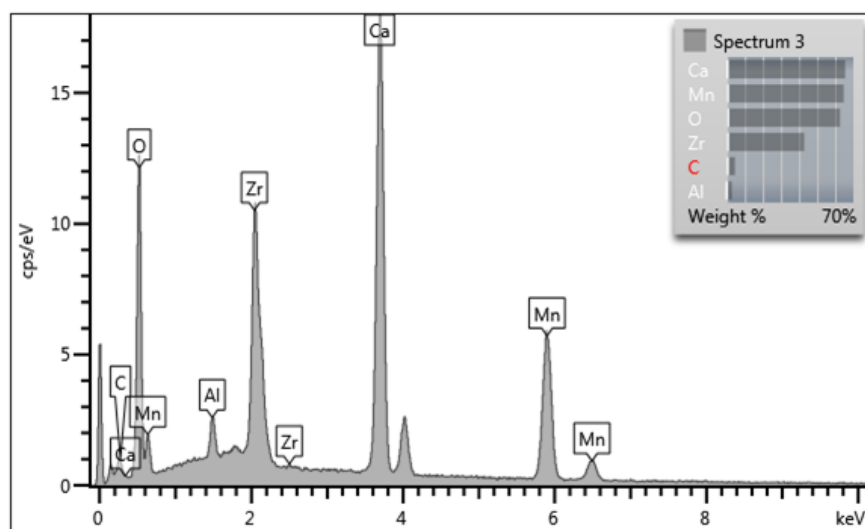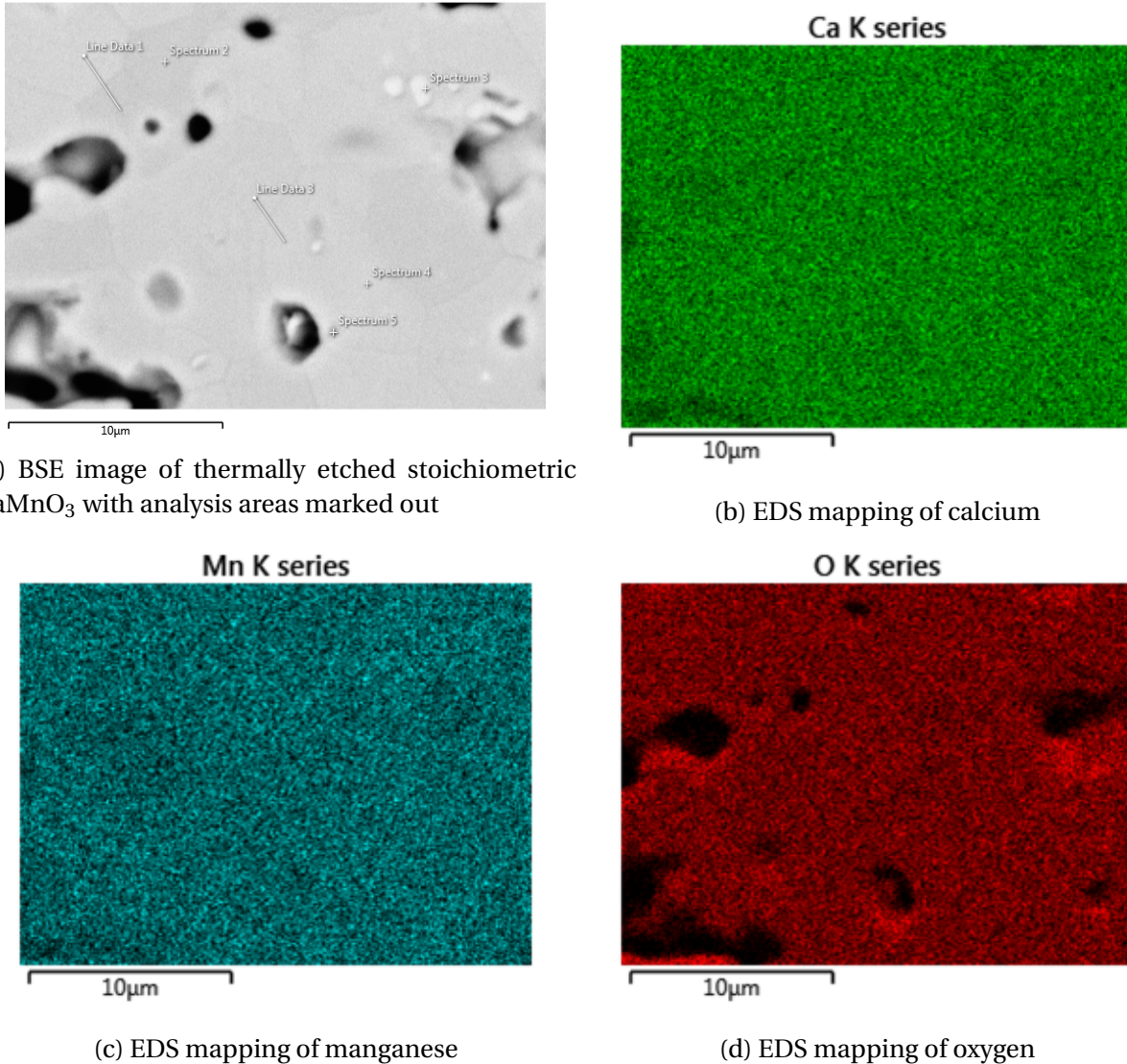Figure 4.14: SEM images of dense V0 annealed at 1250°C for 3h and thermally etched at 1000°C in air.

Figure 4.15: EDS Point scan (Spectrum 3) of white round particles observed in BSE image of V0

(a) BSE image of thermally etched stoichiometric CaMnO$_3$ with analysis areas marked out

(b) EDS mapping of calcium

(c) EDS mapping of manganese

(d) EDS mapping of oxygen

Figure 4.16: EDS mapping of stoichiometric CaMnO$_3$ annealed at 1250°C and thermally etched at 1000°C

4.3.2 CaMnO$_3$ + Ca$_{0.5}$Mn$_{0.5}$O

Based on TG, Fig. 4.9 and DIL measurements, Fig. 4.10 several low annealing temperatures were chosen to investigate the possibility of having a dual-phase material consisting of the rock-salt phase, Ca$_{0.5}$Mn$_{0.5}$O, and perovskite phase, CaMnO$_2$. All oxidations were conducted on low density samples and it was observed that samples annealed at temperatures below 500°C, did not react at all while oxidations at 650°C result in nearly full oxidation and formation of the orthorhombic perovskite with potentially slightly lower oxygen content visible as formation of CaMnO$_{2.8}$, Fig. 4.17. Microstructure, shown in Fig. 4.18, as well as the particles are very un-

even. The typical steps, found in the rock-salt phase remain visible after oxidation and no major densification can be observed.
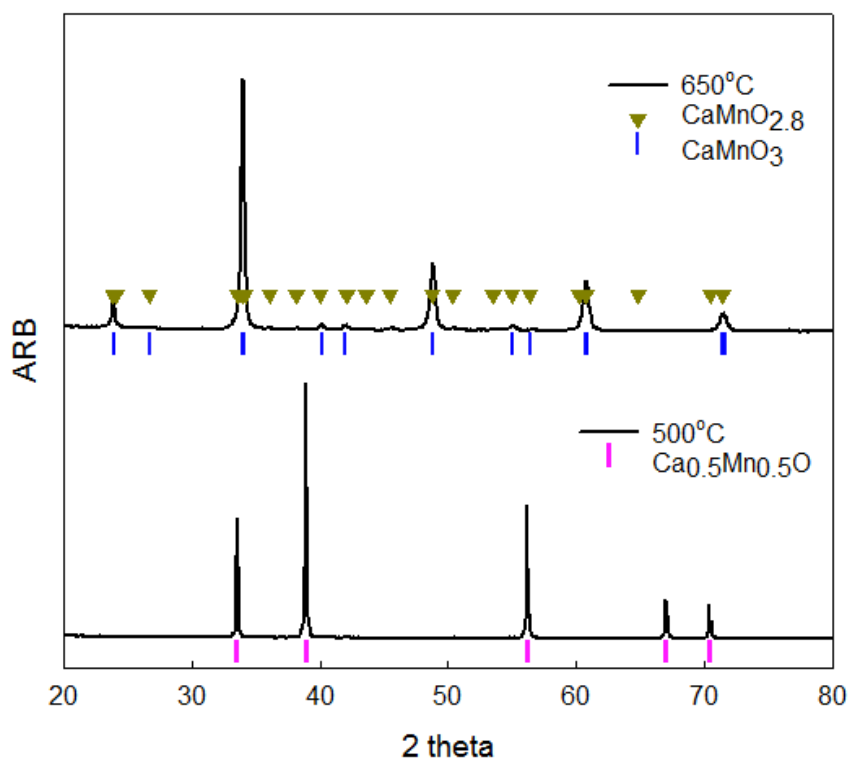

Figure 4.17: Comparison of composition obtained through annealing of low density V0 at low temperatures.

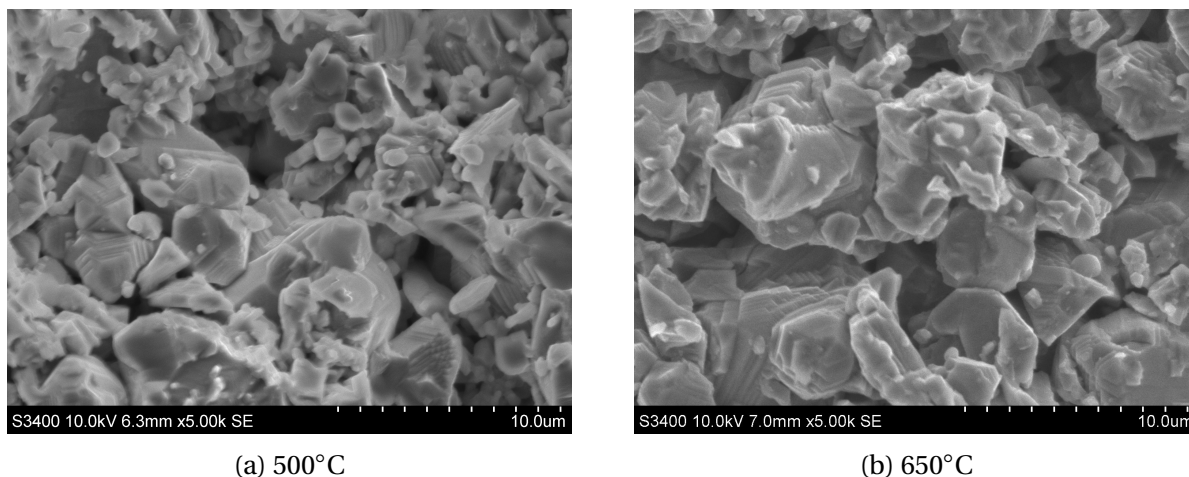(a) 500°C   (b) 650°C

Figure 4.18: Comparison of microstructures obtained from low temperature annealing of low density V0. SEM images taken of fracture surface.

Those results have shown that it is impossible to obtain a mix between the rock-salt and

perovskite structure since the reaction happens so fast due to the topotactic reaction mechanism described in Section 2.5.2. This conclusion is supported by the results obtained from DIL measurements conducted in pure N_2. Due to a leakage of air into the furnace chamber a partial oxidation of measured samples occurred. This resulted in formation of shrinking core shown in Fig.4.19.

(a) Image taken with a camera
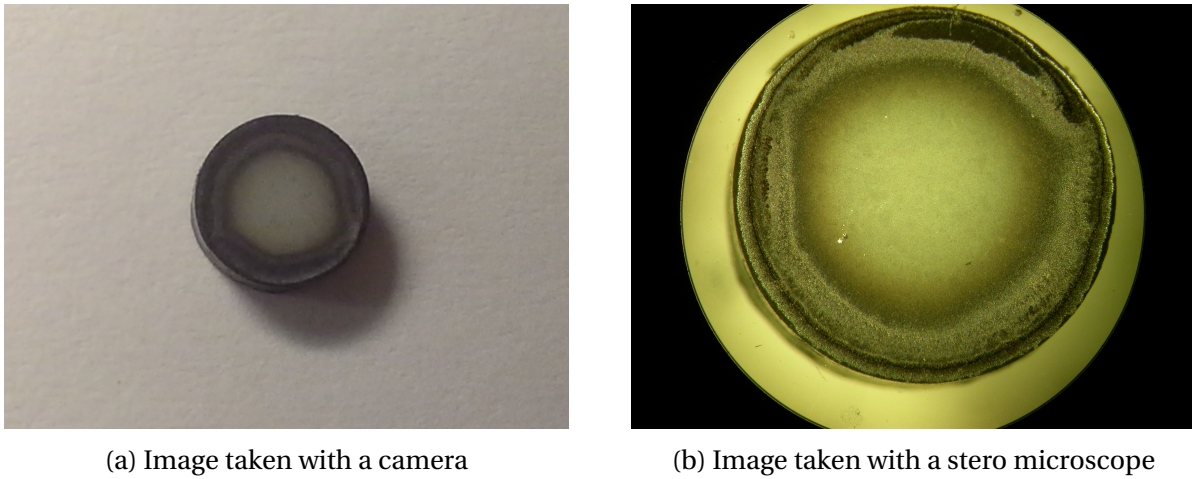

(b) Image taken with a stero microscope

Figure 4.19: Untreated surface of partially oxidized $Ca_{0.5}Mn_{0.5}O$ after DIL measurement in N_2
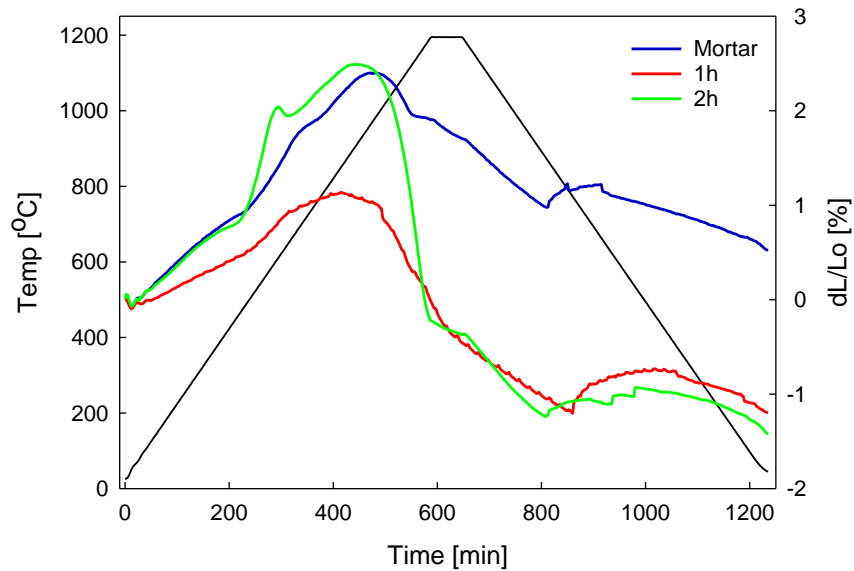

Figure 4.20: DIL measurement in N_2 of single-phase $Ca_{0.5}Mn_{0.5}O$ powders ground in mortar and milled at 175rpm for 1h and 2h.

Polished surface of the pellet was analysed with XRD to determine composition of the differ-

ent layers. As a result of this partial oxidation several phases can be observed in the XRD pattern in Fig. 4.21. Those multiple phases are responsible for the multiple expansion and shrinkage steps visible in the sintering curves obtained from DIL in N_2, Fig. 4.20.
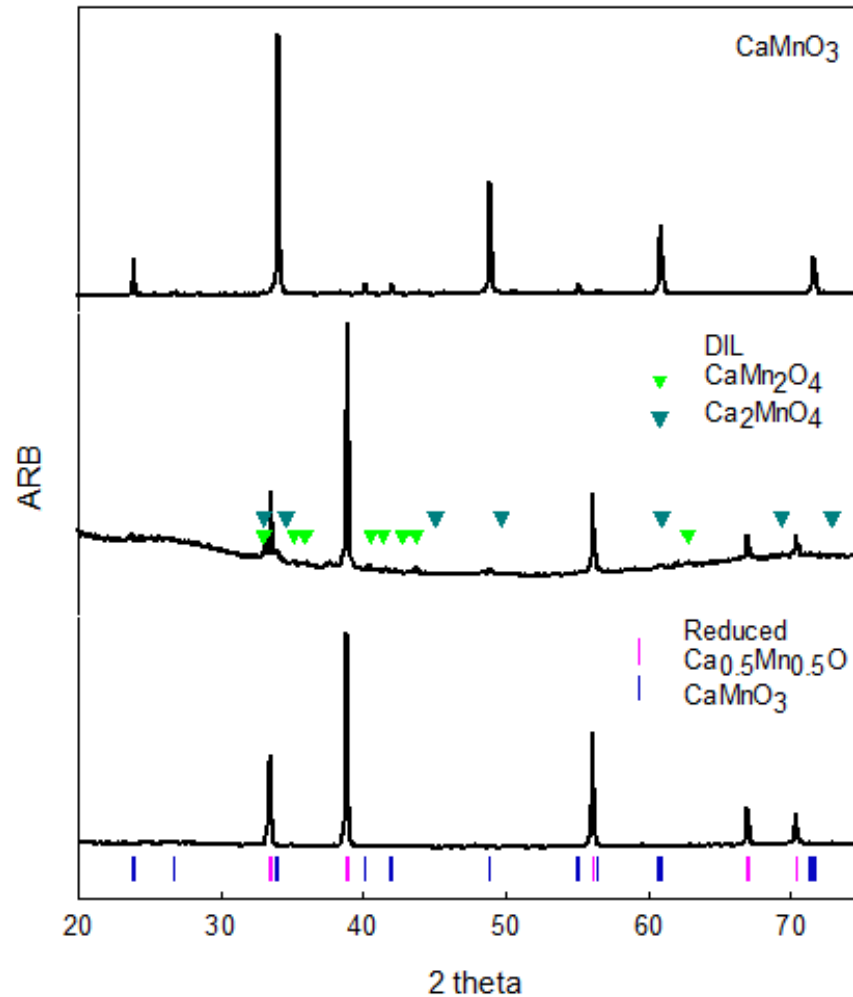

Figure 4.21: XRD pattern of polished top surface of 5mm partially pellet after DIL measurement in N_2.

Further investigation of the interphase of shrinking core was done with metallographic microscope, Fig 4.22 which illustrates how oxidation proceeds from the outside and into the grain. For this investigation, sample was deposited in epoxy and polished <1μm prior investigation.
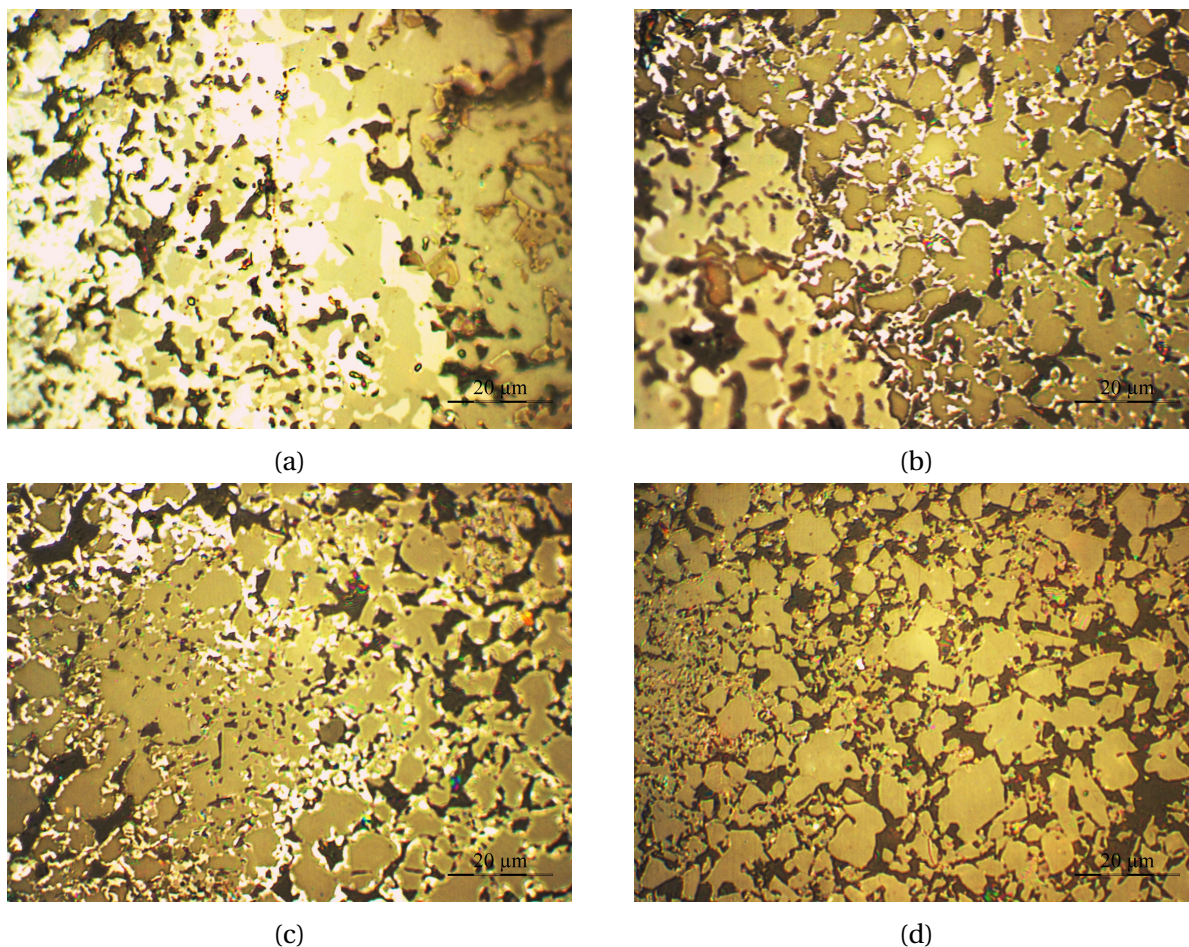
Figure 4.22: Images of V0 after DIL measurement in pure N_2 showing the shrinking core taken with a metallographic microscope. The images are progressing from the edge, ie. fully oxidized $CaMnO_3$ (a) to the core of the sample, i.e. fully reduced $Ca_{0.5}Mn_{0.5}O$(d)

4.3.3 $CaMnO_3$ + $CaMn_2O_4$

Secondary phase formation   From data obtained through DIL, Fig. 4.12, we see that there is an additional step compared to oxidation of the stoichiometric CMO. To further investigate this expansion, series of annealing steps were conducted in pure air. A set of samples was annealed at chosen temperatures with no dwell time to determine what king of phases are responsible for the expansion. Samples were then crushed and phase composition was investigated with XRD, Fig.4.23.
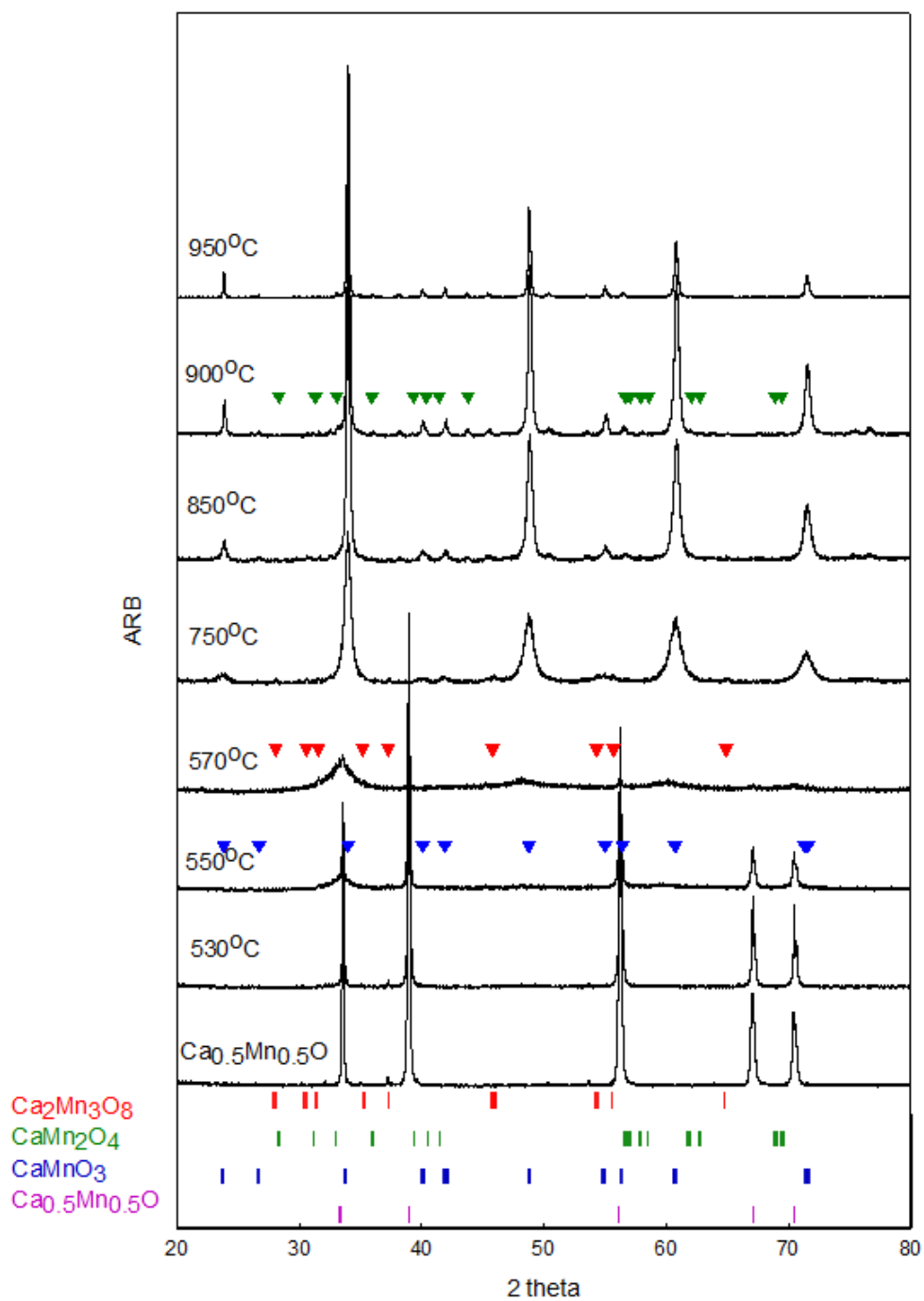
Figure 4.23: Secondary phase evolution in a manganese rich sample (V5). Triangles indicate where given phase can be detected for the first times. Annealing was conducted entirely in air with no dwell time and a heating/cooling rate of 200°C/h. Small peaks in $Ca_{0.5}Mn_{0.5}O$ patterns are due to tungsten radiation.

As a result it was determined that a two-phase material consisting of only $CaMnO_3$ and $CaMn_2O_4$ can be obtained at temperatures as low as 900°C. Lower temperatures result in formation of $Ca_2Mn_3O_8$ and an oxygen deficient perovskite, which agrees well with the phase diagram, Fig. 2.14. Lowest annealing temperatures lead to oxidation of Mn-ions to 3+ resulting in black colour of the sample and shift in cell parameters, however no conversion to perovskite occurs, during this short oxidation time. Later phases are relatively amorphous that are mid phase transition from rock-salt structure to perovskite and the 2:3 phase. As temperature increases, the perovskite phase becomes more evident and the 2:3 phase is being transformed into the desired marokite. Those phase transitions are more evident in Fig. 4.24 which focuses on main peaks and indicates temperature ranges where each phase is present (vertical lines) In case of formation of new phases, peaks at lowest temperatures are often barely visible due to either small amount of the secondary phase being present in the material at that time or by being a part of a larger more amorphous peak. Small peaks observed in difractograms for $Ca_{0.5}Mn_{0.5}O$ and low temperature annealing (530°C and 550°C) are due to tungsten radiation from the instrument and they are not an indication of the 2:3 phase.

Comparison of XRD patterns from samples with various amounts of secondary phase, Fig. 4.25 shows increase in intensity of main peaks corresponding to marokite. In neither of the cases the 2:3 phase have been observed suggesting that it has been completely transformed to marokite.
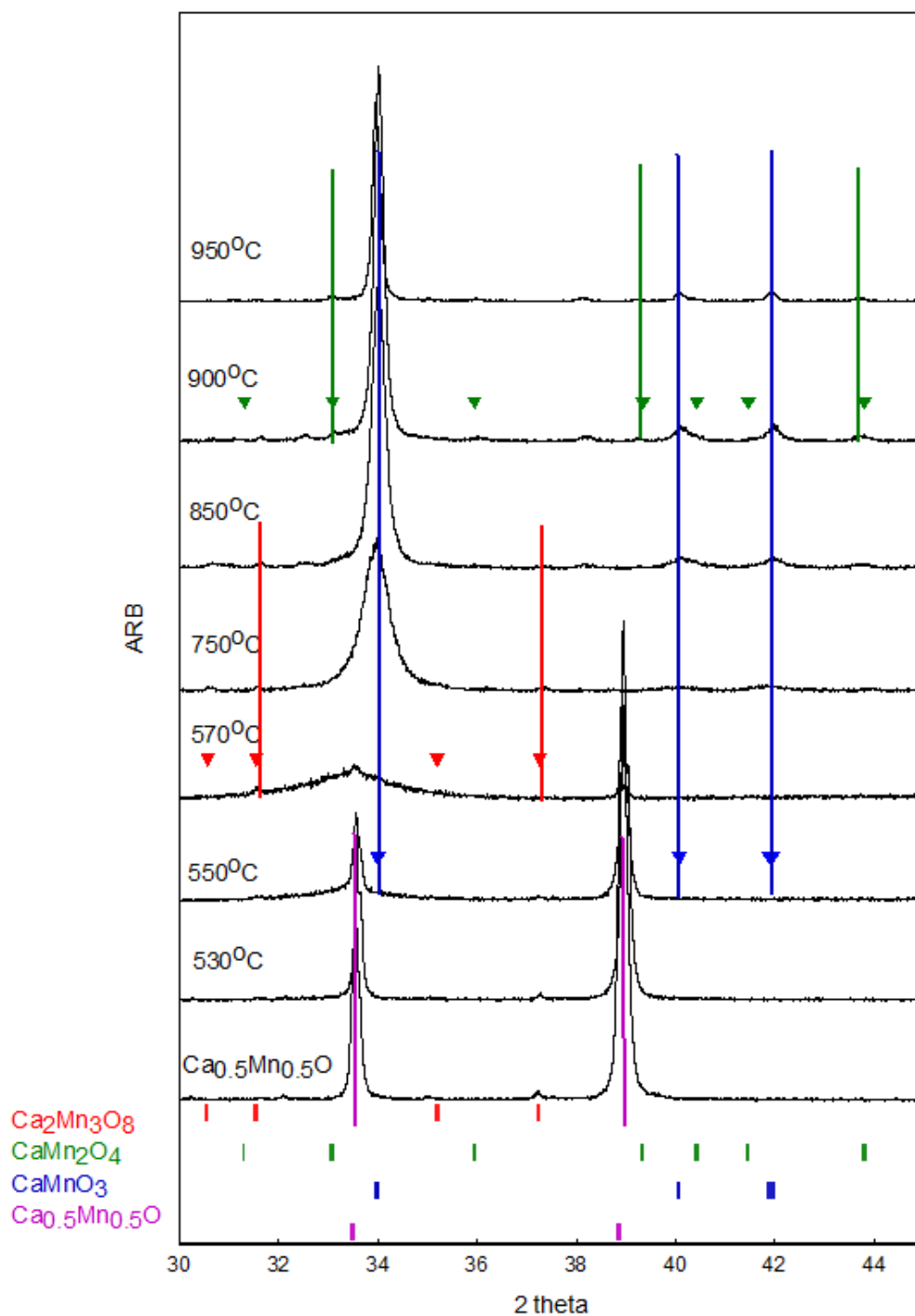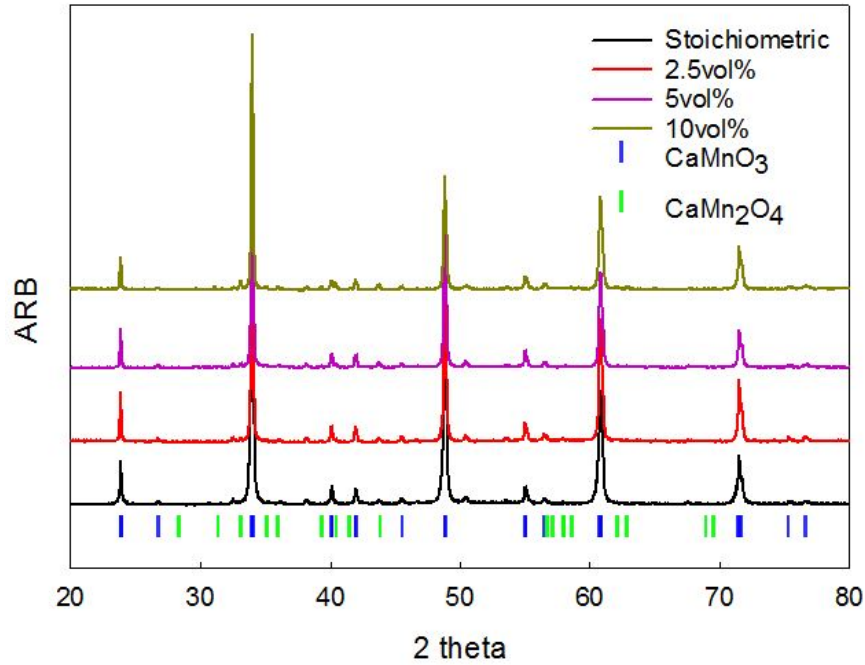
Figure 4.24: Secondary phase evolution in V5 with focus on 30-45 2θ. Triangles indicate start of formation of given phase while lines indicate temperature range where it can be observed. Annealing was conducted entirely in air with no dwell time and a heating/cooling rate of 200°C/h. Small peaks in $Ca_{0.5}Mn_{0.5}O$ patterns are due to tungsten radiation.

(a) Comparison of complete XRD patterns of synthetized stochiometries
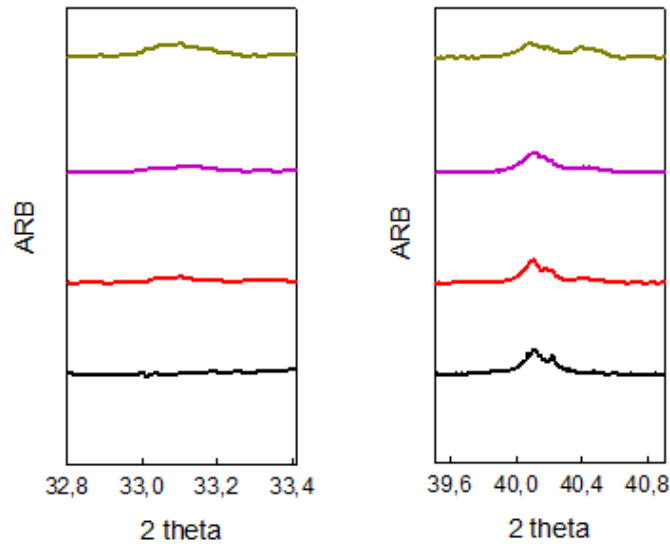
(b) Magnification of $CaMn_2O_4$ (c) Magnification of $CaMn_2O_4$ peak at 33.1° illustrating phase peak at 40.5° illustrating phase evolution with increasing Mn evolution with increasing Mn content.   content.

Figure 4.25: Overview over secondary phase evolution in manganese rich samples with increasing Mn content through XRD.

Secondary phase precipitation Results for SE and BSE for thermally etched V5 sample are shown in Fig. 4.26 while the only polished samples are shown in Appendix B. Both images are taken from approximately the same area on the sample and the shift is due to sample drift in the instrument. In this case, black grains on BSE image are corresponding to the secondary phase. By comparing BSE image with SE image it can be seen that the secondary phase has a slightly different texture and it appears as darker grains in the SE image.

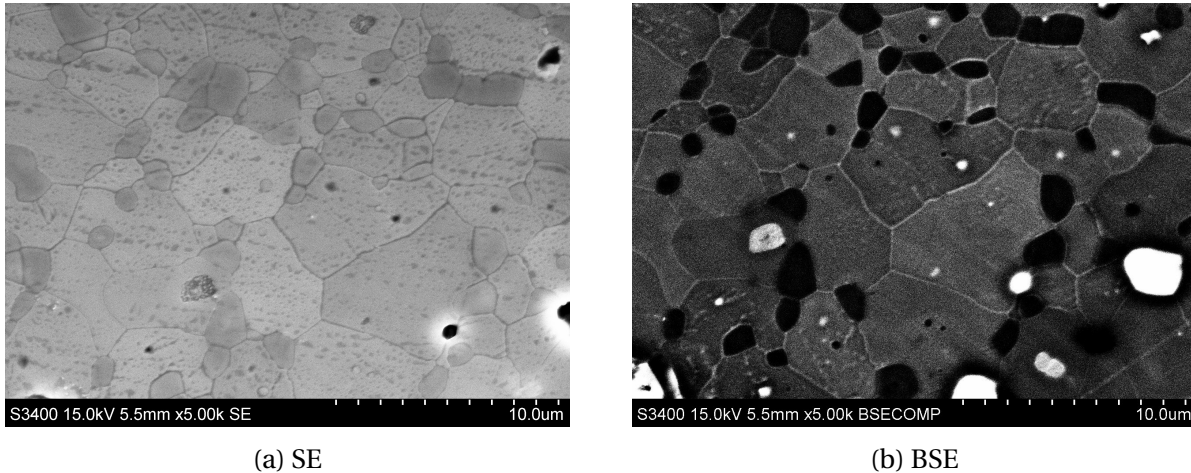(a) SE   (b) BSE

Figure 4.26: SEM images of dense V5 annealed at 1250°C for 3h and thermally etched at 1000°C in air.

EDS map scan of the etched sample, Fig. 4.27, clearly shows differences in intensity for Mn and Ca at various grains. The Ca and Mn maps are are showing exactly opposite trends in intensity supporting the conclusion that the grains, which in BSE image in Fig. 4.27 appear white, belong to marokite. Differences in secondary phase grain colours between Fig. 4.26 and Fig. 4.27 come from use of different imagining settings and not different phase composition.

Finally, line scans in Fig. 4.28 show the interphases between two grains where (a) is an interphase between $CaMnO_3$ and $CaMn_2O_4$ and (b) shows two grains consisting of $CaMnO_3$ with different crystallographic orientations.

Manganese rich sample shows precipitation of secondary phase in form of small grains, much smaller than CMO grains. The thermally etched sample shows that the precipitation happens on grain boundaries and on triple points between grains of the main phase.
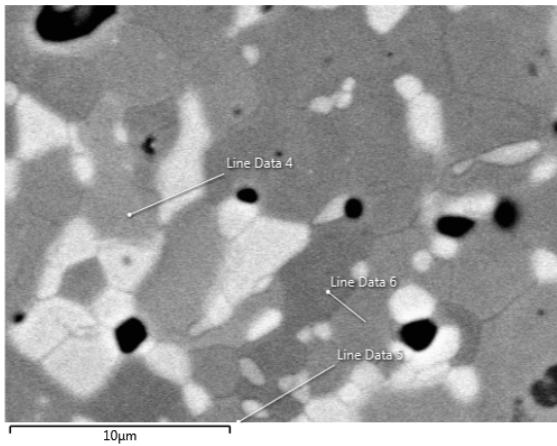
(a) BSE image with line scans indicated
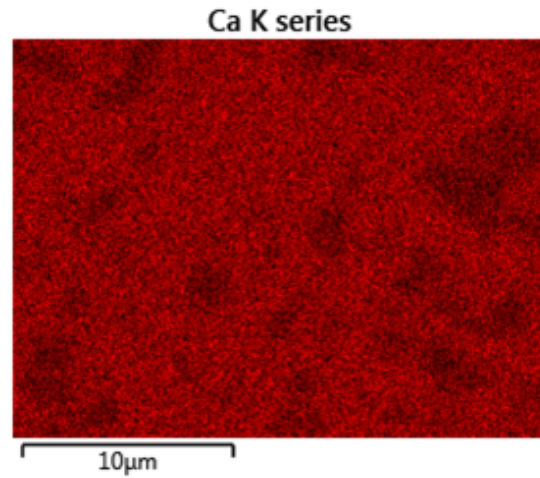
(b) EDS mapping of calcium
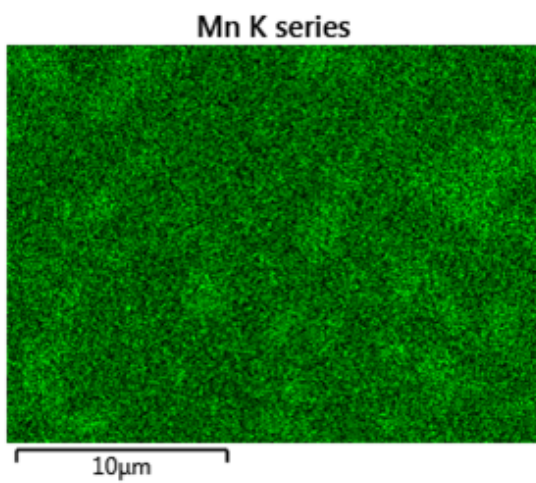
(c) EDS mapping of manganese
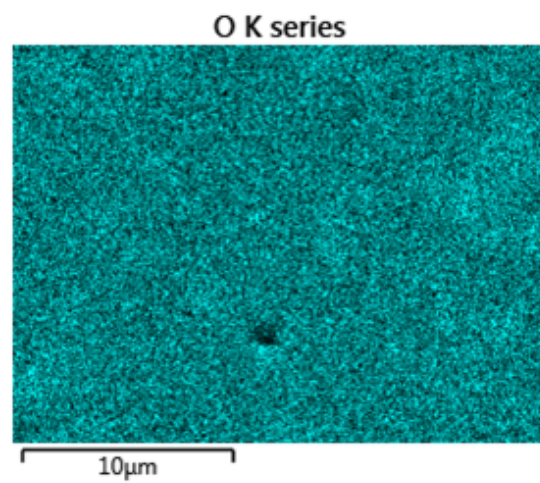
(d) EDS mapping of oxygen

Figure 4.27: EDS mapping of dense V5 annealed at 1250°C for 3h and thermally etched at 1000°C in air.

(a) Line 4   (b) Line 6
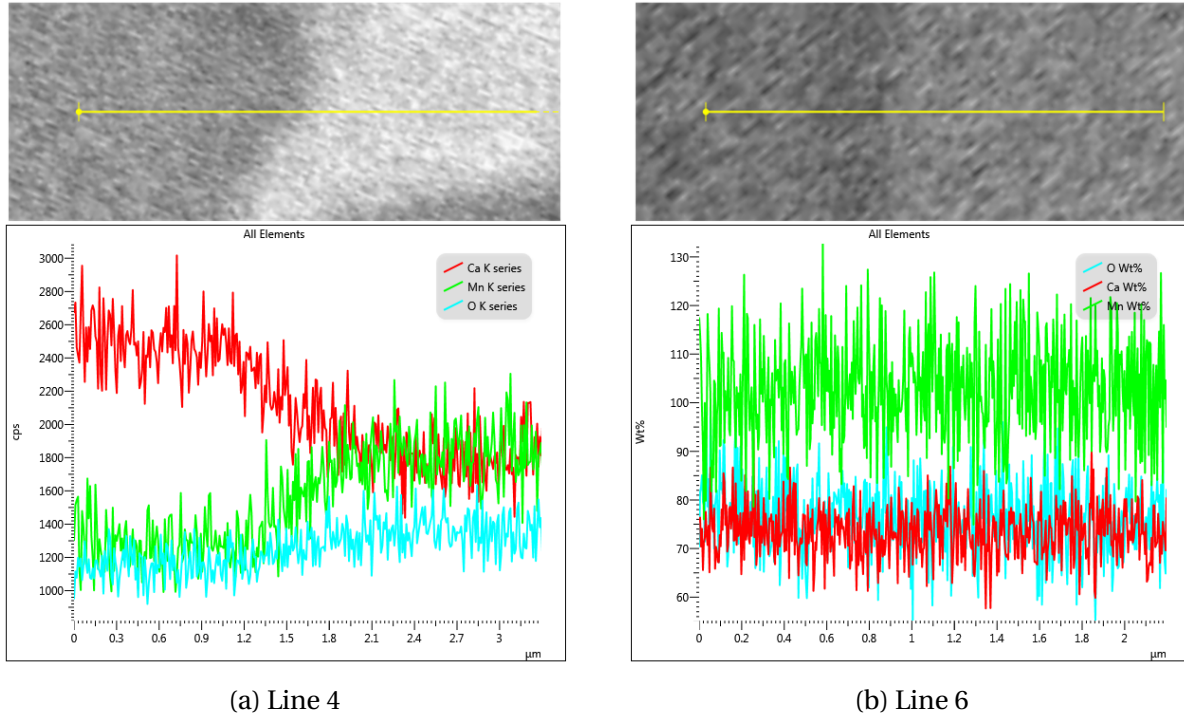
Figure 4.28: EDS Line scan analysis of dense V5 annealed at 1250°C for 3h and thermally etched at 1000°C in air. BSE image on top corresponds exactly with the patterns on the bottom. Placement of lines on the sample is indicated in the BSE image in Fig. 4.27

4.4 Thermal expansion coefficient

DIL measurement was performed with max temp of 910°C to obtain values for TEC used in thermal conductivity measurement. Obtained curves are presented in Fig. 4.29. An obvious trend is seen from those curves, where stoichiometric CMO expands the most and the expansion decreases with the increasing amount of secondary phase. Based on the slope of the curves, TEC was calculated using Eq. 3.6 and it is presented in Table 4.7. Curves were divided into four temperature regions due to noticeable changes in the slope. It can be observed that the change in slope occurs at nearly the same temperature for pairs of materials, where the first pair is made up of V0 and V2.5 and the second pair is V5 and V10.
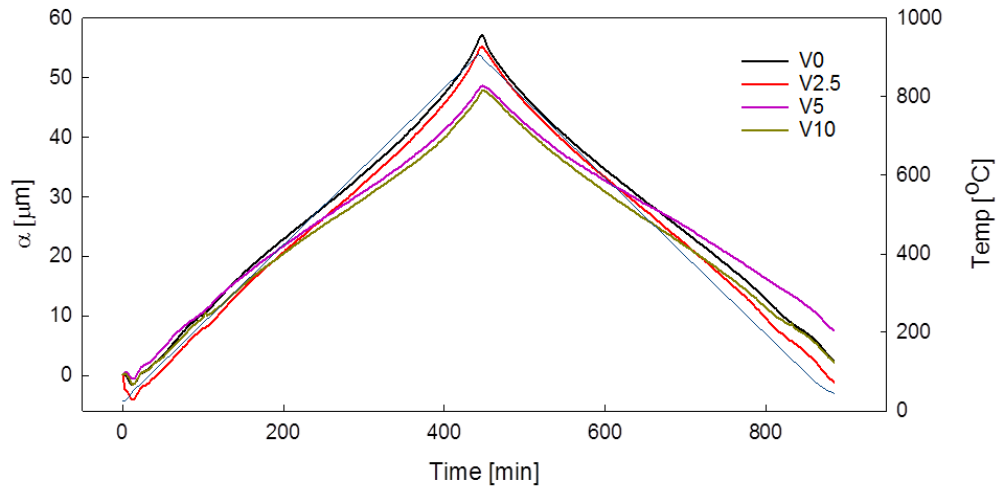
Figure 4.29: Thermal expansion curves obtained through DIL measurement in air. Max. temp = 910°C, no dwell time.

Table 4.7: Thermal expansion coefficients for selected temperature intervals obtained through DIL measurement in air.

	Heating [μm/°C]		Cooling [μm/°C]	
Temp [°C]	25-750	750-900	900-750	750-45
V0	0.058	0.090	0.076	0.059
V2.5	0.056	0.096	0.080	0.063
Temp [°C]	25-600	600-900	900-600	600-45
V5	0.052	0.058	0.048	0.046
V10	0.050	0.058	0.050	0.052

4.5 Electrical conductivity

Electrical conductivity data presented in Fig. 4.30 and Fig. 4.31 are the values obtained upon cooling from 900°C to room temperature. An example of the data obtained from the entire measurement is shown in Appendix F. It was decided to present data obtained upon cooling as oxygen stoichiometry is more defined after the sample has been heated up. This results in shorter relaxation time and smaller fluctuation of values.

Both plots show that electrical conductivity increases with increasing temperature as predicted. They also show that porosity has large impact on the electrical conductivity by decreasing its values. Finally, it can be seen that the secondary phase is increasing electrical conductivity, but the effect becomes less significant at higher temperatures.

Activation energy, E_a was calculated from the Arrhenius plot of electrical conductivity, Fig. 4.32, by calculating the slope of the linear part of the plot. Obtained values are presented in Table 4.8. They show that E_a decreases with increasing volume of secondary phase what correspond to increasing electrical conductivity.

Table 4.8: Activation energy, E_a, based on the slope of the $\ln(\sigma T)$ vs $1/T$ curve.

Sample ID	V0 (ρ=86.6%)	V0 (ρ=90.2%)	V2.5	V5
E_a [eV]	0.27	0.33	0.31	0.29

Figure 4.30: Electrical conductivity measured in air with a four point probe method. Conductivity values are obtained upon cooling for stoichiometric samples (V0) with different densities. Lines are added to guide the eyes.
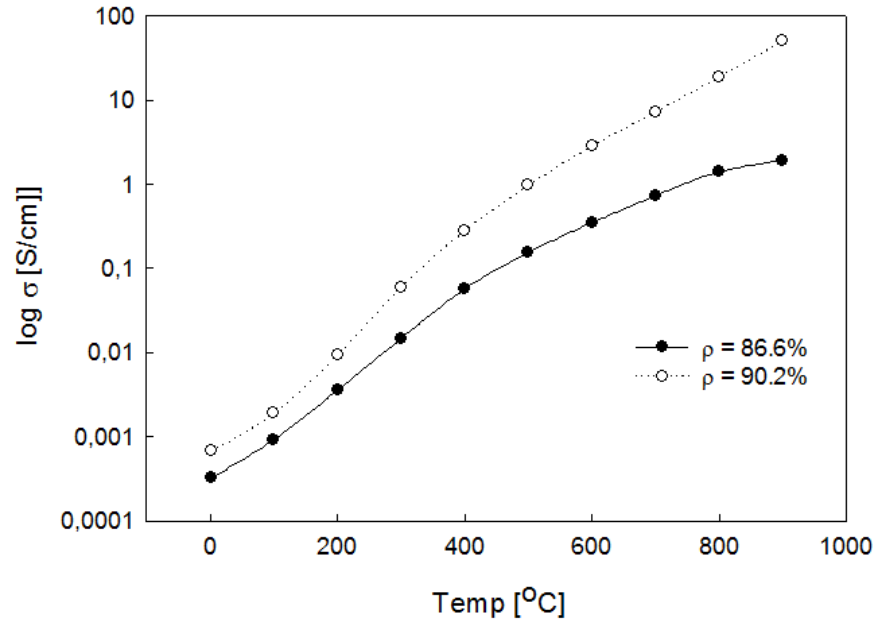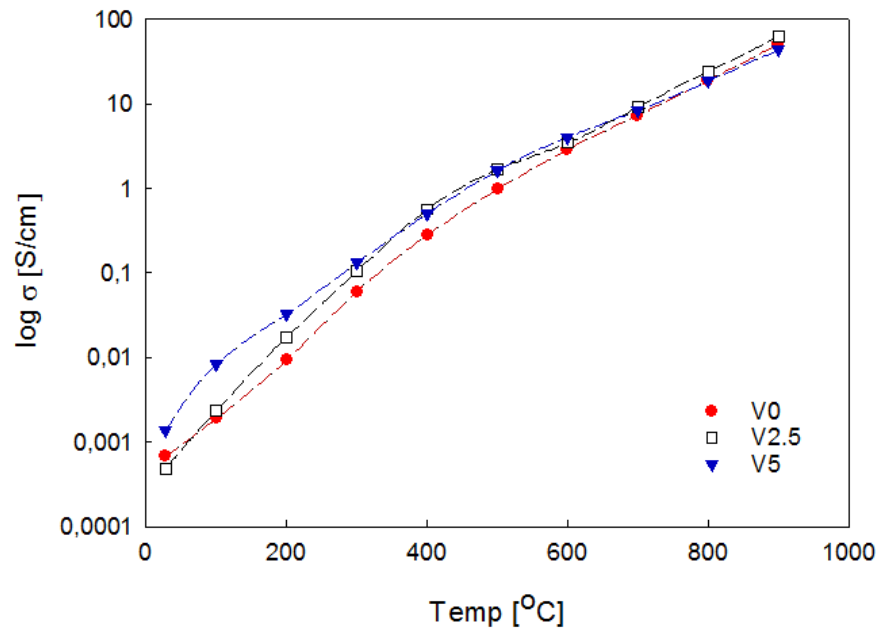
Figure 4.31: Electrical conductivity measured in air with a four point probe method. Conductivity values are measured for selected stoichiometries upon cooling. All samples have density higher than 90%. Lines are added to guide the eyes.
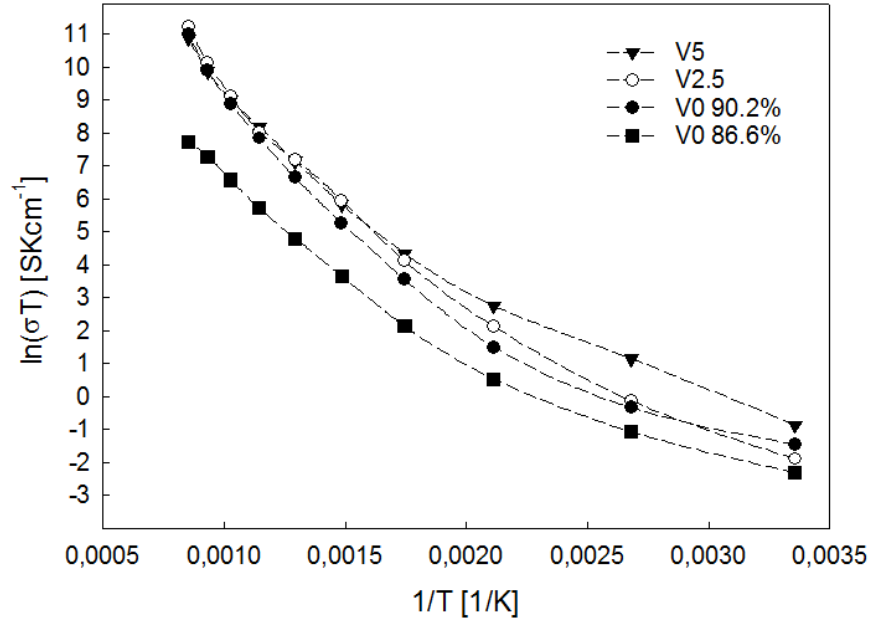
Figure 4.32: Arrhenius plot of electrical conductivity plotted for all investigated samples. Plot is based on the data presented in Fig. 4.31

4.6 Thermal conductivity

Thermal conductivity values were obtained up to 400-500°C and are presented in Fig. 4.33a). The thermal conductivity decreases with increasing temperature and it increases with increasing amount of secondary phase. In most cases standard deviation is about 0.03 making error bar of the same size as the symbols. Maxwell formula, Eq. 2.17 was used to estimate thermal conductivity for 100% dense samples. Obtained values are presented in Fig. 4.33b). Thermal conductivity data at 500°C for V5 are not available due to problems with the instrument.

Electrical and lattice contributions to the total thermal conductivity were calculated using Eq. 2.12 with L = 2.25 $\times 10^{-8} \Omega W/K^2$. [63] and are presented in Fig. 4.34. Those curves show that the electronic contribution is very low and negligible at low temperatures. At higher temperatures its contribution increases greatly and it increases with increasing secondary phase volume. Nevertheless, in comparison with the lattice part κ_{el} is much smaller in all temperature ranges.
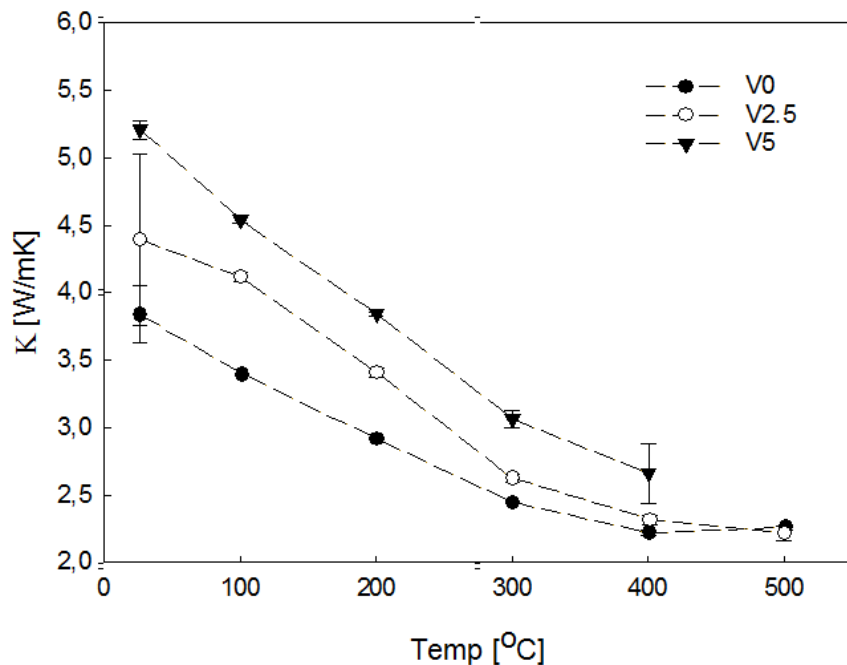
(a) Mean thermal conductivity values obtained for selected temperatures and stoichiometries together with error bars.
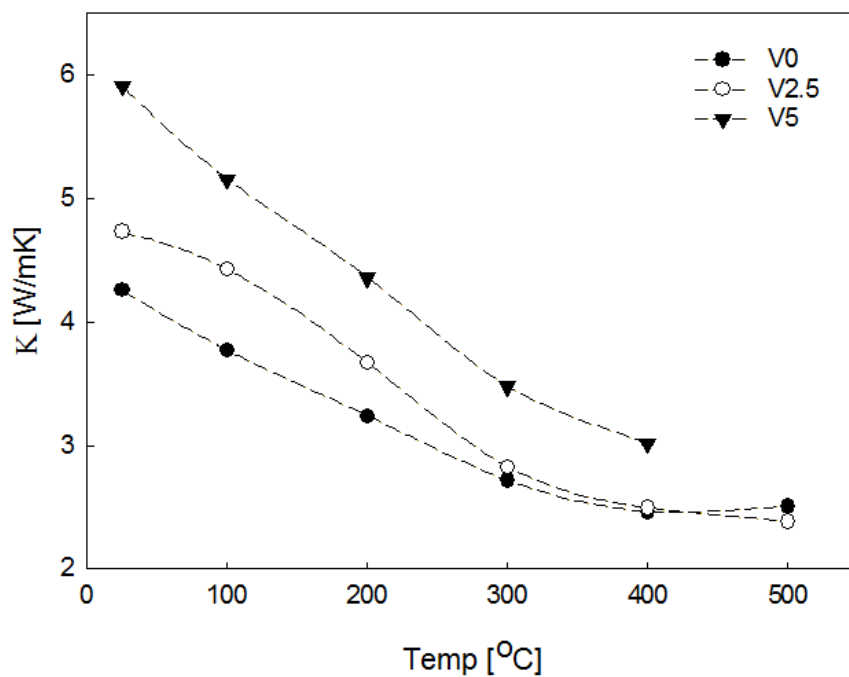
(b) Calculated values for completely dense samples. Data obtained from Maxwell equation and mean data values from laser flash measurement.

Figure 4.33: Results from laser flash measurement conducted in N_2 and on carbon coated samples. Lines are added as eye guides.
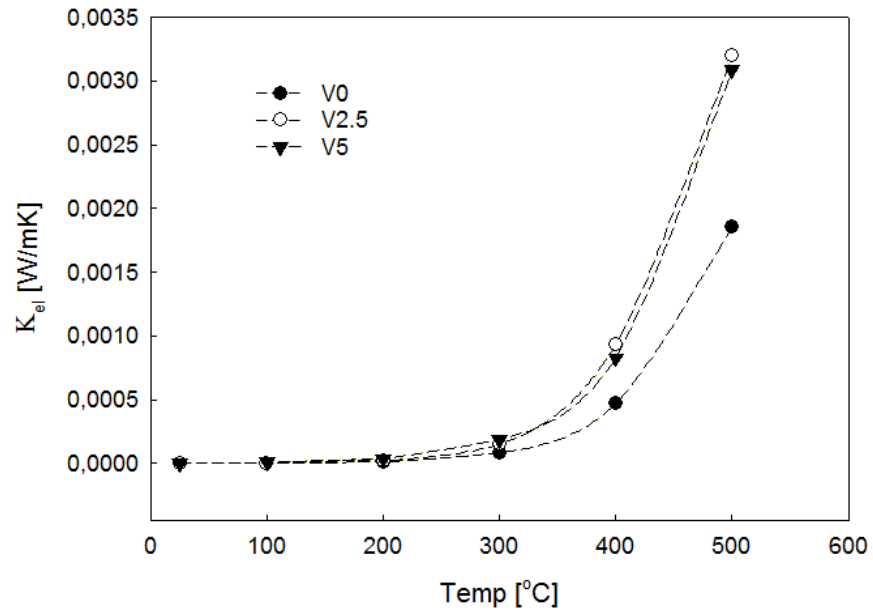
(a) Calculated electronic thermal conductivity, κ_{el}.
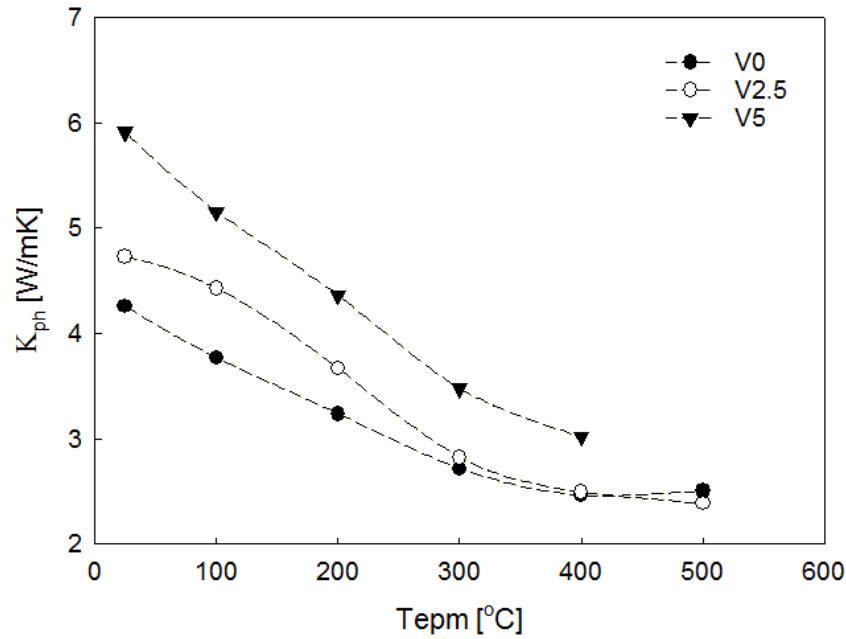
(b) Calculated lattice thermal conductivity, κ_{ph}.

Figure 4.34: Calculated thermal conductivity contributions based on 100% dense κ_{tot} values. Lines are added to guide the eyes.

4.7 Seebeck coefficient

Seebeck coefficient values presented in Fig. 4.35 are the values obtained upon cooling from 900°C (same as for electrical conductivity). An example of the entire dataset for a Seebeck measurement can be found in Appendix G. Measured Seebeck coefficient increases with increasing temperature and amount of secondary phase. V0 and V2.5 exhibit very similar behaviour while $|S|$ for V5 increases greatly at low temperatures. Seebeck coefficient was not measured at room temperature due to long time required to cool down and relax the sample.
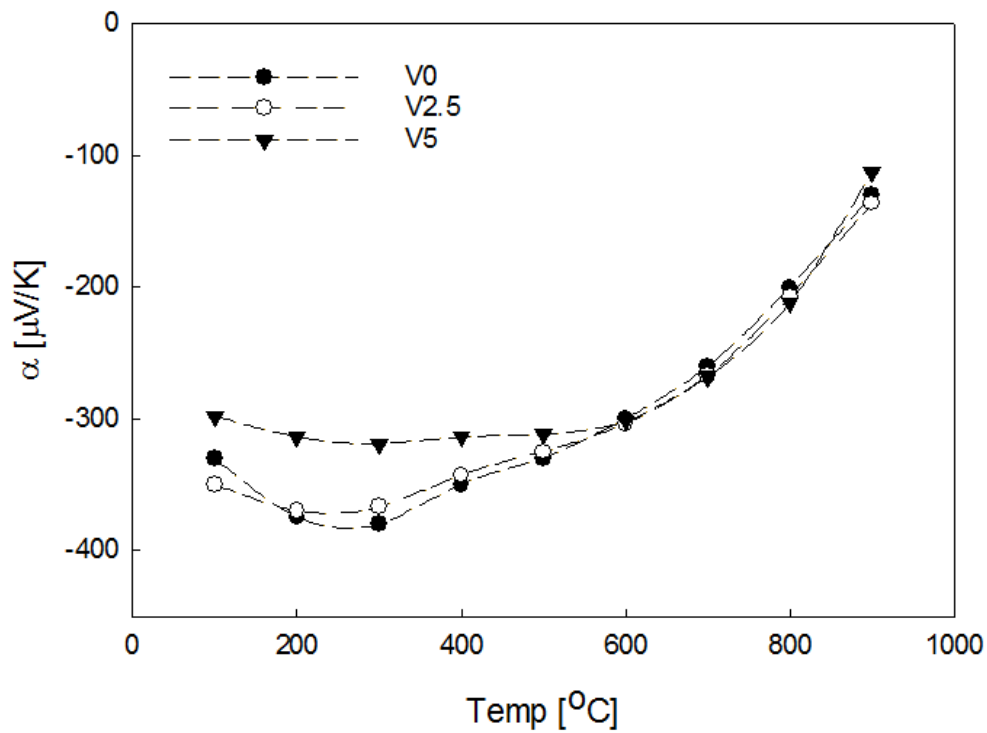
Figure 4.35: Seebeck coefficient values measured in air upon cooling from 900 - 100°C. Dashed lines are added just as eye guides

4.8   Power factor

Power factor (PF) was calculated from measured Seebeck coefficient and electrical conductivity and it is presented in Fig. 4.36. PF values are very low low at low temperatures and they increase with increasing temperature. The best PF was obtained for V2.5, exhibiting much higher values than the two other samples.
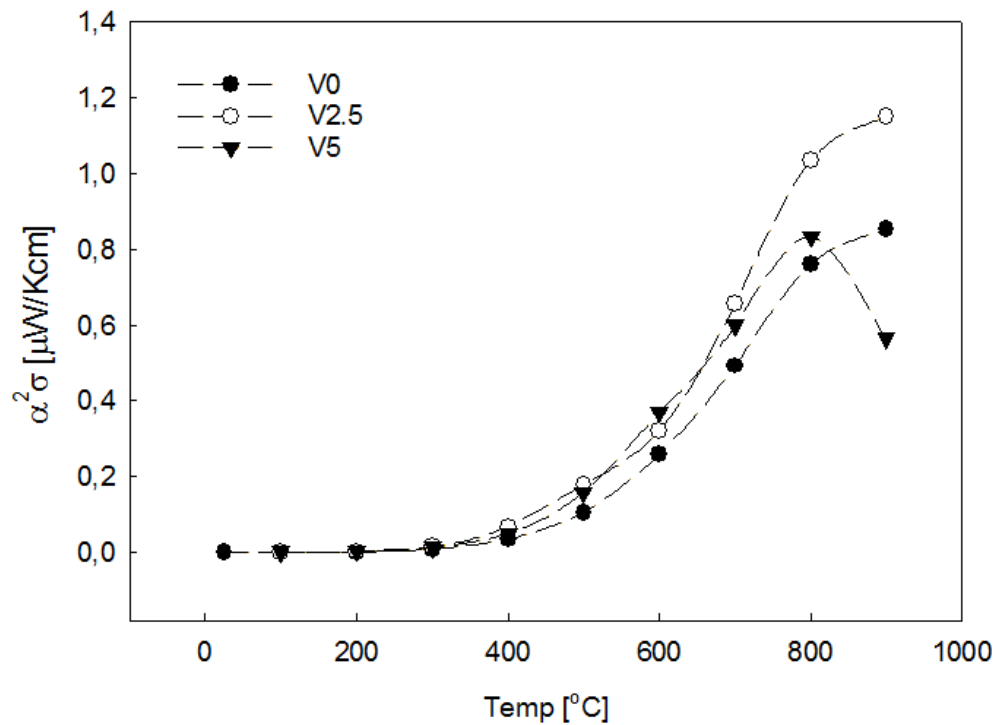
Figure 4.36: Calculated power factor values based on measured electrical conductivity and Seebeck coefficient values. Lines are added to guide the eyes.

4.9   Figure of merit

Thermoelectric figure of merit, zT, was calculated from measured values using Eq. 2.7. Calculations were performed for temperature range of 100-500°C and are presented in Fig. 4.37. zT increases greatly with increasing temperature with V2.5 reaching highest values.
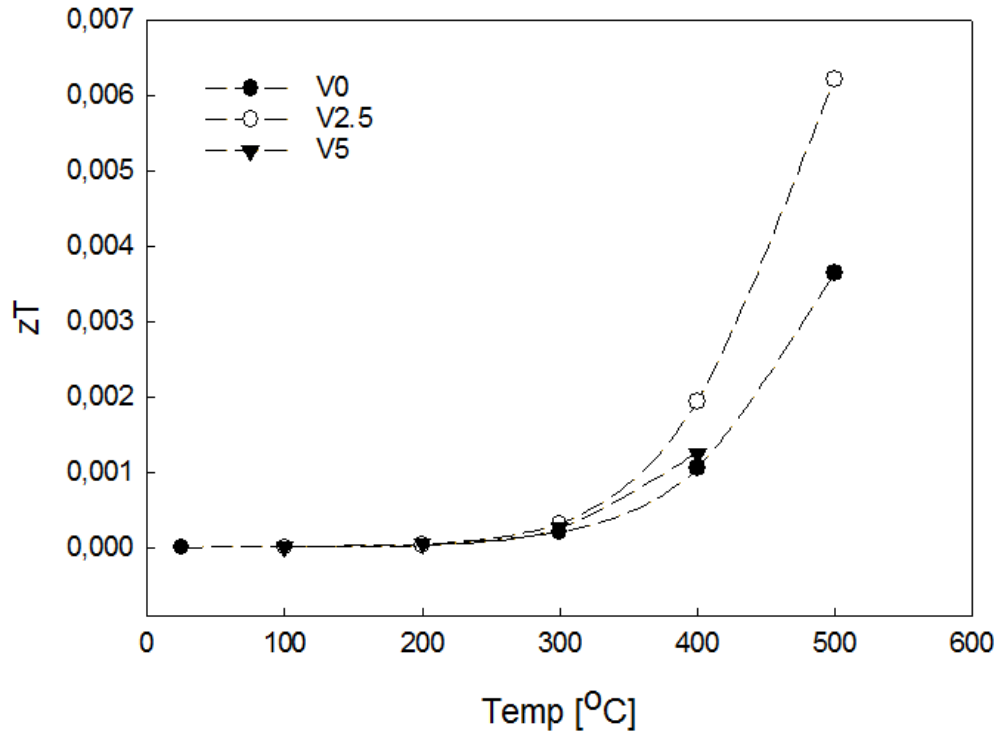
Figure 4.37: Calculated zT values based on measured thermal conductivity, Seebeck coefficient and electrical conductivity values.

Chapter 5

Discussion

5.1 Sinterability of $Ca_{0.5}Mn_{0.5}O$

As described in Section 4.1.2 several different approaches were investigated to obtain as high density of pure $Ca_{0.5}Mn_{0.5}O$ as possible. Firstly, particle size was reduced to increase packing ability and increase sinterability by increasing the driving force for sintering, which is caused by volume diffusion. Smaller particles provide shorter diffusion lengths thus enhance the sinterability. It can be easily observed from SEM images, Fig. 4.3a and Fig. 4.4, that particle size and shape change a lot in a course of milling time. Particles are not very uniform and the assumption made for BET analysis about particles being spherical does not hold very well. In spite of that, the results presented in Table 4.1 give a trend that is visible in the SEM images. Particle size decreases with increased milling time and the particle-size distribution narrows down resulting in more uniform particles with similar size. As a side effect of smaller particle size agglomerates of various sizes are being formed. To solve this problem sieving was used. This not only to removed remaining large particles but also formed soft agglomerates of relatively uniform size that pack well. Over all the particle size was decreased by about 50% from 8-10μm to about 5μm during 1h of milling. This is a significant improvement which is reflected in the increase in density by approx. 7%.

From DIL measurement in H_2, Fig. 4.5 it is easily seen that milled samples start sintering at lower temperatures and the overall shrinkage is greater than that for the one crushed with mortar. This is also confirmed by Archimedes density measurement conducted on pellets sintered

at 1250°C for 6h, Table 4.2, where pellets obtained from powder milled for 2h had the highest density and those crushed by mortar had the lowest. In spite of that, discolouring could be observed in the 2h milled pellets suggesting impurities being introduced to the material during milling, hence 1h milling time was chosen as the most optimal. Later on, EDS studies done on oxidized samples have shown minor zirconia particles in the material that could have come only from the milling jar and milling balls as both consist of zirconia. That is why 1h milling time was chosen as a fair balance between small particle size and low impurity content.

Introduction if CIP into sample preparation has shown to be a good method for improving the green body density and reducing the amount of open porosity. Density improvement of green body after use of CIP is easily noticeable as all sample dimensions shrink in all directions resulting in a pellet of volume smaller than before CIP. This shrinkage leads to density improvement by 33% which translates to nearly 14% higher density for the sintered material with after CIP.

Lastly the increase in temperature and dwell time was investigated. As a result multiple side reactions were observed in addition to observed changes in density. Firstly the reaction between alumina and $Ca_{0.5}Mn_{0.5}O$ at temperatures over 1250°C was observed. From phase diagram, C we can see that there is an eutectic point at 1287°C linking the stable CaO-MnO ss phase and two $CaO-Al_2O_3$ phases. This agrees well with what was observed after sintering at higher temperatures without Pt spacer. The remnants of the melted sample are dark green, suggesting large concentration of Mn^{2+}. Further, upon cutting through the alumina boat, it can be seen that the sample had reacted with the boat and started to dissolve it, filling the groove with the dark green Mn-rich phase. All of this implies a reaction between CaO and alumina and either dissolution of the obtained alloy into the bulk material of the boat or evaporation. To prevent this undesired side reaction Pt wire was used as a spacer between alumina and the sample. Pt is an inert material that is stable at high temperatures and an easy way to separate sample from the bottom of the boat.

Further increase of temperature with use of Pt as spacer resulted in dense pellets however they changed colour from green to white. This colour change suggests lower Mn^{2+} concentration within the sample. Evaporation of manganese is possible as highly reducing atmosphere is used which leads to very low partial pressure of oxygen (pO_2) during the reaction. At those
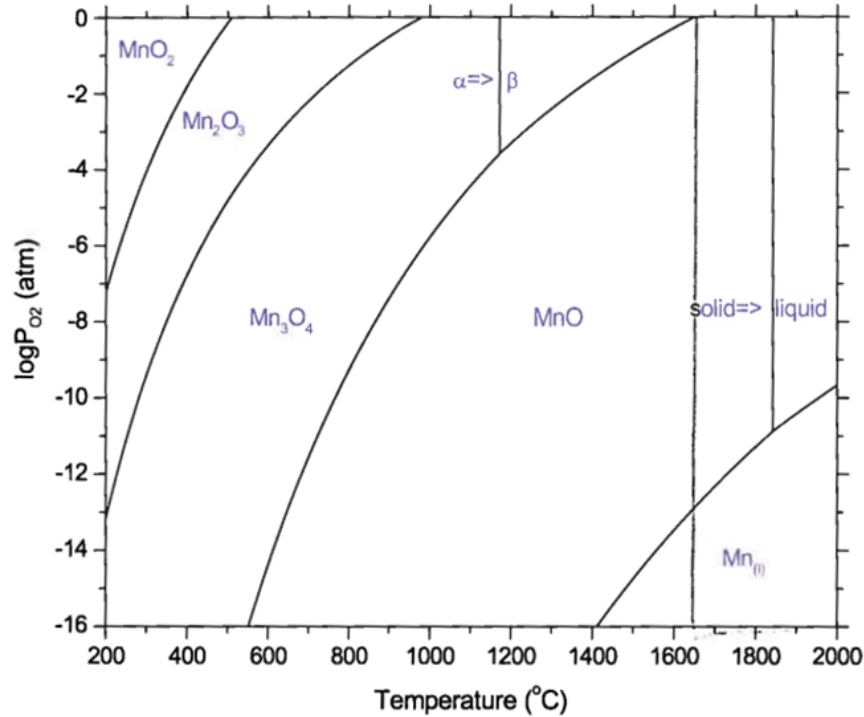
Figure 5.1: Stability of MnO as a function of temperature and oxygen partial pressure [46]

conditions material is being reduced to Mn metal which then proceeds to evaporate. This assumption is supported by Fig. 5.1 where when the line between MnO and Mn(l) is extrapolated further down, we see that it becomes possible to reduce MnO to Mn metal at 1300°C, given pO_2 is very low. Further, the vapour pressure of Mn is very high, 10^{-4} bar at 1020°C [2], and it increases with increasing temperature supporting the theory of Mn evaporation. To prevent this reaction a less reducing atmosphere must be used, hence pure N_2 was chosen for temperatures above 850°C. This temperature was chosen as it provides a good buffer to avoid the negative side-reactions, yet kinetics at this temperature are fast enough to reduce material to the rock-salt phase in case an oxidation has occurred while using an inert atmosphere. Pure N_2 is mildly reducing therefore it will keep pO_2 high enough to prevent full reduction to Mn-metal but not high enough to form perovskite. 5% H_2 was kept at lower temperature to reverse any potential oxidation of Mn^{2+} to Mn^3 and retain the perfect rock-salt crystal structure.

The sintering program has of course large impact on the microstructure of the material as illustrated in Fig. 4.8. Samples sintered at low temperatures have small irregular grains with large fraction of pores. In this case fracture goes along the grain boundaries, therefore grain

size and shape is easy to determine. As temperature is increased the grains are growing and first at 1350°C they become interconnected to the degree that it becomes hard to distinguish separate grains. Pore shape also changes from large voids, to smaller more spherical pores. The texture and steps on the surface of the grains/fracture surface that are seen in Fig. 4.8 c) and d) show that the fracture is happening through the grain and not along the grain boundaries. This means that the grain size is very large and thus strength of the material is lowered. As the grain size increases there are less grain boundaries that can deflect crack propagation or even prevent their formation. Further, large grains are not preferable from the thermal conductivity point of view, as grain boundaries are one of the phonon scattering agents. On the other hand, at hight temperatures, heat radiation in pores is taking place at much faster rate than heat propagation in the solid consequently increasing thermal conductivity of the material.

Finally, variation of sintering time was investigated. It has been shown that increase of dwell time increases the density, however the impact is lower than the one from temperature increase, as described in Section 4.1.2. All those observations agree well with the assumption of grain boundary diffusion being the dominant mass transport mechanism during sintering [12] as such mechanism is more affected by changes in temperature and particle size than in dwell time.

5.2   Oxidation and crack formation

TG analysis of milled powders, Fig. 5.2 and DIL curves of sintered pellets, Fig. 5.3 we can easily notice that corresponding compositions start to oxidise at different temperatures. Sample in TG start to oxidise at lower temperature because it is in powder form which gives larger surface area that is exposed to oxygen and shorter diffusion path. This results in earlier oxidation than in DIL, where samples were sintered pellets. This illustrates very well how oxygen diffusion is affected by the porosity and how it will translate to conversion speed from rock-salt to perovskite structure.

A closer look at TG curves from stoichiometric (VO) and manganese rich samples (V5 and V10) shows some minor differences in mass changes for both types of materials. Although all initial mass increase is nearly exactly the same, V0 is picking up less oxygen than V5 and V10

as as there no secondary phase with four oxygen atoms forming. It also stabilizes fairly quickly when the temperature reaches maximum and stays level until cooling, when it once again picks up oxygen, as it is very common for perovskite materials. V5 and V10, on the other hand, seems to be picking up oxygen at very low rate throughout the entire plateau at max. temperature as to then start loosing mass shortly after cooling begins. Those mass changes are associated with formation of two secondary phases in addition to transformation of rock-salt structure to perovskite. Those transformations can be represented as:

$$Ca_2Mn_3O_8(s) = CaMnO_{3-\delta}(s) + CaMn_2O4(s) + \frac{\delta + 1}{2}O_2 \tag{5.1}$$
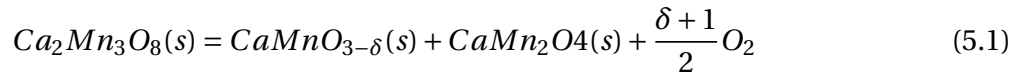
As temperature increases $Ca_{0.5}Mn_{0.5}O$ is being oxidized to $CaMnO_3$ hence the mass increase. At about 570°C $Ca_2Mn_3O_8$ (2:3 phase) begins to form contributing to further mass increase. At temperatures above 850°C the 2:3 phase is being transformed to marokite which slows down the mass increase during dwell time. Upon cooling the material once again finds itself where the 2:3 phase is stable. Oxygen is necessary for its formation and it will come from perovskite as it provides the shortest diffusion path. This reaction is most probably the cause of mass decrease that can be observed in V5 and V10 upon cooling.
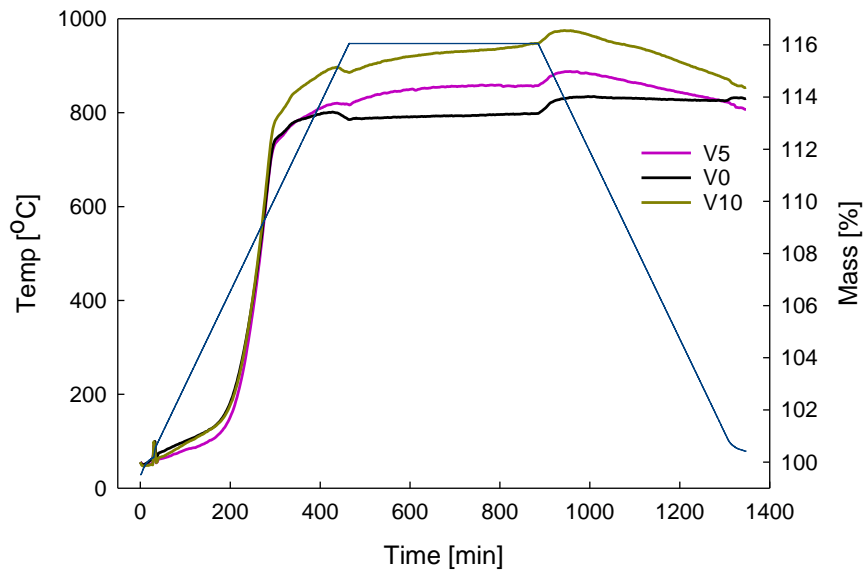

Figure 5.2: Comparison of TG results from stoichiometric (V0) and manganese rich (V5 and V10) samples.

DIL measurement present similar initial behaviour. Both samples start to oxidise at similar temperature and similar speed. The manganese rich sample (V5) goes through an intermediate step where 2:3 phase is formed which is later transformed to marokite. The transformation between 2:3 phase and marokite, which occurs at about 850° C is not visible in the curve because cell volumes of both phases are nearly identical (Appendix E). Further, the sample cracks at relatively low temperature due to secondary phase formation that is much larger than the perovskite, which also affects the measurement and collected data after sample disintegration.
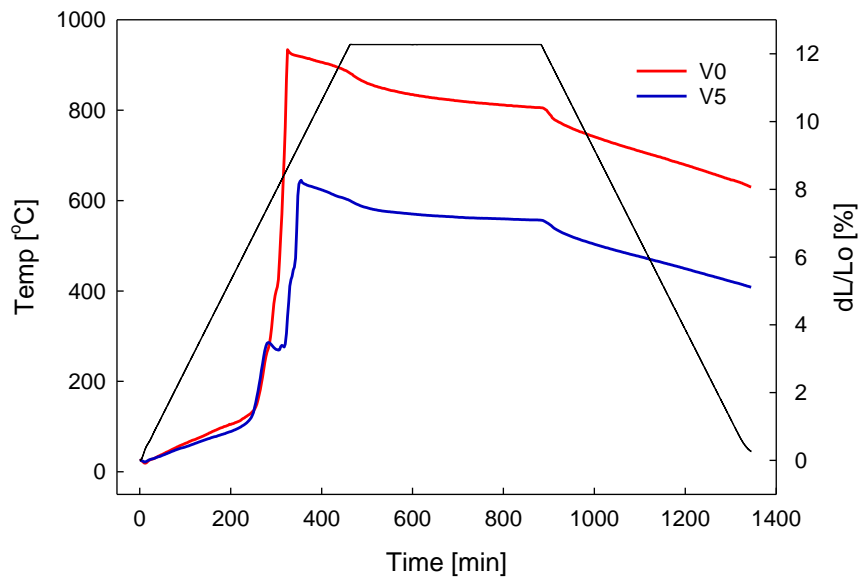
Figure 5.3: Comparison of DIL results from stoichiometric (V0) and manganese rich (V5) samples.

As described in Section 4.2, special heat treatments had to be applied for samples of different density to prevent cracking. Due to differences in the unit cell volumes between the reduced phase and the newly forming phases, material will expand. Low density materials are easiest to oxidise as high porosity prevents crack propagation and gives enough of free space for the structure to expand into without causing any internal strains or stresses. High density samples do not have this option, hence sufficiently high temperature is needed to induce creep. Transformation from rock-salt structure to perovskite is the easiest, since it follows the topotactic reaction mechanism with no cation rearrangement. In case of manganese rich samples cation rearrangement is needed to form first 2:3 phase and then marokite and this will cause greater stresses in the

material than perovskite formation. To anneal those stresses and prevent crack formation oxidation has to be performed at high temperatures. At this stage creep rates are sufficiently high to provide enough flexibility within the material for cations to move around freely.

In spite of relatively high annealing temperatures, microcracks could be observed after polishing sample's surface. Their amount increased with increasing amount of secondary phase suggesting that the creep rate was to low or microstructure of the rock-salt phase was too weak due to large grains to withstand secondary phase formation. A better phase distribution in the material with smaller grains could prevent this from happening as grain boundaries are a very good mechanism for crack deflection and reduction of internal stressed within the material.

5.3   Secondary phases

In case of stoichiometric CMO no secondary phases were observed in either BSE or EDS images as expected. Even annealing at very low temperatures lead to formation of perovskite and it is partially reduced form, $CaMnO_{2.8}$. This, however, cannot be considered as a two-phase material since no reduced phase is observed and the oxygen deficiency is barely noticeable as very small peaks and a broadening in the main peak. In all cases peak splitting can be observed at high θ values which indicates ordered oxygen vacancy distribution. [14]

In BSE images of both stoichiometric and manganese rich samples some of the large grains belonging to the main phase have different shade of grey. Upon analysing them with line and point scan it became apparent that they have exactly the same composition and the different colour in BSE image is due to different crystallographic orientation of the neighbouring grains.

When analysing manganese rich sample, the secondary phase is easily noticeable. It precipitates mainly along grain boundaries and on triple points between main phase grains as expected. The secondary phase grains are also visible in SE having slightly different morphology than the main phase.

Although it is impossible to obtain two-phase material consisting of perovskite and the reduced phase, formation of shrinking core in N_2 under very low O_2 pressure gives good insight into reaction mechanism. Not only it confirms the topotactic reaction mechanism but also the oxidised phases that are formed are in agreement with the work of Bakken [8]. He has shown

that under reducing conditions and very low, pO_2, $CaMnO_3$ decomposes according to following reaction:

$$CaMnO_{3-\delta} \rightarrow \frac{1}{3}Ca_2MnO_{4-\delta'}\frac{1}{3}CaMn_2O_4\frac{1-3\delta\delta'}{6}O_2 \tag{5.2}$$
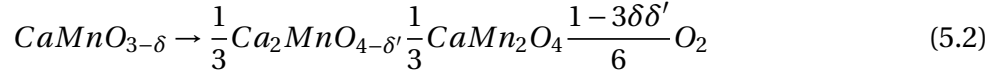
As shown in XRD pattern, Fig. 4.21, both phases are present. In addition highly reduced calcium manganate phases are also present. Since the reaction that was observed is the opposite to the one studied by Bakken, this means that in this case δ is very large and the reaction is far from completion, as supported by still large presence of the reduced phase.

5.4   Electrical conductivity

Study of electrical conductivity has shown that it increases with increasing temperature and increasing amount of secondary phase. The obtained values are lower than expected but the high temperature values for stoichiometric CMO agree quite well with data published by Schrade [57] assuming 1atm partial pressure during annealing as well as other publications. One potential causes for lower than expected electrical conductivity values are zirconia impurities that were found with EDS, Fig. 4.15. Although impurities were found within grains, a placement that affects conductivity less than if it was on grain boundaries, Zr is an insulator which most probably affected the electrical proprieties to some extend. Second option is the impact of porosity and microcracks. Comparison of electrical conductivities of stoichiometric CMO shown in Fig. 4.30 clearly shows that porosity has high impact on electrical transport, especially at high temperatures. In case of manganese rich samples, V2.5 and V5, they are both 3-4% denser than the dense V0, something that can partially contribute to differences in electrical conductivity between the three studied materials.

An unexpected discovery was the enhancement of electrical conductivity with increasing volume of secondary phase, as marokite is highly insulating. [53] This effect is most pronounced at low temperatures and it gradually decreases as the temperature increases. The increase in electrical conductivity is due to changes in pO_2 that lead to changes in oxygen stoichiometry in perovskite, δ and also changes in $\frac{Mn^{3+}}{Mn^{4+}}$ in the material system. Since the conduction mechanism in CMO is governed by small polaron hopping, described in Section 2.5.2, it is proportional to

$\frac{Mn^{3+}}{Mn^{4+}}$. This means that it will decrease with increasing concentration of Mn_{3+} which increases with decreasing pO_2 [57].Oxygen stoichiometry in the material is affected not only by diffusion of oxygen from air into the structure but also by phase relations between the three phases that are stable at different temperatures. The mixed valence system that we are looking at consists of Ca $\overset{3+/4+}{Mn}$ $O_{3-\delta}$, $Ca_2\overset{4+}{Mn_3}O_8$ and $Ca\overset{3+}{Mn_2}O_4$. In addition to transition between the 2:3 phase and marokite at about 850-900°C $CaMnO_3$ changes crystal structure from orthorhombic to tetragonal in the same temperature regime.

At high temperatures material consists of marokite and fully oxidized CMO. This results in cubic structure for CMO that is responsible for improvement in electrical conductivity and compensates for decrease in Mn^{3+}-ion concentration that provides free electrons for current conduction. When the temperature decreases the degree of orthorhombicity in CMO increases but so does the amount of Mn^{3+}. At temperatures below 850°C the 2:3 phase becomes stable. This causes oxygen diffusion associated with this this transition that leads to formation of oxygen vacancies in CMO. This increase in δ is responsible for higher electrical conductivity values for manganese rich samples at lower temperatures.

Finally, lack of linearity in Arrhenius plot of electrical conductivity, Fig. 4.32 further supports change in oxygen stoichiometry. Further, studies have shown that other events might be taking place at higher temperatures potentially leading to change in conduction mechanism. [34]

Calculations of activation energy (E_a) presented in Table 4.8 have produced values nearly twice as high to those assumed as reference point for CMO prepared by ceramic route, however higher values namely 0.22eV [35] and 0.28eV [34] were also published. They decrease with increase in secondary phase volume but they also decrease with decreasing density. Deviation linearity observed at lower temperatures is due to deviation in oxygen stoichiometry in the material. The decrease in E_a agrees well with increase in electrical conductivity with increasing amount of secondary phase.

5.5 Thermal conductivity

From the measured data. Fig. 4.33 a) we see that the thermal conductivity of a material increases with increasing amount of secondary phase. This is caused by two factors: firstly grains of CMO

are very large, something that is very beneficial for the heat transfer through the material, secondly, heat conductivity of the secondary phase is relatively large, approx. 3.6W/Km at room temperature [74] comparing to 3.4W/Km [44] for stoichiometric CMO.

Since it was shown that electrical conductivity is enhanced by formation of secondary phases, electronic contribution to thermal conductivity was calculated from Eq. 2.12 and presented in Fig. 4.34. We can see that at low temperatures, the contribution is negligible, however it increases greatly with increasing temperature.

Another possibility is enhancement of the electrical part of thermal conductivity that diminuates effects of lowering of the lattice part of thermal conductivity. This shows that although the crystal structure of the secondary phase is completely different than the one of bulk material the thermal conductivity proprieties are so similar that the impact on thermal conductivity is not very large. Nevertheless, obtained values are comparable with the data found in literature. [9] [63]

When recalculating the values using Maxwell equation 2.17 we can see that even the low porosity contributed to lowering of the thermal conductivity. Also the differences between the three stoichiometries decrease and it seems that 2.5vol% potentially can have positive impact on lowering of thermal conductivity. Further, those recalculated values agrees quite well with what was published in literature. [27]

Calculations of thermal conductivity contributions have shown that the contribution from electronic part is very low compared to the lattice part and it accounts for less that 10% of the thermal conductivity. Nevertheless, that contribution increases with increasing volume of secondary phase and it has a large influence at higher temperatures.

5.6 Seebeck coefficient

Negative sign for Seebeck coefficient confirms the fact that CMO is a n-type semiconductor. Measured values presented in Fig 4.35 increase with increasing temperature what can be connected to material's semiconductor behaviour. Further, values increase with increasing secondary phase volume what once again can be explained by increased carrier concentration caused by the transition between marokite and 2:3 phase leading to oxygen non-stoichiometry

in perovskite. The biggest differences can be observed at low temperatures where the secondary phase has strongest influence on $\frac{Mn^{3+}}{Mn^{4+}}$ ratio. High temperature values are quite similar as the oxygen stoichiometry is then well defined and secondary phases have much smaller influence. This is a positive development as the absolute Seebeck coefficient value should be as high as possible in order to obtain good conversion of heat to electricity. Measured values agree well with what was previously published in the literature. [63] [57]

5.7 Power factor and Figure of merit

Calculated power factor (PF) which is presented in Fig. 4.36 increases with increasing temperature and secondary phase. This is an expected trend since both α and σ expressed similar behaviour. This trend is also comparable with data published in literature [35] [37] as it is typical for this material system. Out of the three investigated stoichiometries V2.5 has the highest PF. This suggests that introduction of 2.5vol% of marokite has a beneficial effect on charge carrier concentration in the material .

Calculated figure of merit, Fig. 4.37 shows values lower than anticipated. This is due to low electrical conductivity and high thermal conductivity. In theory, based on Eq. 2.15, it was stated that zT can be enhanced when $\frac{\kappa_{ph}}{\kappa_{el}} << 1$. Comparison of κ_{el} and κ_{ph} in Fig. 4.34 shows clearly that this criterion is not fulfilled with $\frac{\kappa_{ph}}{\kappa_{el}}$ being much larger than 1. Further, electrical proprieties are affected by impurities and phase transitions that govern oxygen stoichiometry resulting in less than optimal conditions. Over all sample with 2.5vol% of marokite provides highest values with zT = 0.0062 at 900°C.

Chapter 6

Conclusion

In the course of this work a synthesis procedure for CMO via a reduced phase was determined. Solid state reaction was used to synthesise a two-phase material with desired stoichiometry and high density. Materials synthesised through this route consist of very large grains of $CaMnO_3$ with secondary phase, $CaMn_2O_4$, precipitating on grain boundaries and triple points of the large grains. Obtained densities were over 90% of the theoretical density, however large grains and large difference between unit cell volumes of both coexisting phases lead to formation of micro-cracks and lowering in mechanical strength. An alternative synthesis processes, f.eks. powder precursor synthesis through spray pyrolysis or spark plasma sintering should be investigated to obtain materials with finer grain structure and higher strength.

Obtained electrical conductivity values were lower than anticipated. They increased with increasing temperature and increasing amount of secondary phase. The enhanced electrical conductivity for the two-phase material is due to change in $\frac{[Mn^{3+}]}{[Mn^{4+}]}$ ratio. This change is caused by change in pO_2 and transition between $CaMn_2O_4$ and $Ca_2Mn_3O_8$ leads to an increase in δ. At higher temperatures, effects of secondary phase are less significant as oxygen stoichiometry is more defined and less influenced by the secondary phase.

Thermal conductivity measurements show that it increases with increasing secondary phase volume. This is caused by relatively high thermal conductivity of the secondary phase and large grains that are beneficial for heat transport. In order to decrease thermal conductivity a denser material with finer microstructure should be synthetized. The amount of marokite should not exceed 2.5vol% as this amount exhibits promising trends, yet higher amounts give enhanced

thermal conductivity potentially due to increase in electronic part of thermal conductivity due to increase in charge carrier density.

The increase in charge carrier density caused slight increase in Seebeck coefficient values for manganese rich samples. All obtained Seebeck coefficient values are negative and they increase with increasing temperature what confirms that $CaMnO_3$ is an n-type semiconductor. The biggest impact of change in carrier density on Seebeck coefficient can be seen for V5 while values for V2.5 and V0 are nearly the same. Preservation of highly negative Seebeck coefficient is crucial for this material as it determines conversion of heat into electricity.

Calculated power factor and figure of merit are lower than expected. This is caused by low electrical conductivity and high thermal conductivity. Both zT and PF increase with increasing temperature with 2.5vol% sample exhibiting highest values. This suggests that 2.5vol% represents a limit for marokite allowance in the CMO system. The largest obtained zT value was for V2.5 at 900°C with zT = 0.0062. In order to enhance zT electrical conductivity should be enhanced while thermal conductivity should be lowered. Taking the 2.5vol% stoichiometry as a starting point, since it resulted in best values, microstructure of the material should be changed as to obtain smaller grains with more grain boundaries to include additional phonon scattering agent as marokite isn't enough. Further electrical conductivity could be enhanced through doping in order to obtain more optimal values.

List of roman symbols

Symbol	Description
#	Number of units
A	Crossectional area
A	Pre-exponential factor in Arrhenius equation
A_{BET}	BET surface area
C_V	Heat capacity at constant volume
$C_{v,el}$	Electronic specific heat per volume
d	Sample thickness
D	Particle diameter
e	Electron charge
h	Planc's constant
I	Electric current
k_B	Boltzman's constant
l	Distance between voltage probes (in Eq. 3.11)
l	Length of the sample
l_{el}	Electron mean free path
l_{ph}	Phonon mean free path
L	Lorentz number
l_{ph}	Phonon mean free path
m^*	Effective carrier mass
n	Charge carrier concentration
P	Electric power

Q	Heat
r	Ionic radius
R	Electrical resistance
S	Seebeck coefficient
t	Time
t	Goldsmith tolerance factor (Eq. 2.20)
$t_{1/2}$	Half-time
T	Temperature
T_h	Temperature at the hot end
T_c	Temperature at the cold end
U	Voltage
V	Volume
x	Position on the sample
zT	Dimensionless thermoelectric figure of merit

List of greek symbols

| Symbol	Description
α	Thermal expansion coefficient (Eq. 3.6)
α	Thermal diffusivity (Eq. 3.9)
β	Thomson coefficient
ϵ	Theoretical conversion efficiency
ϵ	Emissivity (Eq. 2.16)
η_c	Carnot efficiency
κ_{tot}	Total thermal conductivity
κ_{el}	Electronic thermal conductivity
κ_{ph}	Lattice thermal conductivity
Λ	Electron mean free path
ν	Concentration and velocity of phonons
ν_e	Electron velocity
Π	Peltier coefficient
Π_{closed}	Closed porosity
Π_{open}	Open porosity
Π_{true}	Total porosity
ρ	Density
$\rho bulk$	Bulk density of the material
ρ_{liq}	Density of isopropanol
ρ_{rel}	Relative bulk density in %
σ	Conductivity

List of abbreviations

Abbreviation	Description
BET	Brunauer-Emmett-Teller technique
BSE	Backscatter electron microscopy
CIP	Cold isostatic press
CMO	Calcium manganate $CaMnO_3$
DIL	Dilatometry
EDS	Energy dispersive spectroscopy
$Eq.$	Equation
$Fig.$	Figure
$i.e.$	that is
FOM	Thermoelectric figure of merit
PF	Power factor
rpm	Revolutions per minute
SEM	Scanning electron microscopy
tc	Termocouple
TE	Thermoelectric
TEC	Thermal expansion coefficient
$temp.$	Temperature
TGA	Thermogravimetric analysis
TMO	Transition metal oxide
XRD	X-ray diffraction
YZT	Yttrium stabilized zirconia

Appendix A

SEM images of raw powders
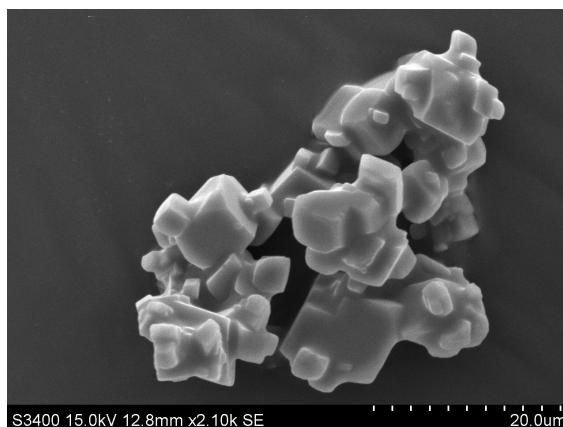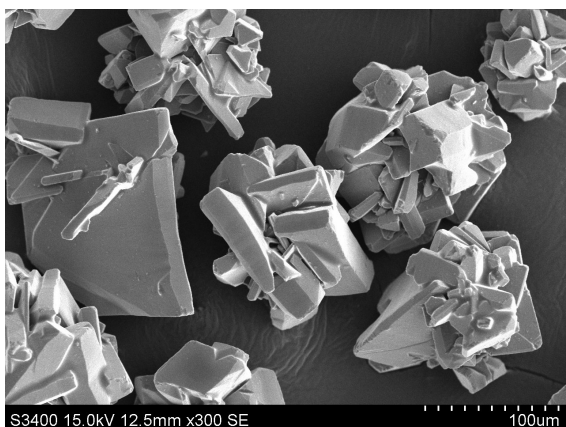
(a) Raw MnO_2 powder as received from Sigma-Aldrich

(b) Raw $CaCO_3$ powder as received from Sigma-Aldrich

Figure A.1: SEM images of precursors. Gold-plated for better conductivity.

Appendix B

Determination of reaction sintering program

Sintering program for single phase rock-salt structure formation was determined during specialization project and it was based on a DIL measurement, Fig. B.1. The max temperature was set to 1350°C and N_2 was used as the mildly atmosphere.
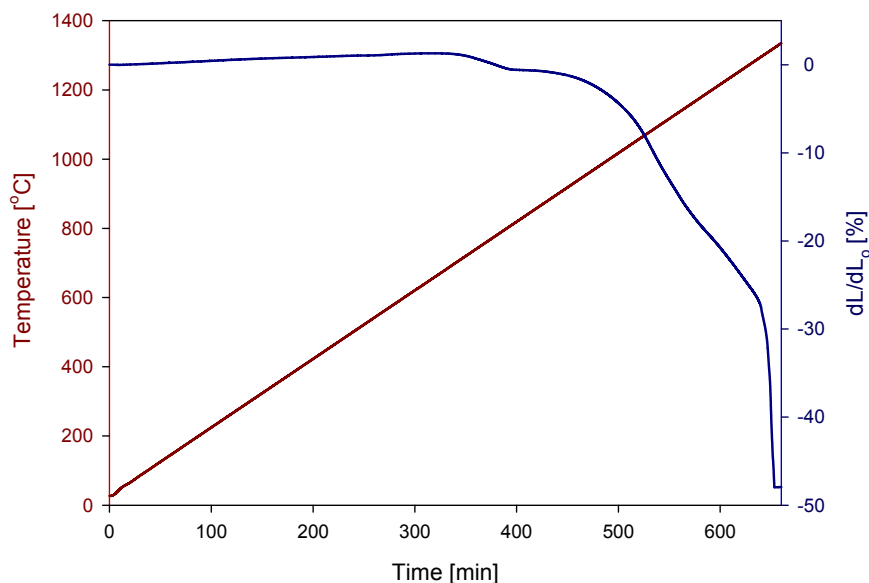

Figure B.1: Investigation of sintering proprieties of raw mixed powders - DIL measurement in N_2 with max temp. of 1350°C. Conducted during specialization project work.

Based on that curve, a maximum temperature of 1250°C was chosen as this is the maxi-

mum temperature for the material to stay stable and not react with alumina. After that a drastic change in dL/Lo can be observed that corresponds to melting of the precursors upon reaction with alumina.
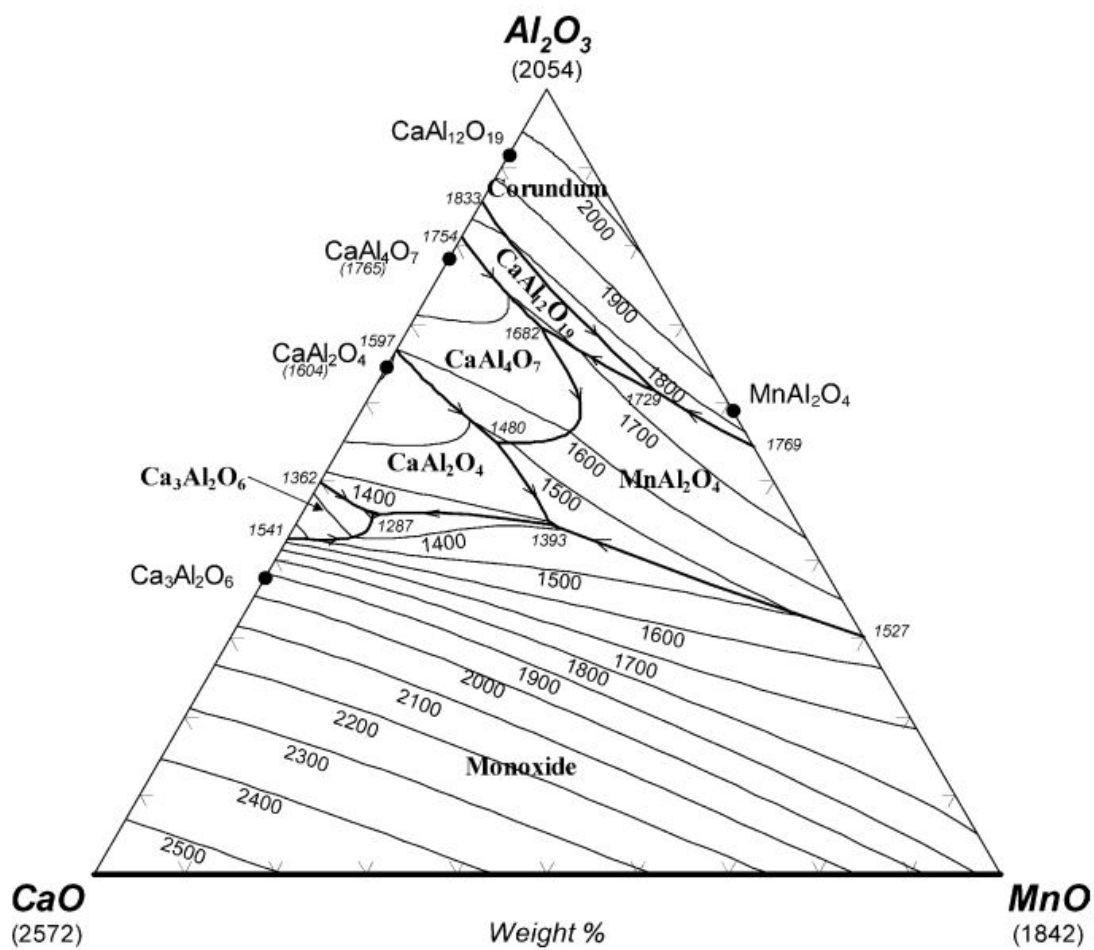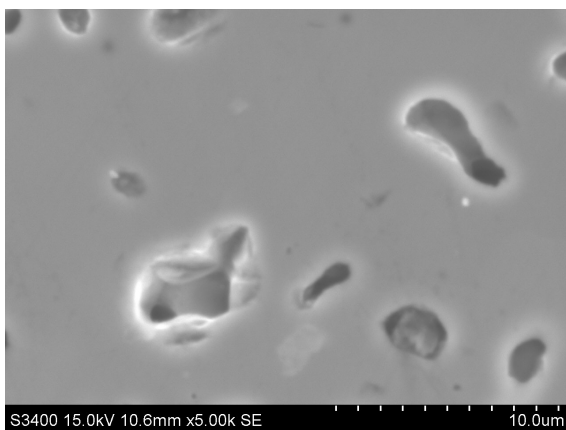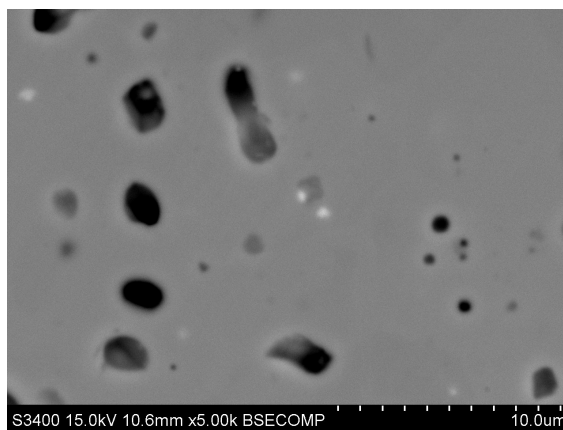
Appendix C

Additional phase diagrams

Figure C.1: CaO-MnO-Al$_2$O$_3$ phase diagram [28]

Appendix D
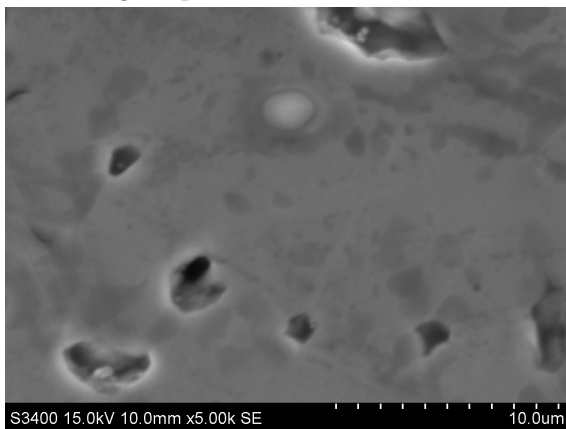
SE and BSE images of polished samples
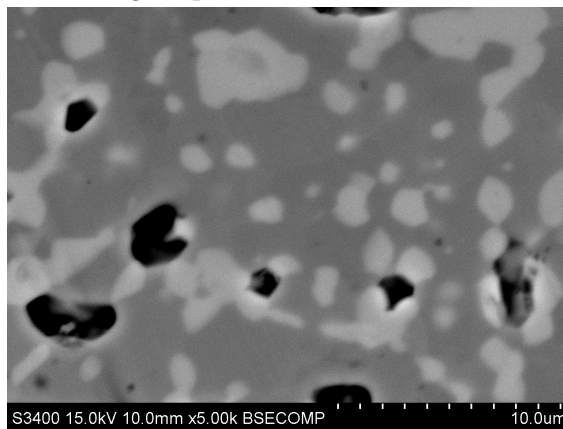

(a) SE image of polished stoichiometric CaMnO$_3$

(b) BSE image of polished stoichiometric CaMnO$_3$

(c) SE image of polished 5vol% CaMn$_2$O$_4$

(d) BSE image of polished 5vol% CaMn$_2$O$_4$

Figure D.1: SE and BSE images of polished stoichiometric and 5vol% CMO

Appendix E

Numerical values used in calculations

Table E.1: Overview over theoretical densities used in calculations.

Material	$Ca_{0.5}Mn_{0.5}O$	$CaMnO_3$	$CaMn_2O_4$	$Ca_2Mn_3O_8$
Theoretical density [g/cm3]	4.25 [68]	4.58 [71]	4.68 [70]	4.13 [69]

Table E.2: Overview over cell parameters for all materials involved used in discussion.

Material	Unit cell vol. [nm^3]	Unit cell parameters [nm]			Crystal structure
		a	b	c	
$Ca_{0.5}Mn_{0.5}O$ [68]	0.0993	0.463	0.463	0.463	Rock-salt
$CaMnO_3$ [71]	0.2075	0.52829	0.74579	0.52675	Perovskite
$CaMn_2O_4$ [70]	0.3036	0.31492	0.998	0.966	Spinell
$Ca_2Mn_3O_8$ [69]	0.2998	1.1014	0.5851	0.4942	Monoclinic

Appendix F

Electrical conductivity measurement data

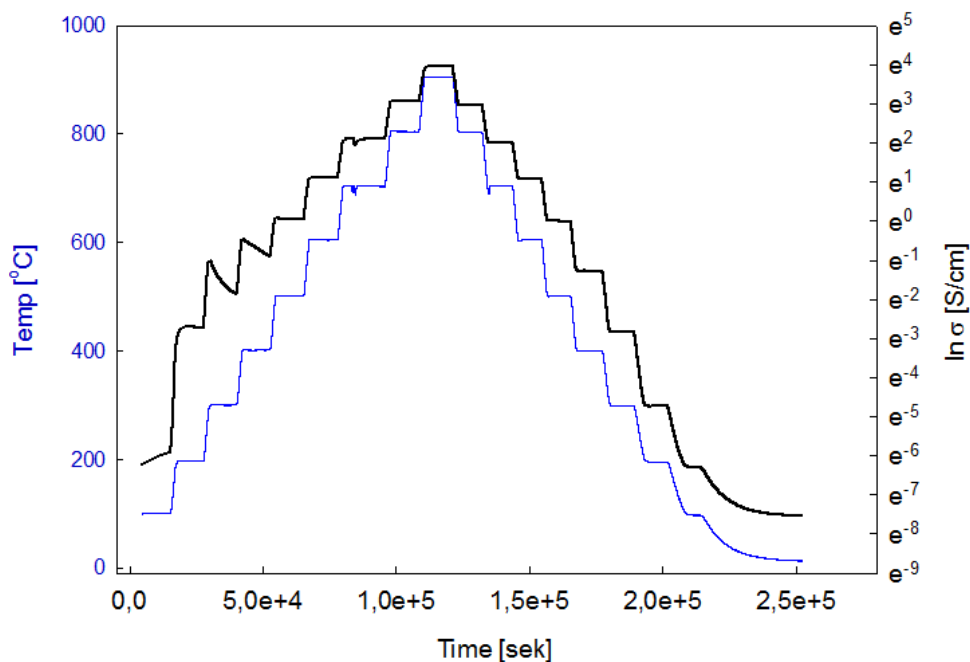
Figure F.1: Complete dataset from electrical conductivity measurement (black) including temerature program (blue). Data obtained from stoichiometric (V0) dense (90.2%) sample.

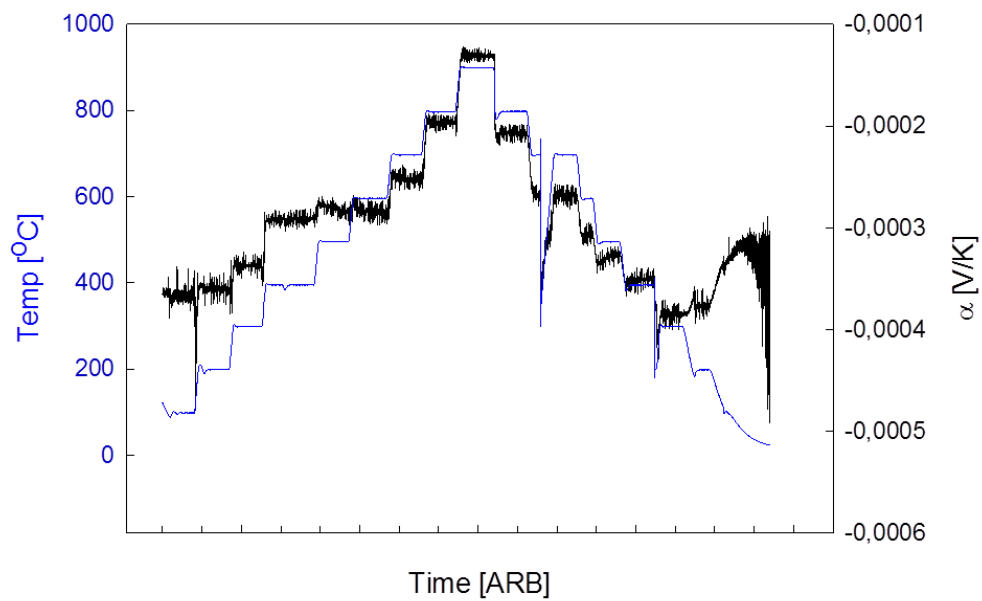# Appendix G

Seebeck measurement data

Figure G.1: Complete curve of Seebeck coefficient measurement (black) of stoichiometric (V0) sample together with the temperature program (blue).

Bibliography

[1] Bruker eva software. https://www.bruker.com/products/
x-ray-diffraction-and-elemental-analysis/x-ray-diffraction/
xrd-software/overview/eva.html. Accessed: 22.04.2015.

[2] Critical melting points and reference data for vacuum heat treating.

[3] Eds software - aztecenergy - oxford instruments. http://www.oxford-instruments.
com/products/microanalysis/energy-dispersive-x-ray-systems-eds-edx/
eds-for-sem/eds-software-aztec. Accessed:14.04.2015.

[4] Gas adsorption theory - presented by micromeritics instrument corporation. http://www.
micromeritics.com/repository/files/gas_adsorption_theory_poster.pdf. Accessed: 06.06.2015.

[5] C. O. Arean and F. S. Stone. Solid solution in the cao-mno system. *Journal of the Chemical
Society, Faraday Transactions 1: Physical Chemistry in Condensed Phases*, 75(0):2285–2294,
1979.

[6] N. A.S. Seebeck coefficient (thermoelectric power) measurements. http://www.norecs.
com/index.php?page=Seebeck+coefficient. Accessed:12.05.2015.

[7] U. Aschauer, R. Pfenninger, S. M. Selbach, T. Grande, and N. A. Spaldin. Strain-controlled
oxygen vacancy formation and ordering in camno3. *Phys. Rev. B*, 88:054111, Aug 2013.

[8] E. Bakken, T. Norby, and S. StÃÿlen. Nonstoichiometry and reductive decomposition of
camno3âĹŠÎť. *Solid State Ionics*, 176(1âĂŞ2):217–223, 2005.

[9] A. Bhaskar, C.-J. Liu, and J. J. Yuan. Thermoelectric properties of ca(1-x)gd(x)mno(3-d) (0.00, 0.02, and 0.05) systems. *The Scientific World Journal*, 2012:149670, 2012. 22997488[pmid] ScientificWorldJournal.

[10] A. Bhaskar, C.-J. Liu, J. J. Yuan, and C.-L. Chang. Thermoelectric properties of n-type ca(1-x)bixmn(1-y)siyo(3-d) system. *Journal of Alloys and Compounds*, 552(0):236–239, 2013.

[11] L. Bocher. Synthesis, structure, microstructure, and thermoelectric properties of perovskite-type manganate phases, 2009.

[12] S. BoškoviÄĞ, J. Dukić, B. Matović, L. Živković, M. Vlajić, and V. Krstić. Nanopowders properties and sintering of camno3 solid solutions. *Journal of Alloys and Compounds*, 463(1âĂŞ2):282–287, 2008.

[13] J. Briático, B. Alascio, R. Allub, A. Butera, A. Caneiro, M. T. Causa, and M. Tovar. Double-exchange interaction in electron-doped camno(3-d) perovskites. *Physical Review B*, 53(21):14020–14023, 1996. PRB.

[14] C. C. K. Chiang and K. R. Poeppelmeier. Structural investigation of oxygen-deficient perovskite camno2.75. *Materials Letters*, 12(1-2):102–108, 1991.

[15] J. Du, T. Zhang, F. Cheng, W. Chu, Z. Wu, and J. Chen. Nonstoichiometric perovskite camno(3-d) for oxygen electrocatalysis with high activity. *Inorganic chemistry*, 53(17):9106–9114, 2014.

[16] J. W. Fergus. Oxide materials for high temperature thermoelectric energy conversion. *Journal of the European Ceramic Society*, 32(3):525–540, 2012.

[17] M. Gao, D. M. Rowe, and K. Kontostavlakis. Thermoelectric figure-of-merit under large temperature differences. *Journal of Physics D: Applied Physics*, 37(8):1301, 2004.

[18] T. F. Gordon Alyward. *SI Chemical Data*. John Wiley and sons, 6 edition, 2008.

[19] J. B. H. Gordon B. Haxel and G. J. Orris. Rare earth elements - critical resources for high technology, 2002.

[20] J. R. Günter and H.-R. Oswald. Attempt to a systematic classification of topotactic reactions (commemoration issue dedicated to professor eiji suito on the occasion of his retirement). 1975.

[21] J. He, Y. Liu, and R. Funahashi. Oxide thermoelectrics: The challenges, progress, and outlook. *Journal of Materials Research*, 26(15):1762–1772, 2011.

[22] S. Hilaal Alama. A review on the enhancement of figure of merit from bulk to nano-thermoelectric materials. 2:190–2012, 2012.

[23] H. S. Horowitz and J. M. Longo. Phase relations in the ca-mn-o system. *Materials Research Bulletin*, 13(12):1359–1369, 1978.

[24] K. F. Hsu, S. Loo, F. Guo, W. Chen, J. S. Dyck, C. Uher, T. Hogan, E. K. Polychroniadis, and M. G. Kanatzidis. Cubic agpbmsbte2+m: Bulk thermoelectric materials with high figure of merit. *Science*, 303(5659):818–821, 2004. 10.1126/science.1092963.

[25] A. F. Ioffe. *Semiconductor thermoelements, and Thermoelectric cooling*. Infosearch, London, 1957.

[26] T. Ishihara. *Perovskite oxide for solid oxide fuel cells*. Springer Science and Business Media, 2009.

[27] R. Kabir, T. Zhang, D. Wang, R. Donelson, R. Tian, T. Tan, and S. Li. Improvement in the thermoelectric properties of camno3 perovskites by w doping. *Journal of Materials Science*, 49(21):7522–7528, 2014.

[28] Y.-B. Kang, I.-H. Jung, S. A. Decterov, A. D. Pelton, and H.-G. Lee. Critical thermodynamic evaluation and optimization of the cao-mno-sio2 and cao-mno-al2o3 systems. *ISIJ International*, 44(6):965–974, 2004.

[29] K. Koumoto, R. Funahashi, E. Guilmeau, Y. Miyazaki, A. Weidenkaff, Y. Wang, and C. Wan. Thermoelectric ceramics for energy harvesting. *Journal of the American Ceramic Society*, 96(1):1–23, 2013.

[30] Y. Lan, A. J. Minnich, G. Chen, and Z. Ren. Enhancement of thermoelectric figure-of-merit by a bulk nanostructuring approach. *Advanced Functional Materials*, 20(3):357–376, 2010.

[31] T. E. Loland. Development of oxide based thermoelectric materials, 2013.

[32] T. E. Loland. Thermoelectric properties of a-site deficient lanthanum substituted strontium titanate, 2014.

[33] N. Mazur. Development of oxide based thermoelectric materials. Technical report, NTNU, 2014.

[34] M. E. Melo Jorge, A. Correia dos Santos, and M. R. Nunes. Effects of synthesis method on stoichiometry, structure and electrical conductivity of camno3-d. *International Journal of Inorganic Materials*, 3(7):915–921, 2001. Syntesis metod.

[35] M. Molinari, D. A. Tompsett, S. C. Parker, F. Azough, and R. Freer. Structural, electronic and thermoelectric behaviour of camno3 and camno(3-d). *Journal of Materials Chemistry A*, 2(34):14109–14117, 2014.

[36] K. Momma and F. Izumi. Vesta 3 for three-dimensional visualization of crystal, volumetric and morphology data. *Journal of Applied Crystallography*, 44(6):1272–1276, 2011.

[37] H. Muguerra, B. Rivas-Murias, M. Traianidis, C. Marchal, P. Vanderbemden, B. Vertruyen, C. Henrist, and R. Cloots. Thermoelectric properties of n-type ca(1-x)dyxmn(1-y)nbyo(3-d) compounds prepared by spray-drying method. *Journal of Alloys and Compounds*, 509(29):7710–7716.

[38] D. Neagu and J. T. S. Irvine. Enhancing electronic conductivity in strontium titanates through correlated a and b-site doping. *Chemistry of Materials*, 23(6):1607–1617, 2011.

[39] G. S. Nolas, V. G. Harris, T. M. Tritt, and G. A. Slack. Low-temperature transport properties of the mixed-valence semiconductor ru0.5pd0.5sb3. *Journal of Applied Physics*, 80(11):6304–6308, 1996.

[40] G. S. Nolas, J. Sharp, and J. Goldsmid. *Thermoelectrics: basic principles and new materials developments*, volume 45. Springer Science & Business Media, 2001.

[41] Nong. *Advanced Materials*, 23(21):2482–2490, 2011.

[42] M. Ohtaki. Oxide thermoelectric materials for heat-to-electricity. *Kyushu University G-COE program "NOVEL CARBON RESOURCE SCIENCES"*, 3, 2010.

[43] M. Ohtaki. Recent aspects of oxide thermoelectric materials for power generation from mid-to-high temperature heat source. *Journal of the Ceramic Society of Japan*, 119(1395):770–775, 2011.

[44] M. Ohtaki, H. Koga, T. Tokunaga, K. Eguchi, and H. Arai. Electrical transport properties and high-temperature thermoelectric performance of (ca0.9m0.1)mno3 (m = y, la, ce, sm, in, sn, sb, pb, bi). *Journal of Solid State Chemistry*, 120(1):105–111, 1995.

[45] M. Ohtaki, T. Tokunaga, K. Eguchi, and H. Arai. Hopping carrier mobilities and thermoelectric properties of oxide materials with perovskite-related structure. In *Thermoelectrics, 1997. Proceedings ICT'97. XVI International Conference on*, pages 224–227. IEEE, 1997.

[46] S. E. Olsen, S. Olsen, M. Tangstad, and T. Lindstad. *Production of manganese ferroalloys*. Tapir Academic Press, 2007.

[47] P. B. Paothep Pichanusakorn. Nanostructured thermoelectrics. 67:19–63, 2010.

[48] W. Parker, R. Jenkins, C. Butler, and G. Abbott. Flash method of determining thermal diffusivity, heat capacity, and thermal conductivity. *Journal of applied physics*, 32(9):1679–1684, 1961.

[49] D. D. Pollock. *Thermoelectricity: theory, thermometry, tool*, volume 852. American Society for Testing and Materials., Philadelphia, 1985.

[50] S. Populoh, M. Trottmann, M. H. Aguire, and A. Weidenkaff. Nanostructured nb-substituted camno 3 n-type thermoelectric material prepared in a continuous process by ultrasonic spray combustion. *Journal of Materials Research*, 26(15):1947–1952, 2011.

[51] A. Reller, G. Davoodabady, and H. Oswald. Reversible topotactic reduction of perovskite-related calcium manganese oxides. *Thermochimica Acta*, 83(1):121–124, 1985.

[52] D. Richerson, D. W. Richerson, and W. E. Lee. *Modern ceramic engineering: properties, processing, and use in design.* CRC press, 2005.

[53] R. C. Ropp. *Encyclopedia of the alkaline earth compounds.* Newnes, 2012.

[54] D. . M. . Rowe, editor. *Thermoelectrics Handbook Macro to Nano.* CRC Press, 2006.

[55] D. M. Rowe, editor. *CRC Handbook of Thermoelectrics.* CRC Press, 1995.

[56] F. Ryoji, M. Ichiro, I. Hiroshi, T. Tsunehiro, M. Uichiro, and S. Satoshi. An oxide single crystal with high thermoelectric performance in air. *Japanese Journal of Applied Physics*, 39(11B):L1127, 2000.

[57] M. Schrade, R. Kabir, S. Li, T. Norby, and T. G. Finstad. High temperature transport properties of thermoelectric camno3-d - indication of strongly interacting small polarons. *Journal of Applied Physics*, 115(10), 2014.

[58] J. Sele. Development of thermoelectric n-type oxides in the la-sr-ti-o-system, 2013.

[59] R. D. Shannon. Revised effective ionic radii and systematic studies of interatomic distances in halides and chalcogenides. *Acta Crystallographica Section A*, 32(5):751–767, 1976.

[60] G. J. Snyder and E. S. Toberer. Complex thermoelectric materials. *Nat Mater*, 7(2):105–114, 2008.

[61] J. Sootsman, D. Chung, and M. Kanatzidis. New and old concepts in thermoelectric materials. *Angewandte Chemie International Edition*, 48(46):8616–8639, 2009.

[62] H. Taguchi, M. Nagao, T. Sato, and M. Shimada. High-temperature phase transition of camno3-d. *Journal of Solid State Chemistry*, 78(2):312–315, 1989.

[63] P. Thiel, J. Eilertsen, S. Populoh, G. Saucke, M. Dãűbeli, A. Shkabko, L. Sagarna, L. Karvonen, and A. Weidenkaff. Influence of tungsten substitution and oxygen deficiency on the thermoelectric properties of camno3âĹŠd. *Journal of Applied Physics*, 114(24), 2013.

[64] O. R. Valmot. Enormt potensial for energisparing. pages 30–31, 2013.

[65] A. Varela, S. d. Dios, M. Parras, M. Hernando, M. T. Fernandez-Diaz, A. R. Landa-Canovas, and J. M. Gonzalez-Calbet. Ordered rock-salt related nanoclusters in camno2. *Journal of the American Chemical Society*, 131(24):8660–8668, 2009.

[66] S. I. Vecherskii, M. A. Konopel'ko, N. O. Esina, and N. N. Batalov. Transport properties of ca(1-x)mn(o3-d) + xceo2(0 < x âĽ'ď' 0.15) mixtures. *Inorganic Materials*, 38(12):1270–1276, 2002.

[67] M. V. Vedernikov and E. K. Iordanishvili. A.f. ioffe and origin of modern semiconductor thermoelectric energy conversion. In *Thermoelectrics, 1998. Proceedings ICT 98. XVII International Conference on*, pages 37–42.

[68] P. Villars. Material phases data system, ca0.5mn0.5o. http://materials.springer.com/isp/crystallographic/docs/sd_1500211, 2014. Accessed:15.05.2015.

[69] P. Villars. Material phases data system, ca2mn3o8. http://materials.springer.com/isp/crystallographic/docs/sd_1404989, 2014. Accessed:31.05.2015.

[70] P. Villars. Material phases data system, camn2o4. http://materials.springer.com/isp/crystallographic/docs/sd_1810135, 2014. Accessed:31.05.2015.

[71] P. Villars. Material phases data system, camno3. http://materials.springer.com/isp/crystallographic/docs/sd_1621032, 2014. Accessed:31.05.2015.

[72] C. B. Vining. An inconvenient truth about thermoelectrics. *Nat Mater*, 8(2):83–85, 2009.

[73] C. Wan, Y. Wang, N. Wang, W. Norimatsu, M. Kusunoki, and K. Koumoto. Development of novel thermoelectric materials by reduction of lattice thermal conductivity. *Science and Technology of Advanced Materials*, 11(4):044306, 2010.

[74] B. White, J. Souza, C. Chiorescu, J. Neumeier, and J. Cohn. Magnetic, transport, and thermodynamic properties of camn2o4 single crystals. *Physical Review B*, 79(10):104427, 2009.

[75] M. R. Winter and D. R. Clarke. Oxide materials with low thermal conductivity. *Journal of the American Ceramic Society*, 90(2):533–540, 2007.

[76] B. Wolfing, C. Kloc, J. Teubner, and E. Bucher. High performance thermoelectric tl9(bite)6 with an extremely low thermal conductivity. *Phys. Rev. Lett.*, 86:4350–4353, May 2001.

[77] S. Zouari, L. Ranno, A. Cheikh-Rouhou, O. Isnard, M. Pernet, P. Wolfers, and P. Strobel. New model for the magnetic structure of the marokite-type oxide camn2o4. *Journal of alloys and compounds*, 353(1):5–11, 2003.